POLITECNICO
MILANO 1863

SCUOLA DI INGEGNERIA INDUSTRIALE
E DELL'INFORMAZIONE

Investigating Different Convective Drying Conditions and the Impact on Cracks and Electrochemical Performance

TESI DI LAUREA MAGISTRALE IN
ENERGY ENGINEERING - INGEGNERIA ENERGETICA

Author: **Armin Kahrom**

Student ID: 912975
Advisor: Prof. Andrea Casalegno, Prof. Odne Stokke Burheim
Co-advisors: Silje Nornes Bryntesen, Ignat Tolstorebrov
Academic Year: 2022-23

Abstract

The characteristic that determines the microstructure of battery electrodes fundamentally changes during drying, making it a critical yet imperfectly understood processing step in cell manufacture. As a result, drying is an important step in electrode manufacturing since it can change component distribution inside the electrode. Phenomena such as binder migration, might have a detrimental impact on cell performance or cause mechanical failure.

Four different approaches of thermal conditions for drying procedure are introduced and investigated in three aspects including energy consumption of drying process, cracks formation, and electrochemical performance. The study admits that drying conditions have a considerable effect on cracks formation, which means the higher drying rate and critical moisture content lead to an irregular drying regime and a raise of crack formation.

In addition, based on the results of galvanostatic cycling, the specific discharge capacity and capacity retention after long-term cycling of half-cells with lower cracks show better electrochemical performance in comparison with samples with higher cracks density. The results of experiments admit that the cracks can increase the capacity fade of cells and decrease the initial capacities.

Finally, the study compares the different approaches of drying procedures to suggest the most energy-effective approach to drying in terms of energy consumption per produced capacity($\mathrm{Wh}_{drying}/\mathrm{Wh}_{capacity}$). It is found that the half-cells which were undergone extreme thermal conditions and higher drying rates, consumed significantly lower energy in comparison with other cells that were produced under lower drying rates. Hence, since the drying step considerably affects the total energy consumption of cell manufacturing, a reasonably high drying approach is recommended taking into account the electrode capacity to obtain an enhanced energy efficiency.

Keywords: Energy consumption, Binder migration, Cracks, Drying rate, Critical moisture content, convective drying, specific discharge capacity, capacity retention

Abstract in lingua Italiana

La caratteristica che determina la microstruttura degli elettrodi della batteria cambia radicalmente durante il processo di asciugatura, rendendola una fase di elaborazione critica, ma non perfettamente compresa nella produzione di celle. Perciò, l'essiccamento risulta essere una fase importante nella produzione degli elettrodi poiché può cambiare la distribuzione del componente all'interno dell'elettrodo. Fenomeni come la migrazione del legante potrebbero avere un impatto negativo sulle prestazioni della cella o causare guasti meccanici.

Sono stati introdotti quattro diversi approcci di definizione delle condizioni termiche per la procedura di essiccazione, che è stata studiata sotto tre aspetti tra cui il consumo di energia del processo di essiccazione, la formazione di crepe e le prestazioni elettrochimiche. Lo studio ammette che le condizioni di essiccazione hanno notevole effetto sulla formazione delle crepe, il che significa che il tasso di essiccazione più elevato e un'eccessiva umidità portano ad un regime di essiccazione irregolare e alla formazione di crepe.

Inoltre, in base ai risultati del ciclo galvanostatico, la capacità di scarica specifica e la ritenzione della capacità dopo il ciclo a lungo termine delle semicelle con crepe minori, mostrano prestazioni elettrochimiche migliori rispetto a campioni con densità di cricche maggiore. I risultati degli esperimenti mostrano che le crepe possono aumentare la capacità di dissolvenza delle celle e diminuire le capacità iniziali.

Infine, lo studio mette a confronto i diversi approcci delle procedure di essiccazione al fine di definire il metodo di essiccazione più efficiente dal punto di vista energetico, in termini di consumo energetico per capacità prodotta ($Wh_{essiccazione}/Wh_{capacit}$). I risultati mostrano che le semicelle che sono state sottoposte a temperature estreme e tassi di essiccazione più elevati, hanno consumato significativamente meno energia rispetto ad altre celle che sono state prodotte con tassi di essiccazione inferiori. Quindi, la fase di asciugatura risulta influire notevolmente sul consumo energetico totale per la produzione delle celle e si consiglia ragionevolmente un'elevata essiccazione tenendo conto della capacità dell'elettrodo per ottenere una migliore efficacia energetica.

Parole chiave: Consumo di energia, Migrazione del legante, Crepe, Tasso di essiccazione,

Umidità critica contenuto di tura, essiccamento convettivo, capacità di scarico specifica, capacità di ritenzione

Contents

Introduction

0.1. Background

Nowadays, the renewable energy grid and related innovations are strongly connected on energy storage. One of the usual ways of storing the energy is rechargeable batteries. Successful deployment of electric vehicles requires maturity of the manufacturing process to minimize the cost of the lithium-ion battery pack (LIB). The renewable energy grid, as well as associated technologies including electric vehicles, are now highly dependent on energy storage[83]. lithium-ion batteries are one of the most common ways to store energy. As the world shifts away from fossil fuels and toward emissions-free electrification, energy storage becomes one of the most important concerns in the global energy system.[2]. According to EIA report in august 2021[12], At the end of 2019, lithium-ion technology was employed in more than 90% of the installed power and energy capacity of large-scale battery storage systems in operation in the United States.

Additionally, according to a report published by Fortune Business Insights, lithium-ion batteries will be the most common kind of energy storage in the globe by 2020, with a market share of more than 97%[12]. lithium-ion batteries have a high cycle efficiency (they don't lose a lot of energy between charges and discharges) and quick reaction times. They are also the current battery of choice for most portable electronic and electric vehicle applications because of their high energy density (stored energy per unit of weight)[12].

Furthermore, the cost and storage capacity of batteries are considerable factors for the future of market and renewable energy growth[40]. Each step of the battery production process is under development and study to reach the most optimized way of production, both in terms of cost and energy consumption. Hence, more studies and research are necessary to reduce energy consumption, which leads to more cost-effective lithium-ion batteries. One of the expensive steps of battery production is the drying step. According to Wood et al[85] approximately the 15% share of electrode processing cost is for drying, or in other words, nearly 9% of the cost of a battery pack.

The electrode manufacture consists of four main steps: Mixing, in this step the active

material, binder, conductive agent, solvent and other additives are mixed in specific mass ratios. Here, NMC111 ($Li(Ni_{0.33}Mn_{0.33}Co_{0.33})O_2$) is used as active material, polyvinylidene fluoride (PVDF) as binder, carbon black as additive to form 3D conductive network and NMP as solvent.

Coating and drying, after mixing the material the produced slurry should be coat on a thin Aluminum foil as current collector by a tape caster and dry until the solvent be evaporated from the surface and forms the cathode. calendering and cell assembly, porous cathodes are pressed by two cylinders and cut or punched in desired shapes to assemble the preferred type of cell.

N-Methyl-2-pyrrolidone (NMP) is used to dissolve the polyvinylidene fluoride (PVDF) which is used as binder in the slurry preparation. After the slurry is mixed homogenously the NMP should be removed from the slurry through the drying process. Moreover, the NMP is a toxic solvent the vapor could not be released in atmosphere. Besides the toxicity, according to the NMP datasheets, if the NMP ratio in air reaches the limit of 1.3 % it may cause fire. Hence, large amount of warm air is required to reduce the mentioned risks and it needs considerable amount of energy. Since One of the most energy consuming steps in making an LIB is the drying of electrodes[17, 85], many studies concentrate on drying process of electrodes, for example Jaiser et al [47] studied The distribution of liquid at the surface and the emptying of pores during drying.[47] Other scientists such as Jaiser et al [47] and Laudone et al [70] studied the film shrinkage and liquid depletion of pores of thin film during the solvent evaporation. The results admit that the liquid depletion in surface pores can occur both prior and concurrent with the end of film shrinkage. Also, Zhou et al [99]studied different conditions of drying NMP solvent and . The paper calculates the drying rate of NMP during the first stage of drying process under different parameters and investigates the drying rate and the wind speed of the dryer.[47, 70, 99]

One of the most energy and time consuming steps of battery production is drying process of cathode material with almost 40 % share of total energy consumption of battery manufacturing process[99]. The boiling point of positive electrode solvent NMP is 204 °C which is very high, and since the drying temperature is in the range of 90 °C to 150 °C , the evaporation rate is noticeably slow. Consequently, it requires long drying time and significant production cost[86].

0.2.   Objectives

The project aims to study a more Green House Gasses-effective battery production through energy optimization of cathode drying by varying the drying rate of NMP. The main idea

is to provide different heating conditions by changing the drying temperatures and air velocities (heat transfer coefficient of air) to obtain various drying rates of the NMP solvent.

The drying conditions could be adjusted, and the results could be recorded by a well-designed lab-view software connected to the sensors of drying chamber. The drying chamber provides a temperature range from 20-100 °C and an air velocity up to from 1 m/s. As a result, the study analyzes four distinct circumstances in the potential range to provide four different solvent NMP drying rates, including 50 ° C, 100 ° C, for 0.5 m/s and 1 m/s of air velocity.

In the first section of experiments, the drying time, total cathode material mass, and mass of evaporated NMP are measured for energy consumption analysis. This section of experiments leads to the charts of percentage of evaporated NMP to time, mass reduction over time, the crack analysis of cathode surface, and energy required per mass unit of evaporated NMP for each thermal condition. The results of drying experiments should be directly considered as energy consumption assessment. Moreover, the consequence of each drying experiment may effect the quality of cathode surface, so the quality of cathode are investigated by scanning electron microscopy (SEM).

The next part of project are dedicated to surface quality investigations with focus on cracks tracking on the cathode surface by SEM. Since cracks could be one of the effective reasons of capacity decay during cycling [20], it would be reasonable to consider the cracks quantity as one of the main surface quality of produced cathodes.

The third part of experiments is devoted to the galvanostatic charge/discharge cycling tests to study the impact of cracks caused by each specific thermal condition of drying process on the battery performance. To be more specific, two galvanostatic cycling tests are performed including rate test cycling and long-term cycling. In the rate test, the cells undergo different C-rates from 0.1 C to 5 C to study the performance of the cells under different rate of discharge. In long-term cycling, the capacity decay of cells is investigated after over 100 cycles at a constant C-rate of 0.5 C to study the indirect impact of different drying conditions and direct effects of cracks on the cells performance.

In the last part of project, all the last sections would be considered together to Figure out the optimized thermal condition of drying process in cathode production. Hence, the energy consumption analysis, morphology of cathodes (cracks analysis) and performance of cells should be put in a nutshell.

0.3. Definitions and Typical Battery Parameters

Cell voltage: the voltage difference between the electrodes determines the result. The electrons are forced to flow across a circuit by the voltage. The whole battery system's compatibility determines the total cell voltage. When no power is pulled from or applied to the battery, the operating voltage, also known as the open circuit potential (V_{OC}), is the potential [60].

Capacity: the capacity of a battery refers to the quantity of electrical charge it can store and deliver over time. It's often measured in ampere-hours (Ah). The specific capacity (mAh/g) refers to the capacity in relation to the active material's mass[52].

Coulombic efficiency Over the course of a cycle, the Coulombic Efficiency (CE) is the ratio of the charge supplied into the battery to the charge retrieved from it[75]. **C-rate**: The C-rate is a measurement of how fast a battery is charged or drained in comparison to its maximum capacity in one hour. A C-rate of 1 C, for example, signifies that the required current is supplied to or drained from the battery in order to fully charge or discharge it in one hour[77].

Capacity retention: Capacity retention, also called capacity loss or capacity fade is the ratio of discharge capacity of a specific cycle to initial discharge capacity.[88].

1 | Theory

1.1.   The lithium-ion Batteries

The lithium-ion battery (LIB) is one of the most capable energy storage technologies currently available and widely used in portable electronics. According to Statista 2022 [1], the worldwide market for rechargeable LIBs is now valued at 40.5 billion dollars per annum and it is projected to be as large as 92 billion dollars in 2026. The main reason behind such rapid growth is its high energy density and cycling performance that no other energy storage methods can match[78]. Recent demands on energy and environmental sustainability have further spurred great interest in a larger scale LIB system for electric vehicles (EVs) and grid load leveling as well as complimentary energy storage for renewable energy resources, such as solar and wind power[93].

Nickel-metal hydride and LIBs are two types of power batteries used in electric vehicles. Because of their high charge and discharge rates and environmentally friendly qualities, nickel-metal hydride batteries are commonly employed in HEVs. However, the application of nickel-metal hydride batteries in EVs remains limited because they have low voltage and are unsuitable for parallel connection. The LIBs, with the advantages of a high voltage performance platform, such as high energy density (theoretical specific capacity reaches 3860 mAh/g), environmentally benign features, wide operating temperature range, low self-discharge rate, no memory effect, high efficiency, and long cycle life, have become widely accepted in recent years, and have become one of the most important components for the new generation of EVs[8].

LIBs store electrical energy in electrodes made of lithium(Li)-intercalation compounds that occur at the cathode and anode during oxidation and reduction processes. A LIB generally comprises a graphite negative electrode (anode), a nonaqueous liquid electrolyte, and a layered $LiCoO_2$ positive electrode (cathode) as shown in Figure 1.1. On charging, Li^+ are deintercalated from the layered $LiCoO_2$ cathode host, transferred across the electrolyte, and intercalated between the graphite layers in the anode. The discharge reverses this process, allowing electrons to travel across an external circuit and power numerous
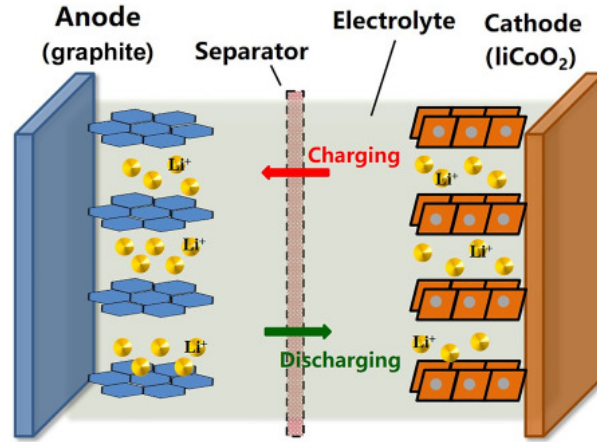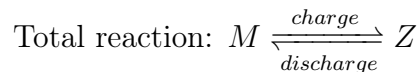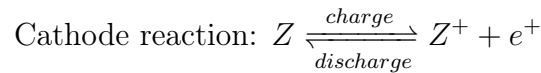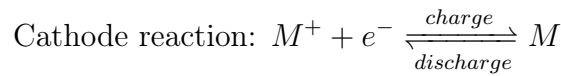
devices.

Figure 1.1: A LIB cell in which, during discharge, Li^+ migrate through the electrolyte and electrons flow through the external circuit, both moving from the anode (negative) to the cathode (positive)

The rechargeable LIB is the pinnacle of solid-state chemistry in action, which began with the discovery of intercalation compounds like Li_xMO_2 (M = cobalt or nickel), which first postulated by Goodenoughand are still commonly employed today [39].The discovery of low-voltage, Li-intercalation, carbonaceous materials that are highly reversible led to the commercialization of $LixC_6/Li_{1-x}CoO_2$ cells by Sony in 1991[10]. The energy conversion in the so-called rocking-chair cells is completed via the following reactions[39, 52] .

The reactions below demonstrate an example of a LIB's cathode, anode, and entire reaction using LCO as the cathode material and graphite as the anode material.

$$\text{Cathode reaction: } M^+ + e^- \underset{discharge}{\overset{charge}{\rightleftharpoons}} M$$

$$\text{Cathode reaction: } Z \underset{discharge}{\overset{charge}{\rightleftharpoons}} Z^+ + e^+$$

$$\text{Total reaction: } M \underset{discharge}{\overset{charge}{\rightleftharpoons}} Z$$

Typical LIB cells is about 3.8 V and the practical specific capacity is in the range of 150 Ah/kg to 182 Ah/kg [58] while the theoretical specific capacity is 270 Ah/kg. The favorable electrochemical performance in energy/power densities and advancements in system design and manufacturing have made the early LIBs a great success for mobile

electronics [93].

Each LIB cell is made up of five primary components that must be put together to form a single cell. Electrolyte, separator, anode, cathode, and casing are the components; each component will be explained in detail in the following sections.

1.1.1.   The Electrolyte

The electrolyte is a medium that facilitates ion movement between a cell's cathode and anode. In general, the electrolyte is designed for a specific battery system While the electrolyte can be a liquid, a gel, a solid polymer, or an inorganic solid, most LIBs use liquid electrolytes containing a lithium salt, such as Lithium hexafluorophosphate ($LiPF_6$) , $LiBF_4$, $LiClO_4$, $LiBC_4O_8$ (LiBOB), or $Li[PF_3]$, and (LiFAP) dissolved in a mixture of organic solvents.[8]

According to Reiner Korthauer et al [52] the electrolyte should fulfill the requirements listed below:

1. High ionic conductivity across a wide temperature range (-40°C to +80 °C) to ensure good flow of Li^+ between the electrodes.

2. Sufficiently electrically insulated cell to force the electrical charge out into the external circuit.

3. Cycling stability over several thousand cycles.

4. Chemical and electrochemical compatibility with the other cell components in all operating conditions. It should be electrochemically stable up to potentials around 4 V, which is the general charging potential of current LIB technologies.

5. In general, safety, environmental and economic concerns should be considered.

The most widely used electrolytes deployed in commercial LIBs are based on the electrolyte solution of $LiPF_6$ dissolved in a mixture of organic carbonates [51]. It has high conductivity in room temperature, is electrochemically stable up to 4.8 V vs. Li/Li^+. The $LiPF_6$ is very water sensitive, and if exposed to water the $LiPF_6$ breaks down and produces hydroiodic acid (HF), which can deteriorate the cell [52].

$LiPF_6$ has many advantages over other conventional electrolyte salts such as $LiAsF_6$, $LiBF_4$ and $LiClO_4$[84]:

1. It can form suitable Solid electrolyte interface (SEI) membrane in electrodes, especially in cathode.

2. It can implement passivation for anode current collectors to prevent their dissolution. to force the electrical charge out into the external circuit.

3. It has wide windows of electrical stability.

4. It has excellent solubility and high conductivity in various solvents.

Decomposition products of electrolytes generate a passivization layer called the solid electrolyte interphase (SEI) on electrode surfaces. The SEI allows Li^+ transport and blocks electrons in order to prevent further electrolyte decomposition and ensure continued electrochemical reactions. Composition and morphology of SEI layers are key steps in developing superior SEI layers that prevent electrolyte breakdown on graphite surfaces. Because of their instability at the anode potential operating window, the anode SEI layer is made up of precipitates from reduced breakdown of solvents, salts, lithium ions, and contaminants in the electrolyte[35, 91]. It tends to be more common after the initial charge, but after that, until the SEI layer is fully developed, it continues to form slowly and progressively.[93]

Figure 1.2 presents the relative energy of electrons of anode, cathode, and electrolyte of a thermodynamically stable redox of a LIB. The difference between electrochemical potential of cathode (μ_c) and anode (μ_a) is presented in the Figure 1.2 is defined as open circuit voltage or V_{oc} [35] . Additionally, the difference between lowest occupied molecular orbital (LOMO) and highest occupied molecular orbital (HOMO) is defined as electrolyte's energy gap (E_g) . The gap between LOMO and HOMO is known as the stability window. If μ_a is higher than the LUMO energy, the electrolyte will be reduced, and if μ_c is lower than the HOMO energy, the electrolyte will be oxidized.[11]. To improve the energy density of the redox pair, the energy gap between the anode and cathode must be as large as possible. The organic electrolytes used in LIBs have oxidation potentials around 4.7 V vs. Li^+/Li and reduction potentials close to 1.0 V vs. Li^+/Li. The intercalation potential of Li into graphite is between 0 V and 0.25 V vs. Li^+/Li, which is below the reduction potential of the electrolyte. During charging, the voltage of the graphite electrodes falls below the electrolyte's stability window, and the electrolyte decomposes at the graphite surface, generating the SEI.[68, 93]

1.1.2.   The Negative Electrode

The negative electrode in LIBs is anode materials, which are coupled with cathode materials in a LIB cell. The anode materials in LIB cells act as the host where they reversibly allow Li^+ intercalation / deintercalation during charge / discharge cycles. As of today, graphite is the most commonly used and commercialized anode material since the first
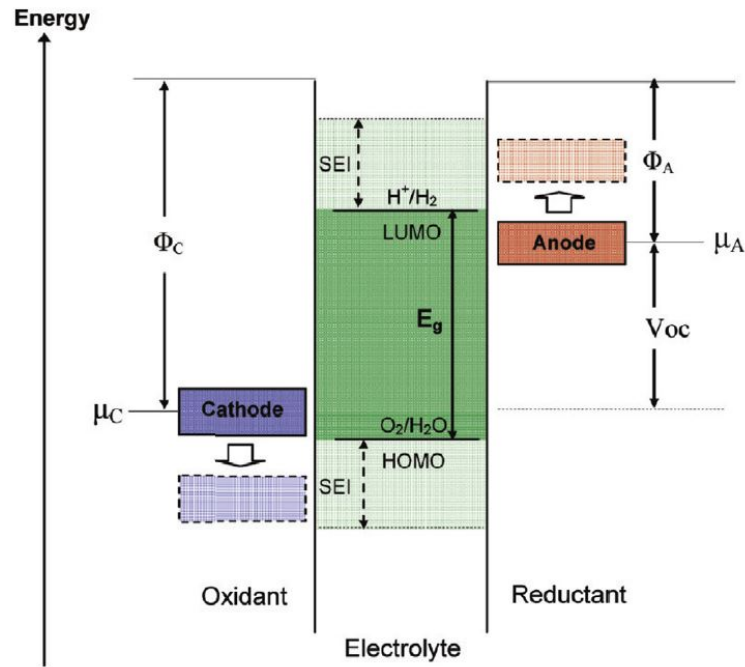
Figure 1.2: Energetics of the formation of the anode and cathode SEI layers under electroreduction and electro-oxidation conditions [34]

LIBs introduced in 1994[16, 69] because of its low price, abundance, high structural stability and low working potential (0.1 V) versus Li/Li^+, ensuring a long cycling life.[69]

However, given the study focuses on positive electrodes, the half-cells could be investigated here for experimental purposes of cathode evaluation (Positive electrode). Lithium half-cell configurations are frequently used to investigate LIB electrode materials, with a lithium metal electrode serving as both the counter and reference electrode. Because lithium metal has a steady reference potential and a large specific capacity of 3860 mAh/g, it can offer a vast reservoir of capacity, allowing reactions at the working electrode to be unrestricted by the capacity available at the counter electrode.[87]

Thus, the characterization of LIB electrodes in lithium half-cells is very useful to study the essential electrochemical properties of the materials, nonetheless, it could not predict the performance of full cells which use the cathode (e.g., lithium iron phosphate or LFP) and Anode (e.g., graphite)[72]. Therefore, as illustrated, since the project investigates on cathode in the following experimental study, the half-cells are used, and a plate of lithium metal plays the role as anode.

1.1.3. The Positive Electrode

Because the research focuses on the positive electrode, the manufacture of cathode components should be carefully investigated. A polymer binder (PB), a conductive additive (CA), and an active material (AM) make up the electrode. To summarize, the polymer binder's principal function is to hold the active material and conductive additive together, enhancing the electrodes' mechanical stability, particle cohesion, and flexibility. The conductive additive improves the electrode's electrical conductivity, while the active material determines is responsible for the cell's capacity and potential.[22, 33]. In the following, the active material, binder, and conductive additive will be reviewed.

Active Material

The cathode material is used to assess the energy density of LIBs. In the case of cathode materials, the main focus of research is on strengthening specific capacity and voltage, which can increase the battery's energy density. First generation LIBs batteries used layered $LiCoO_2$ as active material in cathode. However, in recent years, scientists have concentrated their efforts on chemical replacement in the layered framework to stabilize it, resulting in the creation of a variety of high-capacity cathodes, as illustrated in Figure 1.3.[9, 73]
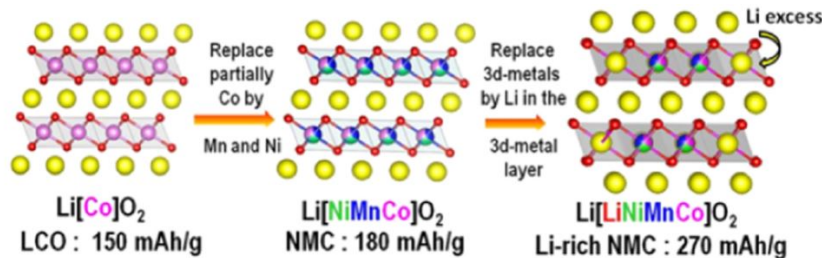

Figure 1.3: Evolution of Li-rich NMC from $LiCoO_2$ (LCO) and its effect on specific capacity

The partial substitution of Co(III) ions by Mn(IV) and Ni(II) ions resulted in the creation of $Li(NiCoMn)O_2$, which has higher specific capacities than first-generation cathode materials (LCO)[36]. Later, the efforts from the teams of Thackeray et al.[79] and Dahn et al. [24] developed "Li-rich NMC" with specific capacity of more than 250 mAh/g (theoretically). Furthermore, structural stability and positive ion ordering in the crystal framework of the cathode are found to govern the electrochemical performance of the layered cathode[73].

According to Peiyuan Guan et al.[36] and Akhalish et al.[9] for the cathode material the

general requirements should be fulfilled as below:

1. The Fermi level of the cathode material should be kept to a minimum.

2. The cathode's potential energy should be as high as feasible.

3. The intercalation/deintercalation of Li^+ of unit mass of material should be reversible and as many time as possible.

4. Li^+ intercalation and deintercalation should cause minimum changes or distortion in the material's structure, ensuring good reversibility.

5. Li^+ diffusion should be as quick as feasible to allow for a high power density.

6. Good ion conductivity and electron conductivity to achieve high electrical conductivity

7. High thermal stability and excellent combability with electrolyte

8. Synthesis should be easy and inexpensive.

Nevertheless, it is almost impossible to meet all the requirements that mentioned above, so there are a few materials that could be used as cathode material. Table 1.1, listed the renowned materials for cathode including their advantages and disadvantages[36]. There are different types of cathode materials but here only layered-type cathode will be discussed . A brief information about specific capacity, advantages and disadvantages are presented in the following tables.

In addition to the table 1.1 information about $LiNi_xCo_yMn_{1-x-y}O_2$ or NMC111, according to Akhalish et al [9], if the charging voltage exceeds the electrolyte's stability window, the danger of phase transitions in a delithiated state (the loss of lithium from an electrode of a LIB) and the risk of O2O2 gas development should be considered.

Hence, all the aforementioned information lead us to conclude that the $LiNi_xCo_yMn_{1xy}O_2$ (NMC) is one of the best active materials in these days for energy storing purposes[89]. Hence, the project uses $LiNi_xCo_yMn_{1-x-y}O_2$ or NMC111 as active material for the following experiments.

Binder

To hold the electrode's components together, a polymer binder is required. Polyvinylidene fluoride (PVDF) [62], which dissolves in hazardous, flammable, and expensive solvents including N-methyl pyrrolidone (NMP) and N-dimethylformamide, is the most used polymer binder for lithium ion batteries (DMF)[33]. It has been proven that the binder type

Table 1.1: The list of layered type materials for cathodes with advantages and disadvantages[36]

Layered-type cathode materials	Specific capacity (mAh/g) theoretical/actual	Advantages	Disadvantages
$LiMO_2$	Co: 148 280 / Ni: 150 Mn: 140	Co: Stable electrochemical performance and ease of synthesis Ni: High rate capability Mn: High reversible capacity (190 mAh/g) at 2.0–4.5 V	Co: Lack of resources, toxic and high price Ni: Difficult synthesis and low thermal safety Mn: Difficult synthesis and low cycle stability.
$LiNi_{0.5}Mn_{0.5}O_2$	275/188	High reversible capacity, good overcharge resistance performance (4.5V) and low cost	Low rate capability, poor low-temperature performance and susceptible of temperature
$CeLiNi_xCo_yM_{1-x-y}O_2$	NCM111: 170 NCM523: 166 280 / NCM622: 176 NCM811: 203 NCA: 200	Mn: High specific capacity and high capacity retention ratio. Particularly, the nickel-rich NCM cathode materials deliver higher energy density, lower cost, and longer cycle life. Al: High energy and power density with an average voltage of 3.7 V	Mn: Poor compatibility with electrolytes and slightly lower voltage Al: High cost and poor system safety
$cexLi_2MnO_3$ / (1-x)$LiMO_2$	458/270	High practical specific capacity (general more than 200 mAh/g)	Low initial cycle efficiency and irreversible capacity loss (40–100 mAh/g)

and the molecular chain length of the binder affect the adhesion of the electrode to the current collector. Moreover, since the molecular weight and the slurry viscosity are high, less binder immigration would happen as a consequence [19, 38]. The cohesive strength of particles and the electrode-film/current-collector adhesion strength, as well as electrolyte soaking, are affected by polymer binder concentration of up to 20%. [33].

Because PVDF must be dissolved in NMP, which is poisonous and flammable, scientists have recently developed new binders that are recyclable and can be dissolved in water.[95]. Water-based binders, such as styrene-butadiene-rubber (SBR), sodium-carboxyl-methyl-cellulose (CMC), poly (acrylamide-co-diallyl dimethylammonium) (AMAC), and an SBR and CMC mixture binder have been widely evaluated as binder materials for electrodes in LIBs and they show similar bonding ability and high flexibility[27, 37, 95].

According to Cholewinski et al [23] binders have three main roles in battery performance. First of all, they are required to disperse the other components in solvent throughout the manufacturing process, resulting in a homogenous dispersion of the chemical[42, 48]. Second, binders hold the energy storage components together, including the active material, any conductive additives, and the current collector, ensuring that all of these elements keep in contact.[18, 43]. Last but not least, they mostly play the role of a connection between the electrode and the electrolyte. The binders protect the electrode from corrosion and prevent depletion of the electrolyte while allowing ion movement across this interface [94].

Conductive Additive

In the composite electrode, the conductive carbon additive is added to improve the electrical conductivity of active materials and was once considered as an "inactive" component [61]. Carbon black (CB) is widely used as conductive additive for the electrode manufacturing. In addition, CB also attaches to the active material surfaces, allowing for short-range electrical interactions. Furthermore, high-intensity dry mixing appears to prevent the creation of electrically conductive networks.[15, 33] In the composite electrode, Even though the conductive additive in the composite electrode has a low weight percent (wt%), it has a large surface area and atomic percentage to cover the majority of the electrode surface. [92].

Additionally, the carbonaceous materials have various chemical functional groups on its surface, including hydroxyl-, carboxyl-, carbonyl-, and aromatic groups. The electrode-electrolyte interface film (EEI) is formed by the wide surface area and different functional groups of conductive carbon reacting with electrolyte both spontaneously and during elec-

trochemical cycling. The carbon additive interacts with the electrolyte through corrosion-like processes during the spontaneous reaction. The EEI is formed by the spontaneous polymerization of solvent molecules and has a similar composition to the EEI formed by electrochemical cycling. [65].

1.2.   Electrode Fabrication and Cell Assembly

The electrode production consists of two main preparation levels: slurry treating and film processing from slurry making and coating to drying and calendering. In the following, electrode main preparation parameters and the impact on electrode morphology and finally on battery performance are presented.

After the electrodes prepared, they should be punched or cut into the desired shapes. Then, the electrodes are prepared for cell assembly and galvanostatic cycling. In laboratory, the produced cells should be characterized terms of quality and electrochemical performance.
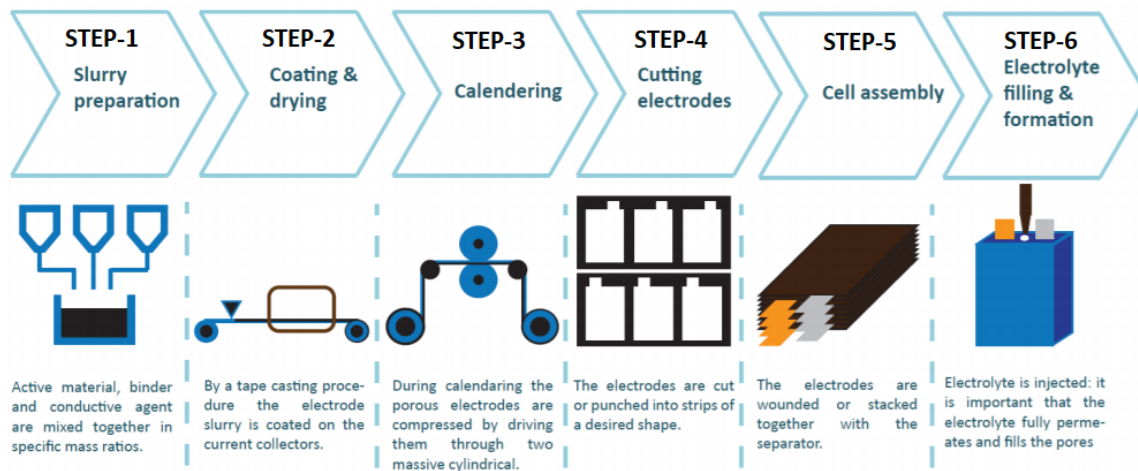

STEP-1	STEP-2	STEP-3	STEP-4	STEP-5	STEP-6
Slurry preparation	Coating & drying	Calendering	Cutting electrodes	Cell assembly	Electrolyte filling & formation
Active material, binder and conductive agent are mixed together in specific mass ratios.	By a tape casting procedure the electrode slurry is coated on the current collectors.	During calendaring the porous electrodes are compressed by driving them through two massive cylindrical.	The electrodes are cut or punched into strips of a desired shape.	The electrodes are wounded or stacked together with the separator.	Electrolyte is injected: it is important that the electrolyte fully permeates and fills the pores

Figure 1.4: electrode production from making the slurry to calendering, drying the electrodes and assembling the cells in various shapes and dimensions depending on purposes and conditioning as the last step of production. The picture is inspired by rheonics[3].

1.2.1.   Slurry

The very first step before the electrode fabrication is to select the slurry proportion and choose the solvent to solid ratio. An abbreviated notation is used to show the formula of composition. For instance, to represent the standard composition of cathode slurry which is 85 wt% active material, 10 wt% conductive material and 5 wt% binder the abbreviated

notation becomes 85:10:5.

In the next step, the slurry processing is commenced by the first phase which is mixing the binder with solvent to reach a homogenous solution then mixing active material, conductive material, and the binder-solvent solution. Mixing is an essential step for controlling the rheological properties of the system and for properly disperse the components within the slurry.

There is some common equipment for laboratories to achieve homogenous solutions, including magnetic stirrers, ultrasonic baths and ball mills and centrifugal mixer. The technique of slurry production, particularly the sequence in which the components are introduced, has been shown to affect rheological behavior and, as a result, electrode battery performance.[32].

During the mixing the components a solvent is needed to solve the components, specially the binder material should be properly solved to achieve a homogenous slurry. According to Mackeen et al [64] the most substantial characterizations that should be considered in slurry solvent selection is (1) its impact on rheology/viscosity of coating, (2) evaporation rate and vapor pressure (i.e., boiling point), (3) solubility of polymers, (4) dispersion stability, (5) surface tension, (6) flashpoint (i.e., flammability limit) and safety, and (7) cost and toxicity [17]. Table 1.2 represents some important characterizations of renown solvents.

Table 1.2: Chemical and physical properties of some common solvents for electrode slurry production at room temperature(20 °C) [17]

Solvent	Melting Point °C	Boiling Point °C	Dielectric Constant	Density (g/cm^3)	Viscosity ($10^{-3}Pa.s$	Flashpoint °C
Water	0	100	80.1	1	0.89	N/A
N-Methyl-2-pyrrolidon (NMP)	-24	202	32	1.033	1.67	96.65
Dimethylformamide (DMF)	-61	153	37	0.944	0.8	58
Dimethylacetamide (DMAC)	-20	166	38	0.942	2.14	63
Dimethyl Sulfoxide (DMSO)	18.4	189	47	1.092	2.00	95

1.2.2. Electrode Film Processing

There are three steps for electrode film processing, the first one is coating the produced slurry material on the current collector (e.g., aluminum foil), the next step is drying process of the coated cathode material, and the last step is calendering.

Casting Over Current Collector

Applying of the slurry over the current collector is possible thanks to tape caster and doctor blade (or film applicator). The tape caster or the film coating machine is mainly used

for LIBs electrode coating for coin cell assembly and pouch cell research. Doctor blade coating is a technique used to form films with well-defined thicknesses. The technique works by placing a sharp blade at a fixed distance from the surface that will be covered. The slurry solution is then poured in front of the blade, which is then pushed across the surface in a straight line, generating a wet film. The approach should ideally have solution losses of around 5%; however, finding optimal conditions takes time in practice.[21].

Drying Process

The second stage is solvent drying process. After the slurry has been applied to the current collector with a doctor blade (or film applicator), the slurry should be dried to remove the solvent and shape the electrode. Typically, the drying phases are classified into four main sections which is stated by Zhang et al. [97].

As in the Figure 1.5 the first stage of drying is converting the slurry to semi slurry phase due to solvent evaporation. After a while, the second phase followed by further removal of solvent to form a condensed layer of coating, and finally resulting in a compacted solid film coating.
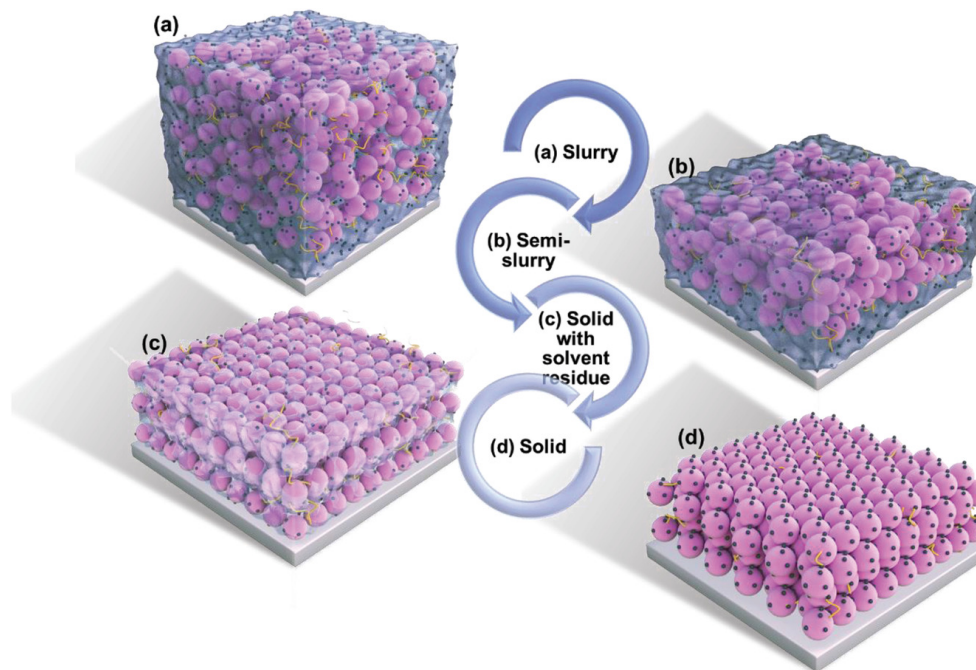
Figure 1.5: Typical electrode drying process from a) slurry phase to b) form a semi-slurry, following with the c) further removal of solvent and d) end up with a compacted solid film of coating (yellow lines indicate the binder, pink particles indicate active material particles, black dots indicate the conductive carbon and light blue color indicates the solvent).[97]

The drying of electrodes is a critical stage in the fabrication of LIBs since it has a major impact on the electrode's performance. Binder migration may occur if the solvent dries quickly. Furthermore, high drying rates will cause a heterogeneous distribution of the soluble and dispersed binder throughout the electrode, which might lead to accumulation near the surface[96]. The optimized drying rate during the electrode manufacturing process will promote balanced homogeneous binder distribution throughout the electrode film [21, 45, 56].

The drying process can be divided into three periods: heat-up or induction period, constant-rate, and falling-rate regimes. Figure 1.6 shows a typical drying curve for a coated web. During the constant rate period most of the solvent would be removed from the coated web. During this period, the solvent reaches the surface of the coating relatively unimpeded and the major resistance to mass transport is in the gas phase boundary layer at the surface of the coating. The next section of drying period is falling rate period, which is shown in Figure 1.6 that the slope of the moisture content or NMP solvent/time decreases and drying rate start to fall. Only a tiny portion of the total solvent removed is normally eliminated during this time. The falling-rate period, on the other hand, might account for a major amount of the entire drying time required to obtain the dried product's final properties. Because the greatest obstacle to mass transport is within the porous volume of the coating phase, the solvent is partially prevented from reaching the coating's surface during the decreasing rate period: In the decreasing rate phase, practical experiments are frequently required to determine drying time demands[85].
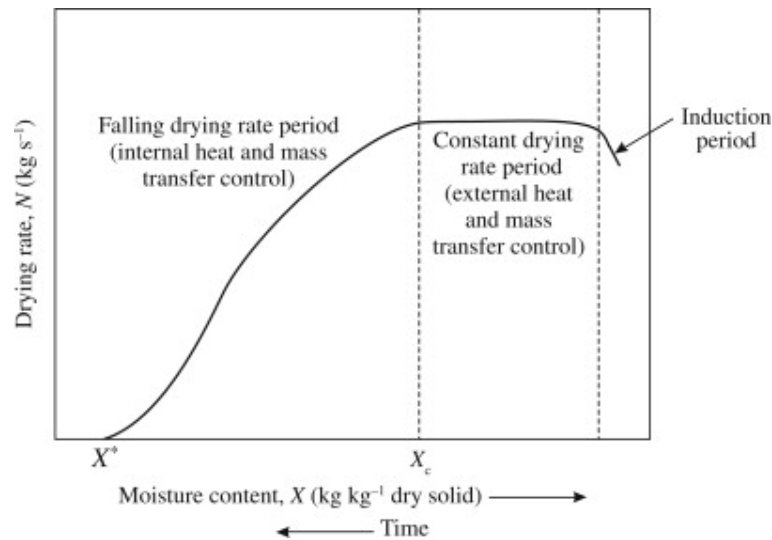

Figure 1.6: induction period (heat up), constant rate, and falling rate stages are shown in this typical drying curve, Source : M.Doran[25]

The heat transfer coefficient (K_t) and mass transfer coefficient (K_m) is connected together

by Lewis analogy. Heat and mass coefficients are dependent together by density and heat capacity of the gas and Lewis (Le) number. In the equation 1.1 n=0.33 for laminar flow and 0.4 for turbulent flow.[53, 76]

$$\frac{K_t}{K_m} = C_{p,G} \cdot \tilde{\rho}_G . Le^{1-n} \tag{1.1}$$

The heat and mass transfer coefficients are dependent variables to temperature and velocity of hot dry air flowing over the electrode, respectively. To achieve better understanding of the impact of hot air velocity on drying rate, the process will be investigated here. For the turbulent flow of hot air over a flat slab, the ratio of convective to conductive heat transfer at a boundary in a fluid (Nusselt) should be defined as below:

$$\bar{Nu} = 0.037 \cdot Re_L{}^{0.8} \cdot Pr^{0.33} \tag{1.2}$$

Considering the Nusselt definition and its relation with heat transfer coefficient:

$$Nu_L = \frac{hL}{K} \tag{1.3}$$

Where h is heat transfer coefficient, L is defined as characteristic length and let K as thermal conductivity of the fluid. So, the combination of equation 1.2 and equation 1.3 leads to the formula 1.4 to calculate the heat transfer coefficient.[76]

$$K_t = 0.037 \cdot V_a^{0.8} \cdot \frac{\mu_{air}}{\rho_a} \cdot Pr^{1/3} \cdot \lambda_a \cdot L^{-0.2} \tag{1.4}$$

The hot air velocity is shown by V_a, μ_{air} is the viscosity of air, and the Pr is representative of Prandtl number of air. The λ_a is the thermal conductivity of air and L (m)is the characteristic length, which is defined as:

$$L = \frac{V_{electrode}}{A} \tag{1.5}$$

Where $V_{electrode}$ is representative of volume (m^3)of electrode and A is surface of electrode(m^2). The mass transfer coefficient is then calculated from the heat transfer coefficient using the Chilton-Colburn correlation.[76]

$$K_m = \frac{K_t}{C_p \rho_a} \cdot Le^{-2/3} \tag{1.6}$$

where, Le is the Lewis number.

In order to figure out the critical moisture content ($X_{critical}$), constant drying rate and falling drying rate should be estimated by the measured data of experiments based on the equation 1.7.

$$W_D = \frac{-m_s}{A_e} \cdot \frac{dX}{dt} \tag{1.7}$$

Where m_s is representative of mass of dry solid in (kg), W_D is for drying rate in $kg/m^2.s$ and X (Moisture content)is for moisture content (kg of solvent/kg of bone dry material), A_e is for surface area of electrode in m^2 and t represents time in seconds[49] [14].

The increased drying stress can cause electrode defects including fracture, curl, and delamination, researchers have spent a lot of time looking into the influence of drying factors on internal stress and crack formation in electrodes [57, 59, 71]. According to the findings of the experiments, cracking became more severe as the drying temperature or in general drying rate rose.. The driving force for crack formation is capillary stress during drying [71]. Typically, the creation of holes, presumably due to film blistering during high-temperature drying, can be ascribed to the worsening crack severity. Furthermore, the electrode thickness influenced fracture initiation, and cracks were more likely to form at high drying rates[57].

The degree of binder migration is accelerated by a high drying rate, resulting in considerable heterogeneity in the electrode material. Under high drying rates, capillary tension practically increases, causing the solvent to move fast to the surface and promoting an obvious gradient distribution of inactive components. Furthermore, the drying rate has a substantial impact on the mechanical integrity of dried PVDF systems. The less uniform distribution of binders in PVDF-based coatings is to blame for this tendency.[100]

Energy Consumption

The evaporation load is the smallest amount of energy required for drying, but it must be delivered to the solids in a practical manner, such as through convective drying, contact or conduction drying, or absorbing electromagnetic radiation (infrared, radio frequency, or microwave drying). The process of delivering heat often requires far more energy than evaporation's latent heat.

The heater duty for the input air heat exchanger (without heater losses) for a continuous convective (hot air) drier is provided by[41]:

$$Q = A \cdot V_\alpha \cdot \rho_\alpha \cdot c_\alpha \cdot \Delta T \cdot D_t \tag{1.8}$$

Where A is area of channel's cross section, V_α is representative of drying air velocity, ρ_α is for density of air, c_α is average specific heat of air under adiabatic conditions (kJ/kg.K), T is temperature in degree Kelvin (K), and D_t is drying time. Moreover, the convection dryer is supported by a blower which blow the air into the drying chamber, the energy consumption of the blower should be determined in two steps. First, energy conservation equation for steady flow to determine the required power the blower as below:

$$\dot{Q}_{C\cdot V.} + \sum \dot{m}_i \cdot (h_i + \frac{1}{2} \cdot \dot{V}_{\alpha,i}^2 + g \cdot Z_i) = \dot{W}_{C\cdot V.} + \sum \dot{m}_e \cdot (h_e + \frac{1}{2} \cdot \dot{V}_{\alpha,e}^2 + g \cdot Z_e) \quad (1.9)$$

Where the $\dot{Q}_{C\cdot V.}$ and $\dot{W}_{C\cdot V.}$ are for heat and work of control volume. h_i and Z_i are representative of enthalpy and height of inlet air, while h_e and Z_e are for enthalpy and height of outlet air. Since input and output mass flow of air as defined by equation 1.10 ($\dot{m}_i$ and $\dot{m}_e$) are equal and the altitude of inlet and outlet is equal, the height and mass flow rate can be canceled out from both sides of equation.

$$\dot{m}_{i \, or \, e} = A \cdot V_\alpha \cdot \rho_\alpha \quad (1.10)$$

Also, initial air velocity can be assumed as zero because the air intake is motionless. So the equation 1.9 can be simplified to calculate the specific work needed for the air blower as below:

$$\dot{W} = h_i - (\frac{1}{2} \cdot \dot{V}_{\alpha,e}^2 + h_e) \quad (1.11)$$

Equation 1.11 can be used to calculate the specific work of blower based on KJ/kg of air ($\dot{W}$). However, in order to calculate the power of blower, it should be multiply with mass flow rate ($\dot{m}_\alpha$), so we have:

$$P_{blower} = \dot{W} \cdot \dot{m}_\alpha \quad (1.12)$$

The estimated power of blower (P_{blower}) should be multiply by drying time which results energy consumption of blower during the drying procedure:

$$E_b = P_{blower} \cdot D_t \quad (1.13)$$

Where P_{blower} is the power of the blower and the D_t is the dying time. Hence the total energy consumption of the convection dryer is the summation of energy consumption of blower (E_b) and energy consumption of heater (Q).

Drying Methods

In the industrial scale, large belt dryers with infrared radiators are the most prevalent approach for electrode drying. Hot air blowers might also be put in the coater to dry the electrode if the dry chamber has access to upstream. This is to prevent the cell components from remoistening after drying.[55, 97]

In the case of laboratory scale electrode drying, the convectional air-drying method (Figure 1.7) and vacuum oven are common. The convectional air-drying method is to cast the slurry on the current collector (CC) and dry in an ambient air temperature or similar mild temperature [97].The vacuum drying oven is a closed oven with adequate heating components and is coupled to a vacuum pump. In the oven, the temperature and pressure could be changed to achieve the desired thermal conditions. Usually, samples may be placed in the oven, where they should be left overnight to dry entirely.
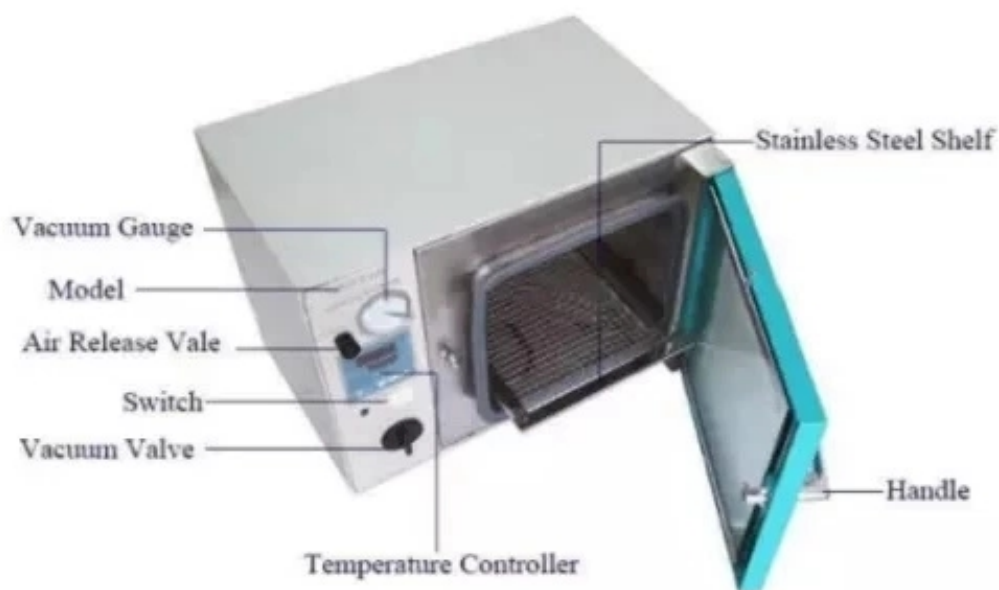
Figure 1.7: A conventional vacuum dryer for lab-scale utilization

Another type of lab-scale drying method is convection dryer or drying chamber (Figure 1.8) which is a type of convection dryer that uses heating to raise temperature and a blower to adjust convective heat transfer coefficient (h) through Reynolds number. It has to be equipped by an air outlet suction to remove the evaporated solvent such as NMP which is toxic.
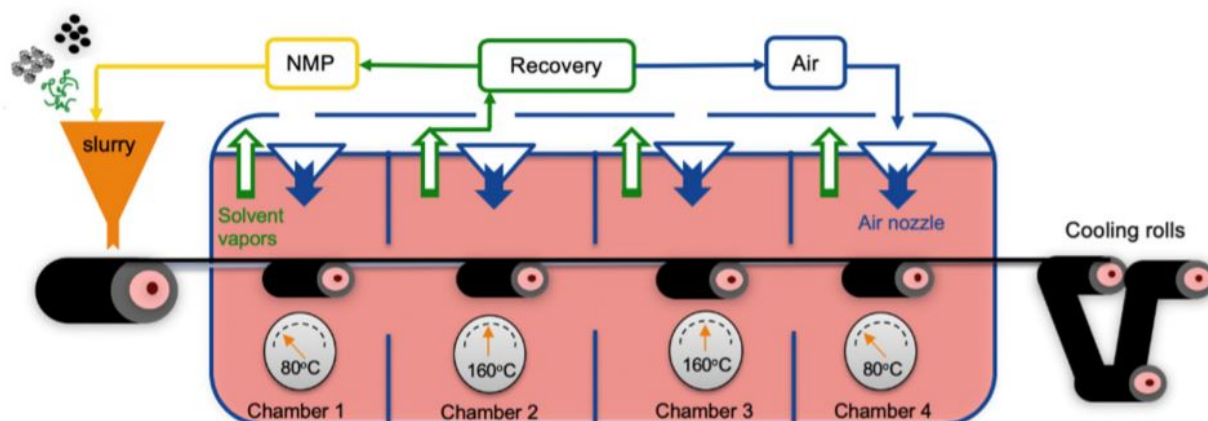
Figure 1.8: The electrode slurry is applied onto the Al foil, going through a typical four-stage industrial convection oven with flowing hot air, and the evaporated NMP is recovered. Reused from Bryntesen et al[17].

Calendering

The dried electrode should be positioned between two rolling cylinders that are smoothly rolling to press the dried electrode in the last step of film production. Based on the relevant factors, the operator can control the final thickness and movement speed. The dried electrode is then calendared to lower the thickness of the electrode, boosting 3D connection, electrical conductivity, and volumetric energy density [97]. The calendering process, which efficiently decreases electrical resistance and enhances energy density of the electrode at the expense of rate capability, is primarily responsible for porosity and pore structure. However, few research have investigated the impact of tortuosity and porosity on calendering in real time, as well as whether or not the same calendering approach should be used on electrodes of different thicknesses.[90]

Moreover, according to Zheng et al [98], the surge of capacity loss and rate capability are connected to excessive compression of calendering, because the high compression force of calendering process increases tortuosity and increase porosity of electrode which is unfavorable. In Addition, C.Lim's [67] study of the effect of calendering compression on $LiCoO_2$ found that a mild calendering compression on the cathode improves C-rate performance by increasing electrical conductor and more uniform pore and carbon black binder matrix distribution, which increases the electrochemically active surface area.

1.2.3. Coin Cell Assembly

After the aforementioned steps, the electrodes are ready for assembly, for this purpose, the electrodes should be cut into circular shapes with a specific radius depends on the size of casing. There are many types of coin cells. Their number is based on their dimensions, e.g., CR2032 represents a cell with a 23 mm diameter and a 2.5 mm thickness. For the purposes of consistency, all the cells used in our laboratory are of the CR2325 type[77].

Before the assembly process, the electrodes should be measured to estimate the active material weight, it would be necessary for battery tester input data. After the electrodes prepared for the coin cell assembly, they should be put inside the glovebox considering the safety protocols. A glovebox (or glove box) is a sealed container that is designed to allow one to manipulate objects including coin cells where a separate atmosphere conditions are desired. Built into the sides of the glovebox are plastic gloves arranged in such a way that the user can place their hands into the gloves and perform tasks inside the box without breaking containment. At least one side of the box is usually transparent to allow the user to see what is being manipulated. Two types of gloveboxes exist. The first allows a person to work with hazardous substances, such as radioactive materials or infectious disease agents, and the second allows manipulation of substances that must be contained within a very high purity inert atmosphere, such as argon or nitrogen. It is also possible to use a glovebox for manipulation of items in a vacuum chamber. The second type of glovebox is enough for the LIB laboratory to assemble the cells.

The casing material including upper case, bottom case, filler, and spring should be placed in the glovebox, should be kept in the oven and then in placed in the glovebox for at least 24 hours, to make sure that any types of contaminants and moisture are removed.

As the Figure 1.9shows, the mentioned parts should be assembled carefully and then be crimped with a coin cell crimper with appropriate pressure which normally between 90 psi and 110 psi. Cells should be conditioned for at least 2 hours in a static state at room temperature prior to electrochemical investigation, enabling the electrolyte to wet the electrodes and separator[77].

1.3. Characterization Techniques

The characterization techniques represent an important step forward in LIB industries because researchers and scientists are now able to obtain a more comprehensive understanding of how the different electrochemical processes affect the individual battery components under real operating conditions.
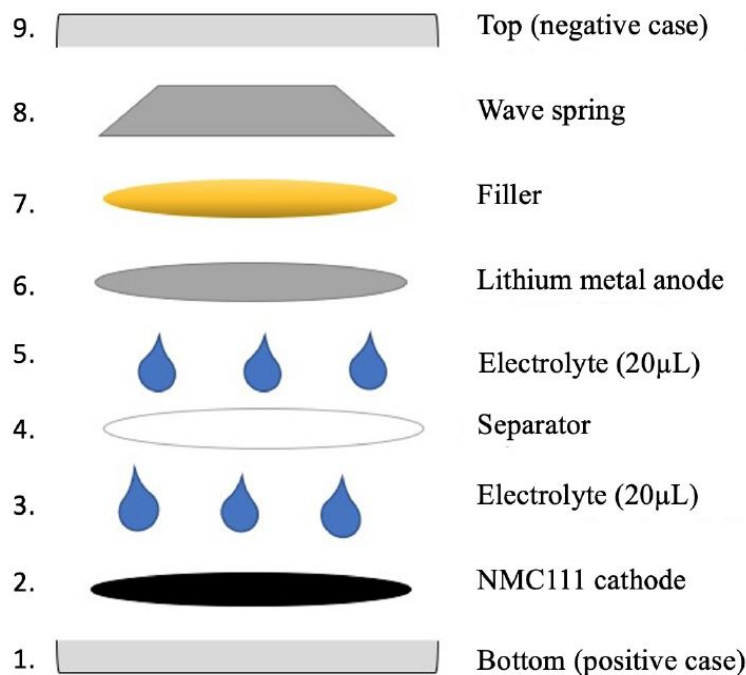
Figure 1.9: coin cell components

Many characterisation approaches established for materials science research are being studied to examine the initial and ultimate condition of battery components after cycling. for example, s canning electron microscopy (SEM), transmission electron microscopy (TEM), and hard X-ray microscopy are all used to check the morphology and homogeneity of electrode microstructures. The elemental composition and crystallinity of the materials are studied using NMR, electron dispersive X-ray spectroscopy (EDX) combined with electron microscopy (EM), and X-ray diffraction analysis (XRD). Surface analysis methods such as Raman spectroscopy, Fourier-transform infrared spectroscopy (FT-IR), X-ray photoelectron spectroscopy (XPS), and X-ray absorption spectroscopy (XAS) are also used to investigate the electrodes' surface and interfacial chemical environments. Characterizations within the device, on the other hand, are focused on the electrochemical characteristics of a cell. Battery cycle assessment, electrochemical impedance spectroscopy, and the galvanostatic intermittent titration technique are all common battery electrochemical techniques.[63].

Moreover, there are some characterization techniques that are classified as rheology characterization such as viscosity measurement of slurry. Also, scratch test is used for the effect of calendering process on the electrode.

Some characterizations are examined in each experiment to analyze the outcomes and investigate the specific impacts on the samples. In this project, two investigations are chosen

to assess the results of experiments which are scanning electron microscopy (SEM) and Galvanostatic cycling. The next subsections will go through each of these characterisation strategies.

1.3.1. Scanning Electron Microscopy (SEM)

As the Figure 1.10 the scanning electron microscope (SEM) produces images by scanning the sample with a high-energy beam of electrons. As the electrons interact with the sample, they produce secondary electrons, back-scattered electrons, and characteristic X-rays. These signals are collected by one or more detectors to form images which are then displayed on the computer screen. When the electron beam hits the surface of the sample, it penetrates the sample to a depth of a few microns, depending on the accelerating voltage and the density of the sample. Many signals, like secondary electrons and X-rays, are produced as a result of this interaction inside the sample.
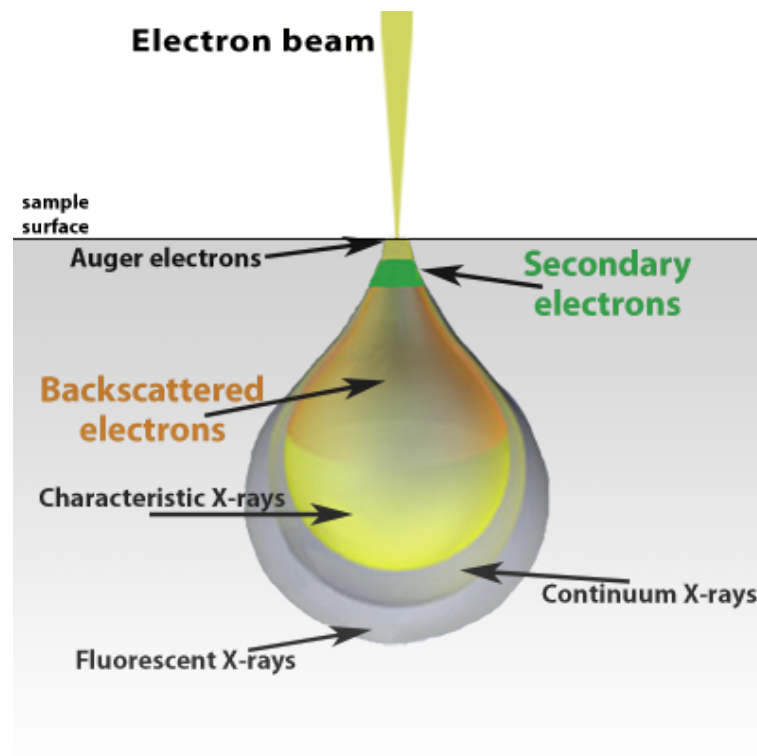
Figure 1.10: Schematic of electron beam interaction[34]

The maximum resolution obtained in an SEM depends on multiple factors, like the electron spot size and interaction volume of the electron beam with the sample. While it cannot provide atomic resolution, some SEMs can achieve resolution below 1 nm. Typically, modern full-sized SEMs provide resolution between 1-20 nm whereas desktop systems can provide a resolution of 20 nm or more.

1.3.2.   Electrochemical Characterisation

To research electrochemical processes and battery behaviors, a range of experimental procedures may be utilized with batteries.The most common and significant experiment carried out in the pursuit of better batteries is electrochemically charging and discharging a novel electrode material, and it is usually the first experiment that researchers and scientists seek when reading a report about new material.[77].

We can obtain a significant number of essential metrics for accumulator characterization, such as capacity or Coulombic efficiency, using this "cycling" approach. Following polarization, hysteresis, and over-voltage events may also be used to determine their health. Several representations of interest can be derived from the same data collection, each offering additional information. During galvanostatic cycling of batteries, the charge and discharge current are often expressed as a C-rate, calculated from the battery capacity. The C-rate is a measure of the rate at which a battery is charged or discharged relatively to its maximum capacity[77]. For example, a C-rate of 1 C means that the necessary current is applied or drained from the battery to completely charge or discharge it in one hour. C-rates multiples of 1 C are also exploited. In battery research, it is common to use a C-rate of 0.1C, so to charge and discharge a battery in ten hours. Since the capacity is expressed in Ampere per hour, calculating the current necessary to charge or discharge a battery is straightforward.

Applying a constant current (CC) to the battery and monitoring the voltage response is known as galvanostatic cycling. After a given length of time (charge) has passed, or after a specified voltage has been attained, the measurement is terminated.[77] As a result, a plot of voltage vs. capacity (time) is created, which is commonly referred to as the voltage characteristic. Under particular testing settings, the length of the curve indicates the accessible capacity (of a full-cell or a single electrode[13, 77].

Both thermodynamic and kinetic contributions are included in the characteristics. As a result, several factors can affect the shape of the curve, including the electrode's chemistry and crystallographic structure, and the current applied (often referred to in terms of C-rate, i.e. the electrode's working capacity divided by the desired amount of time for a full (dis)charge).[13, 77] For such reasons, CC cycling is commonly used:

1. The first experiment on a new electrode material was carried out in the studies. [77]

2. for characterizing (long-term cycling) cells and electrodes.

3. for creating (standard) cycle procedures that simulate LIB usage in the real world [13]

The discharge capacity divided by the previous charge capacity is known as Coulombic Efficiency (CE). The CE typically exposes parasitic reactions that suck charge away from the desired reaction, i.e. charging the electrode.[74, 75]. Hence CE is fundamentally defined as the ratio of Li^+ ions or electrons returning to the cathode to the quantity of Li^+ ions or electrons departing from the cathode in a complete cycle or the ratio of discharge capacity over the charge capacity and the equation 1.14 illustrates the CE:[50]

$$CE = \frac{Discharge\ Capacity}{Charge\ Capacity} \tag{1.14}$$

A LIB's CR is also a significant measure to consider. Cycle n+1's CR is calculated by dividing the measured discharge capacity of cycle n+1, $C_{Dch(n+1)}$ by the measured discharge capacity of cycle n, $C_{CDch(n)}$ (n). As the equation 1.15 shows the Capacity retention could be calculated as below:[80]

$$Capacity\ retention = \frac{C_{Dch(n+1)}}{C_{Dch(n)}} \tag{1.15}$$

n is representative of number of cycles. As the equation 1.16 shows, the term "Capacity Retention" could be defined in relation to the initial discharge capacity in the case of defining capacity retention after a period of cycling[80].

$$Capacity\ retention = \frac{C_{Dch(n)}}{C_{Dch(1)}} \tag{1.16}$$

The predicted capacity can be estimated by multiplying the mass of active material in the electrode by the active material's specific capacity (mAh/g) or measured by cycling the cell once or twice and proclaiming the 'initial' discharge capacity to be the expected capacity[77].

1.4. Analysis of Variance

The analysis of variance or ANOVA in brief is a statistical method that consists of separating the total variation of data set into logical components connected with specific sources of variation in order to compare the mean of two or more sets of values. ANOVA test is used to figure out that if testing groups have significant difference or not. In other words, the ANOVA test helps to figure out if it is needed to either reject the null hypothesis and accept the alternate hypothesis or the null hypothesis is valid [5, 31].

The null hypothesis can be thought of as a nullifiable hypothesis. It means that the

hypothesis can be nullify or be rejected and replaced by alternative hypothesis. In other words, the null hypothesis is a statistical theory that states that no statistical link or significant difference exists between two sets of observed data and measurable events in a given single observed variable. The alternative hypothesis is defined as a statement in direct opposition to the null hypothesis. When the test values fall into the rejection region as Figure 1.11 shows, the null hypothesis should be rejected and the alternative hypothesis is valid.

There are different ways to estimate group of results values and either support or reject the null hypothesis. The method should be selected depending mainly based on the Probability value or p-value in brief. P-value is a value that is used to justify the hypothesis statement. If the value falls in the rejection region, it means the results show statistically significant difference and null hypothesis can be rejected[5, 26].
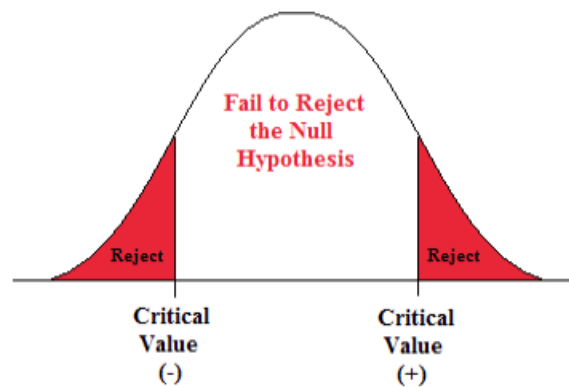
Figure 1.11: The rejection regions are shown in red in tailed curve, Source: www.courses.lumenlearning.com, [82]

1.4.1. One-Way and Two-Way ANOVA

A one way ANOVA is used to compare two means from two independent (unrelated) groups using a factor called F-distribution [6] (also called Fisher distribution). The null hypothesis for the test is that the two means are equal. On the other hand, the alternative hypothesis means that the two means are not equal[4]. On the other hand, Two-way analysis of variance is an expansion of one-way analysis of variance in which two independent components are included (variables). Each component has two or more levels, and treatments are created by combining the levels of two factors in any way conceivable[7].

2 | Experimental

The thesis consists of several experiments with different conditions for electrode drying. Each one of drying conditions has specific NMP drying rate which is provided by particular air velocity and temperature. The experiments are including the air velocity of 0.5 m/s for 50 °C and, 100 °C, and air velocity of 1 m/s for 50 °C and 100 °C. The air velocity could not be higher than 1 m/s due to the equipment technical limits, also it could not be lower than 0.5 m/s due to the safety considerations.

In the following sections, the experimental methods, related calculations, and investigations are going to be expanded. In this chapter, the whole process of half-cells production from slurry production to coin cell assembly will be discussed and compared for each one of the drying conditions. Additionally, the characterization techniques including cracks analysis (Scanning Electron Microscope), Galvanostatic cycling (rate test and long-term cycling) will be explained and discussed by details. The following steps are done for each one of the experiments.

2.1. Slurry Preparation

As mentioned in the theory part, the first step is slurry mixing and it starts from the selection of cathode material formula. The selected ratio for slurry mixing is standard ratio of 85:10:5 for cathode material, which means 85% weight ratio for active material (NMC111), 10% weight ratio for carbon black and 5% weight ratio for binder (PVDF). The PVDF is dissolved in the NMP solvent with the ratio of 1:20 wt% in the magnetic stirrer for at least 12 hours of mixing.

In next step, the total weight of slurry was set so that the required NMC and carbon black would be estimated through the equation 2.1. The desired solvent to powder material is 1:2 wt%. After the estimated NMC111 and carbon black added to the small special container the NMP-PVDF solution was added to the container and the pure NMP was added to achieve the desired powder to NMP ratio. The table 2.1 shows the detail of the components that are used in the experiment.

The total weight of material will be useful for drying process calculations. Hence, if the amount of NMP content of sample is known, it will be possible to make sure the drying process is finished whenever the NMP content is evaporated. In the slurry mixing procedure, the amount of each chemical component is usually given as a mass ratio (wt%), where the recipe can be calculated using equations 2.1 and 2.2.

$$Theoritical\ Mass = \frac{Weighted\ Amount}{Wt\%}.100 \tag{2.1}$$

$$Extra\ Solvent = (Solvent\ ratio.theoretical\ mass) - binder\ in\ solvent + binder \tag{2.2}$$

After the mentioned components are put together in the special container, the container should be placed in a centrifugal mixer (Thinky-Mixer ARE-250) to mix the slurry for 25 minutes at 1500 rpm and 5 minutes at 2000 rpm to obtain homogeneous slurry.

Table 2.1: Chemical components used in the experiments

Materials	Chemical name	Abbreviation	Supplier
Active material	NMC111	$LiNi_{1/3}Mn_{1/3}Co_{1/3}O_2$	Targray
Binder	PVDF	Polyvinylidene fluoride	Sigma-Aldrich
Conductive additive	Carbon black	C	Imerys

2.2. Coating

The facilities that are needed in this section is tape caster and doctor blade (or film applicator) the Figure 2.1 shows the film applicator that is used with dimensions. As Figure 2.2 shows, the model of tape caster (MSK-AFA-HC100) is supported with a vacuum pump for the heatable vacuum bed. For casting process, a four-sided film applicator (Figure 2.1)is used with its maximum raised gap, which is 200 μm, so the overall thickness of electrode including the aluminum foil thickness and slurry thickness is 200 μm before drying.

The first step of film processing is aluminum foil preparation, the aluminum foil as current collector should be completely neat, smooth and without wrinkles and contaminant. Therefore, the Aluminum foil should be cleaned and smooth cloth and laboratory ethanol with 99% purity.
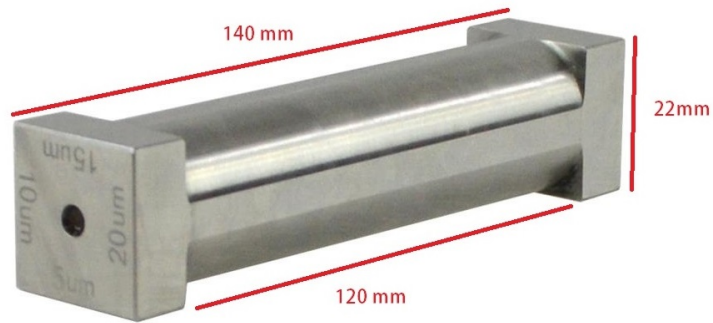
Figure 2.1: Film applicator with four different heights for coating from 50 μm to 200 μm, picture from the supplier company MTI

Figure 2.2: Tape caster with heatable vacuum bed and adjustable casting speed,picture from the supplier company MTI

The Aluminum foil should be laid down on to the tape caster vacuum bed to make sure that the foil sticks to the surface and does not move during the casting process. Then, the film applicator should be completely cleaned by ethanol and dried to make sure that any types of contaminants and dust are removed from the staff. Since the slurry contains toxic solvent of NMP for the safety reasons all the casting process should be done in the fume hood to make sure that toxic evaporation does not harm the operator's lungs . The slurry should be poured in front of film applicator and make sure that the heating element of the vacuum bed is off. Then, the tape caster starts to push the film applicator with the speed of 20 mm/s to cast the slurry evenly over the current collector.

2.3.   Convection Dryer

The drying method that is used for solvent evaporation of the samples is convection drying. The convection dryer able to adjust both the temperature and air velocity to achieve the desired evaporation rate of NMP solvent for each one of the experiments.

As the Figure 2.3 shows the convection dryer consists of drying chamber, air suction, heating elements accurate scales, air blower and temperature sensors which is connected to a computer. The computer adjusts the heating elements through the air temperature of the moving air. Moreover, the scales is connected to the computer to record the weight reduction of the sample. The air suction is installed right after the air outlet of drying chamber to remove the evaporated NMP which is toxic and flammable. The software that is used to control and record the data of experiment is written in LabVIEW software.

2.3.1.   NMP Evaporation

The sample which was placed in the convection dryer was exposed to air velocity and temperature. Since the electrode should be placed on the bottom of the drying chamber and top of the scales, the hot air passes over the electrode and the electrode could be consider as a simple plate for the estimations related to the convective heat transfer coefficient which the equation 1.4 shows. Since the air velocity is recorded continuously during the experiment it was possible to consider the average air velocity for the Reynolds number and heat transfer coefficient estimations. Moreover, since the Powder to solvent ratio is 1:2 in the following experiments, the weight of NMP content is 66% of the total content. Hence, whenever the estimated NMP content is evaporated, the drying process was considered as completed and the samples were post-dried at 120 C for 4 hours to remove NMP solvent residues.
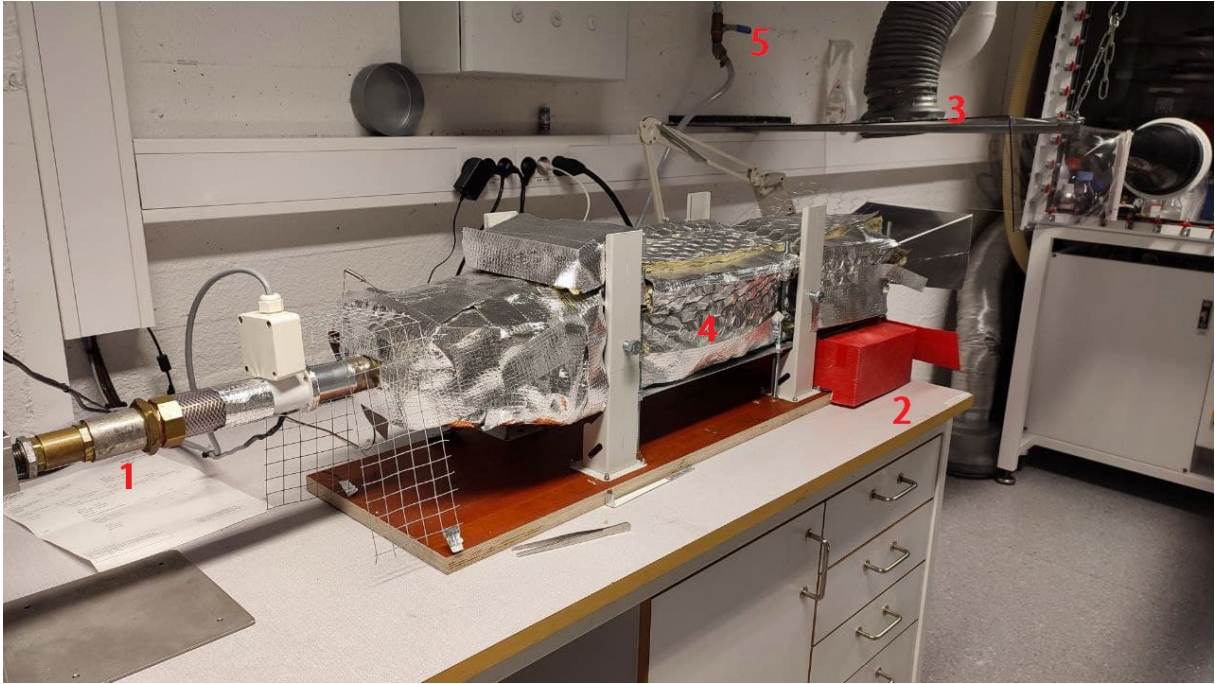
Figure 2.3: the convection dryer including: (1) Hot air inlet (2) Accurate Scales in protective shield, (3) Air suction, (4) Drying chamber, (5) Inlet air valve

2.3.2.   Energy Consumption

Another crucial factor that is estimated from the drying process for each experiment is energy consumption of drying per gram of electrode using equation 1.8. Based on the measurements of temperature of hot air, the accurate density of air was estimated based on the average of density, also as the Figure 2.4 shows the dimensions of the channel is 144×116 mm. Hence the mass flow rate was calculated using air velocity and average density of air. Moreover, since the specific heat transfer of air varies with the temperature, the average temperature of each experiment is used to estimate an average of specific heat transfer for the calculations. The inlet air is equal to room temperature (varied from 19 °C to 23 °C according to the measurements) because the blower intakes the air from the outside. Thus, the equation 1.8 was usable for the energy consumption calculations.

Air Compressor Energy consumption

The convective drying chamber was supported by a central industrial air compressor in another room, so the energy consumption estimation related to the blower was impossible. Hence, equation 1.11 is used estimate energy consumption of air blower considering each drying thermal condition. First, the mass flow rate is calculated from average air velocity of the experiment, air density (considering that air density varies with temperature) and
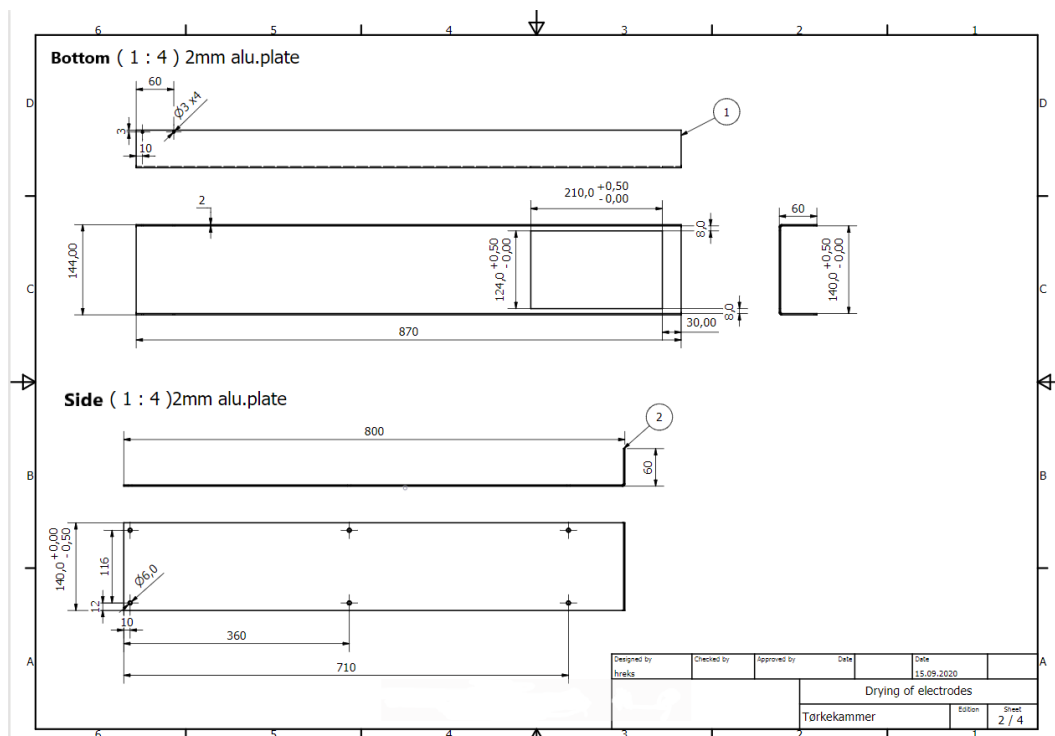
Figure 2.4: The sketch of the convection dryer shows the drying chamber from the side view and bottom view

the channel dimensions which is shown in Figure 2.4. The Psychrometric chart (Appendix A) is used for enthalepy estimations of air.

2.4.   Calendering and Electrode Preparation

The calendering process was necessary after the drying process as mentioned in theory part, in this project each sample was divided to two parts. One part was prepared for cracks analysis by Scanning Electron Microscopy and the other part was calendared for cell assembly.

The dried electrodes are cut by laboratory scissors, the part that should be used for coin cell assembly was calendared with 40 μm thickness. The calendering machine (MSK-HRP-01, MTI Corporation) with adjustable rotating speed and thickness is used for calendering. The range of the thickness of electrodes after drying and before calendering was between 45 μm to 70 μm so that to make sure that all electrodes are in approximately same thickness, 40 μm thickness was chosen. The speed of rotating was set on 10 mm/s and the thickness was set on 40 μm.

In the case that the time gap between the procedures was considerable for any reason the

samples were placed in a dry and clean environment to avoid the moisture and contaminant degrade the samples. Since usually drying and calendering process takes longer than other procedures, the samples were put in a dry box. The dry boxes gauge pressure is equal to atmosphere pressure, but they are isolated from free air and kept dry by silica gels which are placed in bottom of the box.
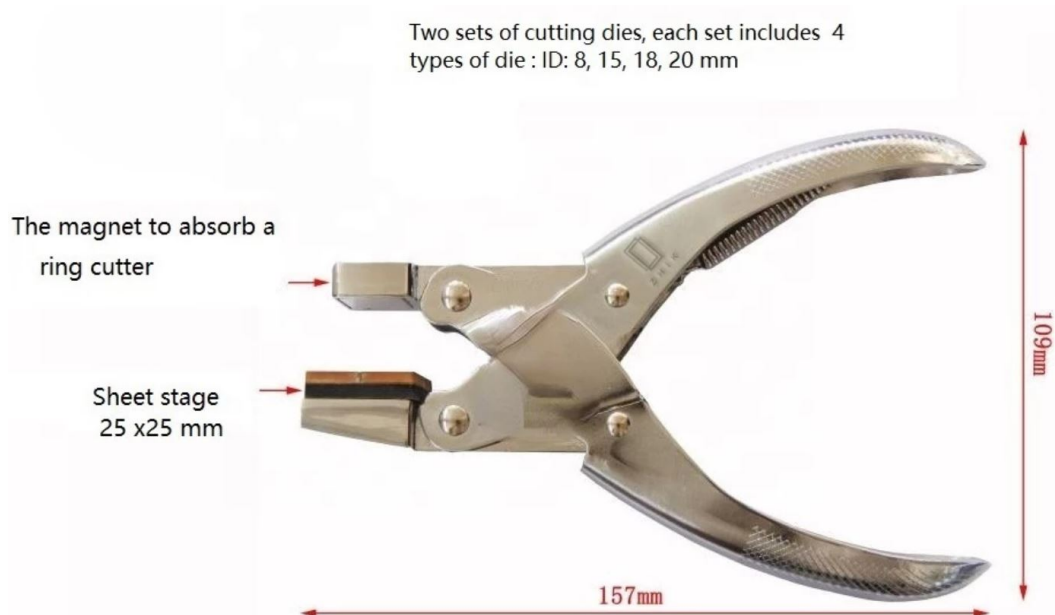
Figure 2.5: Manual Disc Cutter Punching Tool For Button Cell Battery Electrode

After the calendering process of electrodes were done, the electrodes were cut by electrode puncher into the desired radius as shown in Figure 2.5. In the following experiments the desired radius of electrodes is equal to 7.5 mm.

2.5. Coin Cell Assembly

Since the electrodes are cut by the punching tool described before, they are ready for coin cell assembly. However, before the process all components of coin cell assembly including, electrodes, casing components and separators were dried and kept in the glovebox for at least 12 hours.

The assembly process was mainly done in the glovebox, where the gauge pressure, moisture and O_2 were under control and was filled by an inert gas. As explained before, in the Figure 1.9 the operator should place the cathode electrode on the negative cap and pour 20 μL of electrolyte (Lithium hexauorophosphate($LiPF_6$)) on the cathode then the separator was taken place on the wet cathode, another 20μL of electrolyte was poured on the separator and put the anode on it. The anode was brushed before the assembly to make sure that

Table 2.2: The SEM settings of pictures

Apparatus	Working distance	Accelerating voltage (EHT)	Magnitude
Zeiss Ultra 55VP	36-44 mm	10 KV	300x

the lithium plate is smooth and free from any kind of oxidations so it could be perfectly tapped on the electrolyte. The first step of coin cell assembly was finished by taking place of filler, spring, and the positive cap on top of each other.

The next step of assembly is crimping which is done by a crimper in the glovebox. The crimper (MSK-PN110-S) that is used for the assembly was supported by a pneumatic power,and the coin cells were pressed by the pressure of 90 psi. Since the electrolyte is toxic, the assembled coin cells were kept in the glovebox for at least 24 hours to make sure that the leaked (if any) electrolyte is evaporated so it is safe to remove from the glovebox for the galvanostatic cycling.

2.6.   Characterization Methods

Conventional characterization techniques on LIBs are applied to either the materials within the device (such as electrodes and electrolytes) or the device itself. To characterize the coin cells, cracks analysis and galvanostatic cycling were used in that sequence.

2.6.1.   Scanning Electron Microscopy and Cracks Analysis

With the aim of taking SEM pictures of the surface of samples, the dried electrodes were mounted on the sample holder. As the Figure 2.6 shows, the sample holder took place in an isolated metal vessel where the backscattered electron detector, and magnetic lens were right above the sample holder and the secondary electron detector was located diagonally next to the back-scattered electron detector.

The samples were separated to four groups based on the drying conditions, and each condition repeated for at least three times to increase the accuracy and estimate the variability of each conditions. For each one of the samples at least 15 SEM pictures were taken which means more than 200 SEM pictures were taken for all drying conditions. Table 2.2 shows the settings of the SEM pictures that are investigated in this study.

After the scanning electron microscopy has been done by the SEM instrument(Zeiss Ultra 55vp) the pictures were imported in tif formats and they were analyzed by a software called ImageJ(version 1.53). ImageJ can detect the cracks and based on the scale of the picture
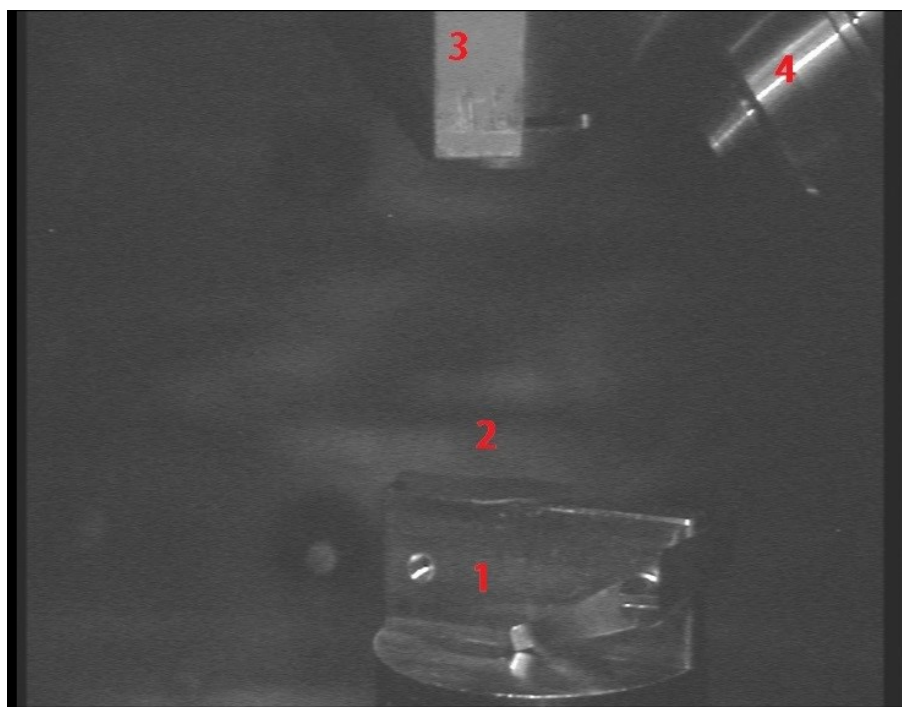
Figure 2.6: (1) Sample holder, (2) electrode which is sticked to the sample holder (3) the back-scattered electron detector, and magnetic lens (4) secondary electron detector(The picture is taken in NTNU SEM laboratory)

it can estimate the area of the cracks and generate the list of cracks and the dimensions in a CSV file which is useful for the further analyses.

2.6.2. Galvanostatic Cycling

In the galvanostatic cycling section, the assembled coin cells were cycled to study on the electrochemical performance of coin cells. The cycling tests could be very useful for the final analysis to find the optimum drying rate of electrodes besides the cracks analysis.

For the purpose of battery cycling analyses, a laboratory scale battery tester is taken into service from Arbin Instruments company and all the cycling programms are written with the Arbin instruments software (MITS PRO). All the tests are done in the controlled temperature of 34 °C for two types of tests which are rate test cycling and long-term cycling.

Rate Test Cycling

During the rate test cycling the charge and discharge of batteries in different C-rates and its effect on the discharge capacity were investigated. The C-rates changes every five

Table 2.3: Rate test cycling and long term cycling programs with different discharge C-rates and voltage in range of 3 to 4.3 V

Cycle	Charging		Discharging
	C-rate	CV	C-rate
1-5	C/10	-	C/10
6-10	C/5	4.3	C/5
11-15	C/2	4.3	C/2
16-20	C/2	4.3	C
21-25	C/2	4.3	2C
26-30	C/2	4.3	3C
31-35	C/2	4.3	5C
36-40	C/10	-	C/10
41-140	C/2	-	C/2

cycles, and the test started from the lowest C-rate which is C/10 to the highest C-rates with 5C and it returns for C/10 for the last five cycles. The table 2.3 shows the variation of C-rates for charge and discharge during the rate-test cycling.

Each of the drying conditions were undergone the rate test cycling for at least three coin cells in order to make sure that the results are consistence and are not affected by random events.

Long-term Cycling

During the long-term cycling the charge and discharge of the coin cells in one specific C-rate which was equal to C/10 C for the first 2 cycles and then it increases to C/2 C for the next 100 cycles. The aim of the test is to test out the discharge capacity retention during long-term usage , and CE investigations for each group of experiments.

In order to apply the charge and discharge on coin cells based on the desired purpose, a program should be written in the Arbin software, Figure 2.7 shows a diagram that clarifies the logic behind the program of long-term cycling.
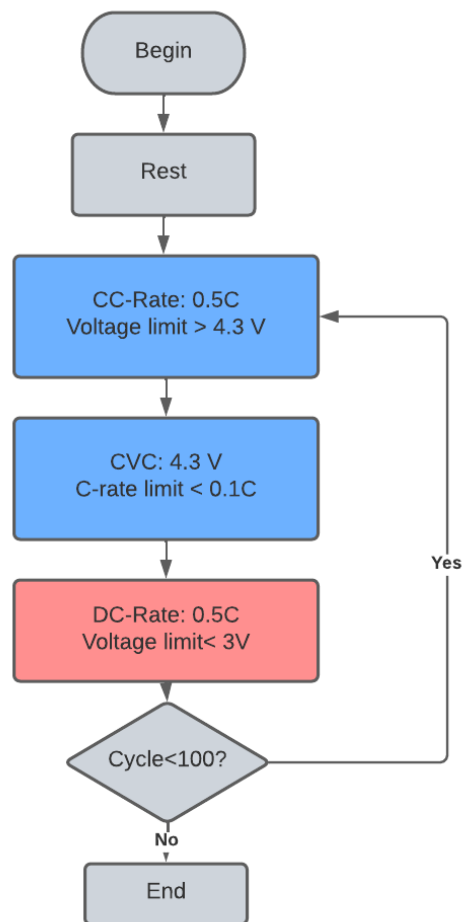
Figure 2.7: Flow chart of long-term cycling test

3 | Results

In the following chapter, the results of experiments will be presented, and related analysis will be discussed. The first section would be dedicated to the energy consumption and drying processes and the results of each group of experiments would be discoursed. The results of convection drying process can provide ideas about the most and the least energy consuming drying procedure. Moreover, it illustrates the drying rate system of each thermal conditions.

The second section of chapter is devoted to cracks analysis and its relation to the thermal condition of drying process. The results of cracks shows that which drying procedure might be the best way of electrode drying.

The next section represents the electrochemical performance of battery cells, since the electrodes of battery cells have passed different ways of drying processes, the results of battery cycling could be a key clue to figure out the best procedure of drying.

The last section puts all the results together to find out the most optimum approach of drying in terms of energy consumption and electrochemical performance.

3.1. Drying Process and Energy Consumption

In the following sections the results of drying rate of each thermal conditions will be presented based on the results of experiments. In addition, the energy consumption of each drying conditions will be presented and compared to other conditions to figure out the lowest energy consumption. At the end, the presented results will be discussed and compare to the calculations.

3.1.1. Drying Rate

As mentioned before the drying conditions are separated to four different thermal conditions based on temperature and air velocity. Based on the equation 1.7, the drying rate for both the constant rate period and drying rate period are calculated. Since three exper-

iments were done for each drying conditions the standard deviations both for $X_{critical}$ and constant drying rate are calculated and shown in the following table. Based on ANOVA which is described in the theory part, all the drying conditions characteristics can be compared to each other since the P-values are less than 5%.

Table 3.1: The drying rate during constant rate period and critical moisture content of each drying conditions $X_{critical}$

Experiment Code	V1T50	V1T100	V05T50	V05T100
Air Velocity (m/s)	1	1	0.5	0.5
Drying Temperature °C	50	100	50	100
Constant Drying Rate (g/m^2.s)	0.0095	0.042	0.0057	0.0196
$X_{critical}$ (Kg_{NMP}/Kg_{dry})	0.38	0.41	0.34	0.41
Standard deviation of Constant drying rates	0.00084	0.0018	0.0015	0.0029
Standard Deviation of $X_{critical}$	0.011	0.085	0.026	0.077

As the table 3.1 shows, the constant drying rate is a function of temperature and air velocity. The extremer the thermal condition the higher the constant drying rate. The temperature of 100 °C and air velocity of 1 m/s has the highest constant drying rate which is 0.042 g/m^2.s. The $X_{critical}$ is in the range of 0.34 to 0.41 for all the thermal conditions. However, the in the temperature of 100 °C for both air velocities the $X_{critical}$ is higher than the temperature of 50 °C.

3.1.2.   Energy Consumption Results

The energy consumption of each thermal condition is calculated using equation 1.8, equation 1.11 and equation1.13 for the whole period of drying process with respect the conditions of each experiment as explained before. The thermal energy consumption and blower energy consumption is considered together in order to have a fair comparison. The following histogram shows the total energy consumption per each gram of produced electrode for each of the drying conditions. As the Figure3.1 illustrates the energy consumption for drying of each gram of electrode for V1T50 is equal to 5.6 kWh/gr due to higher air velocity which requires more power for air blowing and more heat to increase temperature of air flow. Moreover, since the drying rate is as low as 0.0095 g/m²s, the required time of drying for electrodes increases which lead to greater energy consumption. On the other hand, V05T50 with drying rate of 0.0057 g/m²s consumed 32% less energy in comparison with V1T50 due to lower air velocity.

In addition, V1T100 with air velocity of 1 m/s and 100°C consumed 2.63 Kwh for each gram of electrode which is only 5% greater in comparison with V05T100 with same temperature while the drying rate of V1T100 approximately twice V05T50. The standard deviations of energy consumption are estimated based on the same three samples that are used in galvanostatic cycling. Hence, the energy consumption of electrodes can be compared based on specific discharge capacity later on discussion chapter.
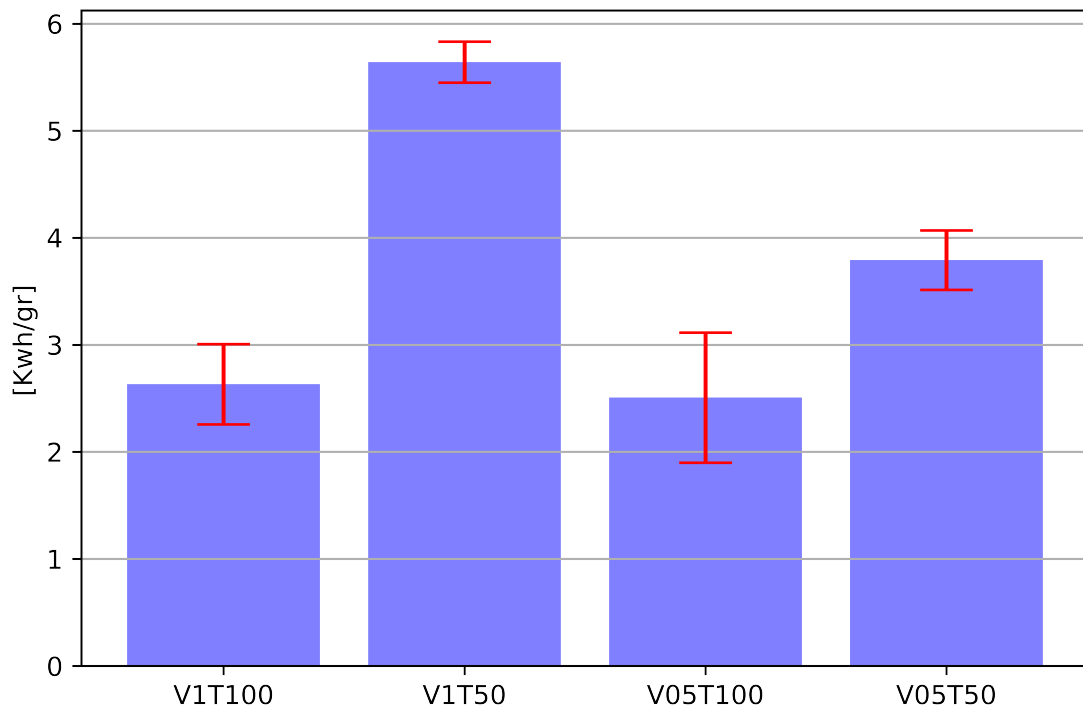
Figure 3.1: Energy consumption for drying of one gram of electrode for each procedure of drying

3.2.   Scanning Electron Microscope Results

For crack analysis investigations, five samples for each drying conditions were prepared and studied by SEM. As Figure 3.2 illustrates, cracks with reasonable area should be considered. Hence, The cracks are sorted in range of 10 μm^2 to 300 μm^2 which are classified by 10 to 20μm^2, 20 to 30 μm^2, 30 to 50 μm^2, 50 to 100 μm^2, 100 to 200 μm^2, 200 to 300 μm^2 and larger than μm^2. The number of cracks per area (number of cracksμm^2) is estimated and classified based on the size. Based on ANOVA all cracks of thermal conditions with same drying air velocity have statistical difference and could be compared. On the other hand, the comparison between thermal conditions with different air velocity and same drying temperatures only have statistical difference for cracks with

equal and larger than 300 μm^2. Hence, the following histograms only compare the data with significant difference based on ANOVA method.
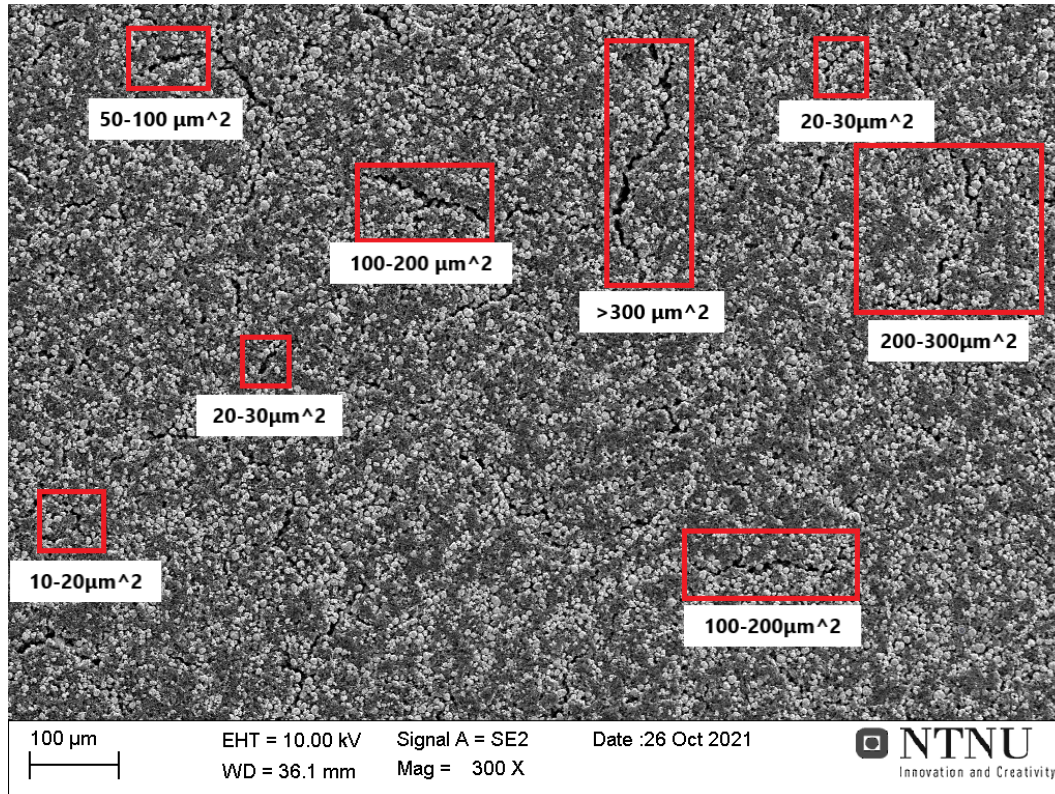
Figure 3.2: Example of SEM picture of V1T100 with recognized cracks

As Figure 3.3 shows the thermal condition with 1 m/s of hot air velocity the number of cracks has a considerable reduction with the temperature of 50 °C in compare with 100 °C, especially in cracks with larger than 200 μm^2.

The Figure 3.4 presents the experiments with 0.5 m/s for 50 °C and 100 °C, the difference of cracks quantity per area between 50 °C and 100 °C increases from small cracks to larger cracks as the same way as the experiments with 1 m/s. Furthermore, based on above histograms (Figure 3.3 and Figure 3.4) the number of cracks per area with 0.5 m/s of air velocity is considerably lower than number of cracks per area with 1 m/s of hot air velocity.

The cracks results could be presented in another way which classifies the share of cracks area (based on the size of cracks) over the total investigated area. The following histogram presents percentage of cracks area and the comparison of drying conditions. The Figure 3.5 shows the comparison of drying conditions of 50 °C and 100 °C in 1 m/s of hot air velocity, based on the histogram in a temperature of 100 °C, the share of larger cracks are considerably higher than the drying condition with a temperature of 50 °C, on the
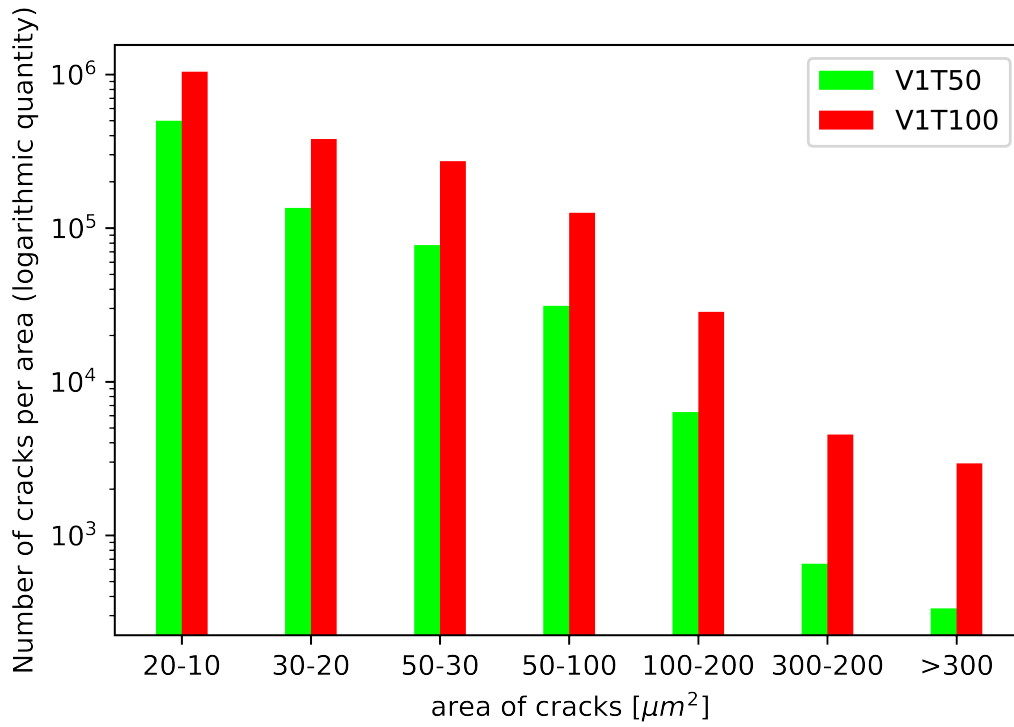
Figure 3.3: Comparison between V1T50 and V1T100 for cracks per area
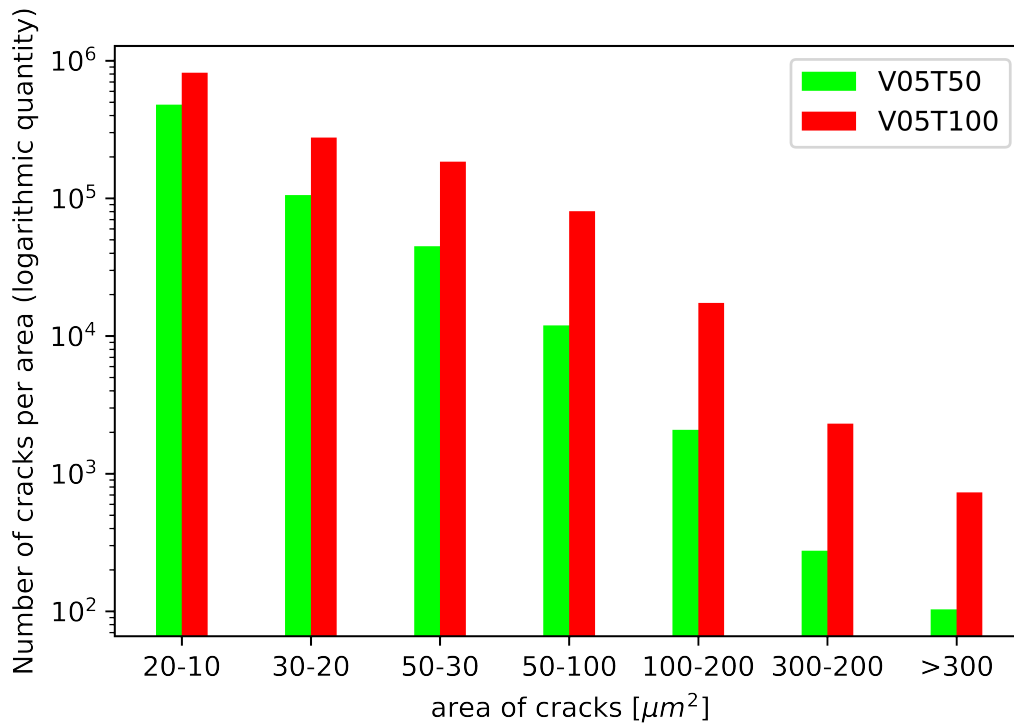
Figure 3.4: Comparison between V05T50 and V05T100 for cracks per area

other hand, in the lower temperature the share of smaller cracks is significantly larger than higher temperature.
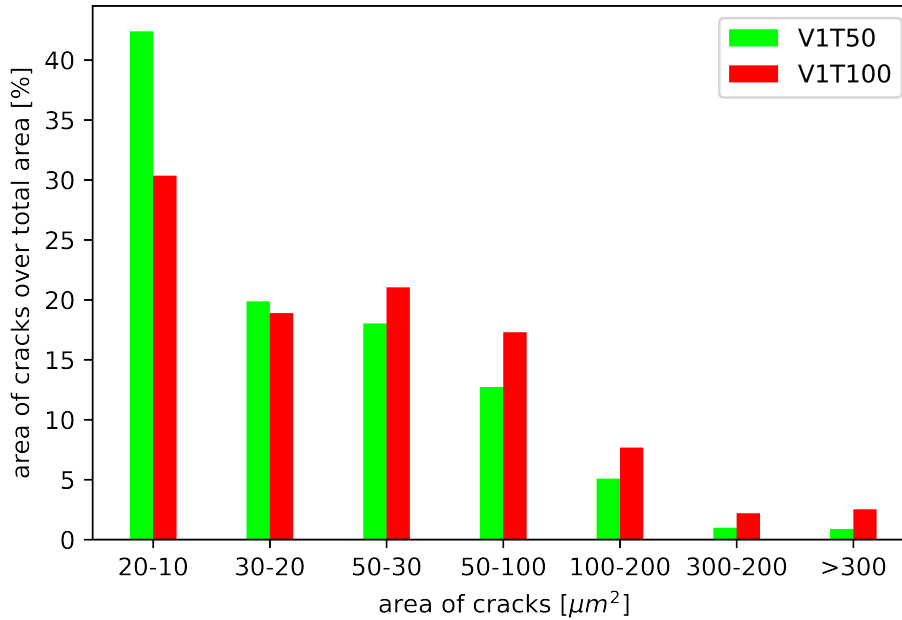
Figure 3.5: Share of cracks area over the total investigated area for V05T50 and V05T100

As Figure 3.6 illustrates, as the same way as the drying conditions with hot air velocity of 1 m/s, in the drying conditions with 0.5 m/s of hot air velocity for the temperatures of 100 °C and 50 °C, The proportion of medium and big cracks (larger than 50 μm^2) are much greater in the drying condition at 100 °C than in the drying condition at 50 °C, whereas the share of smaller cracks (smaller than 50 μm^2) is significantly higher in the lower temperature.

in the midst of the all presented histograms and results the drying condition of V1T100 has the highest proportion of crack area over total area for large and medium cracks and the V05T50 has the lowest proportion of crack area over total area for large cracks. On the other hand, the area of small cracks over total area have obviously larger proportion for the drying conditions of V05T50 and V1T50.

3.3. Galvanostatic Cycling Results

In this section the results of electrochemical performance of half-cells will be presented. As stated in the experimental chapter, the coin cells were cycled using a rate program (40 cycles) followed by a long term cycling (100 cycles), which will be presented separately in
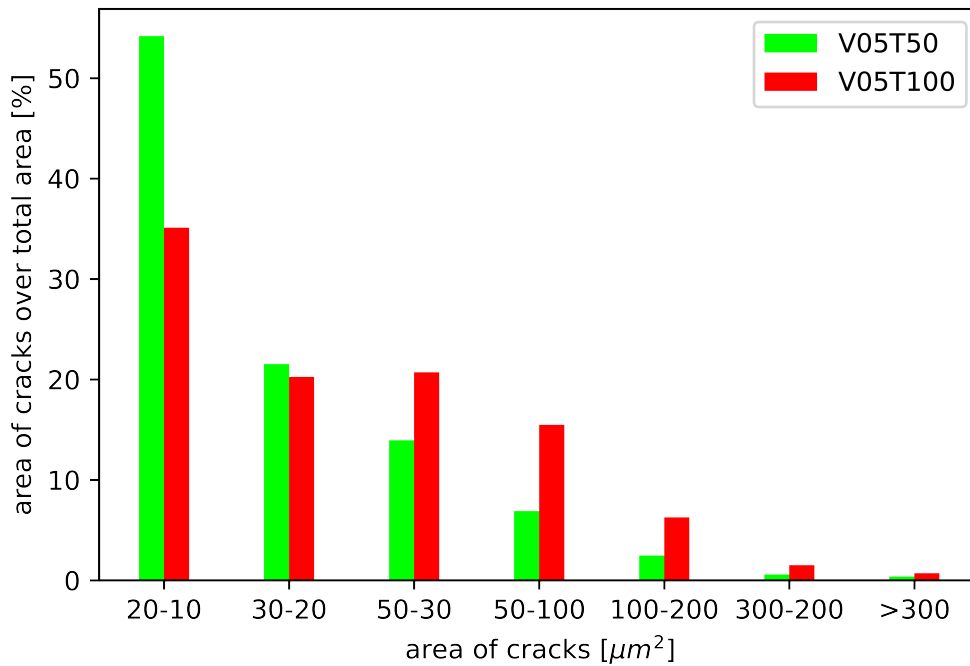
Figure 3.6: Share of cracks area over the total investigated area for V05T50 and V05T100

the following parts.

3.3.1. Rate Test Cycling Results

As the table 2.3 shows in the chapter two, the coin cells were undergone different C-rates to assess the discharge capacity of coin cells. For the purpose of repeatability, the results of three parallel half-cells which were undergone same process will be presented in one chart.

The Figure 3.7 illustrates the electrochemical performance of V05T50 for three parallel samples. The highest specific discharge capacity is for C/10 which is approximately 163 mAh/g for all samples. As the C-rate increases, the specific discharge capacity falls to the lower values. The first considerable fall of specific discharge capacity is for switching the C-rate of 2C to 3C, in which the specific discharge capacity decreases from about 130 mAh/g to less than 120 mAh/g. Finally, in the C-rate of 5C, all samples fell to less than 80 mAh/g. After the C-rates decreased to C/10 again, the specific discharge capacity of samples turned back to the initial values with minor capacity fade.

The Figure 3.8 shows the results of the cells of V05T100 which are dried by temperature of 100°C and air velocity of 0.5 m/s. The highest specific discharge capacity is 160 mAh/g
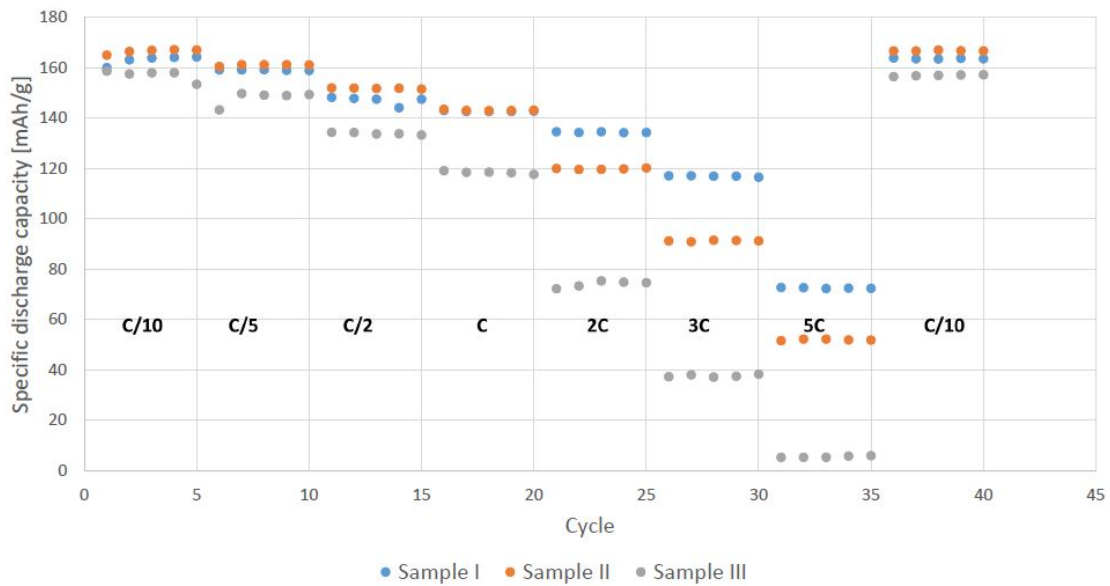
Figure 3.7: Rate test cycling for the experiments with 0.5 m/s hot air velocity and temperature of 50°C
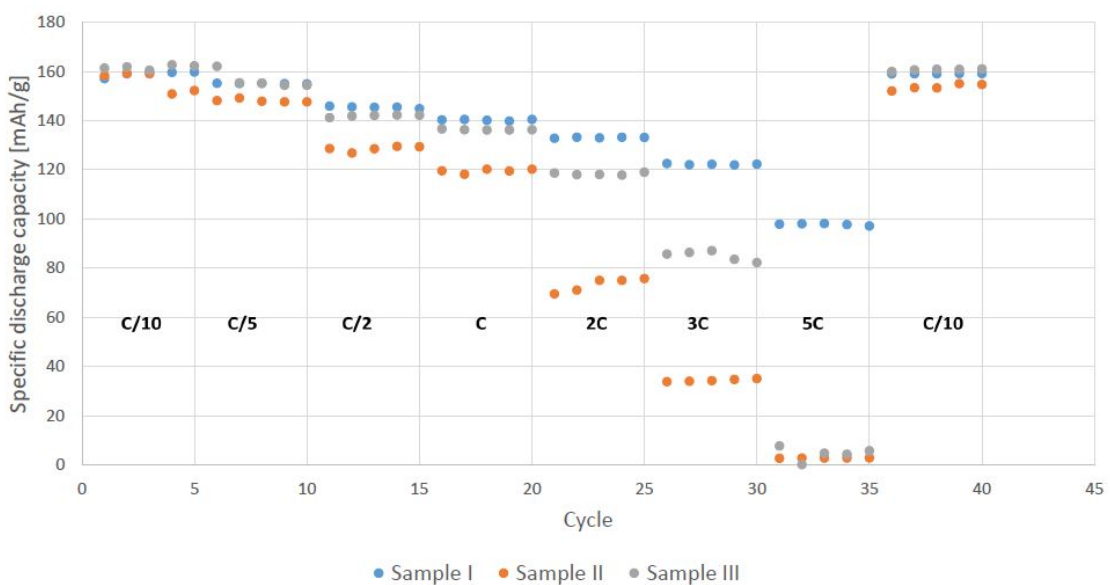
Figure 3.8: Rate test cycling for the experiments with 0.5 m/s hot air velocity and temperature of 100°C

for C-rate of C/10 and for the C-rate switching from C to 2C, the specific discharge capacity decreased from 120 mAh/g to 80 mAh/g for sample II, while the other two samples showed better performance. However, in C-rate of 5C sample II and sample III fell down to less than 5 mAh/g.

On the other hand, sample I reduced to 100 mAh/g in 5C. The electrode of sample I is produced from drying test of 20KV05T100-part1 and it performed considerably better. It is worth to state that, as the appendix A shows the cracks larger than 200 μm^2 occupied less proportion of cathode's area in comparison with other samples which lead to faster lithium ion diffusion in the electrode and better electrochemical performance.
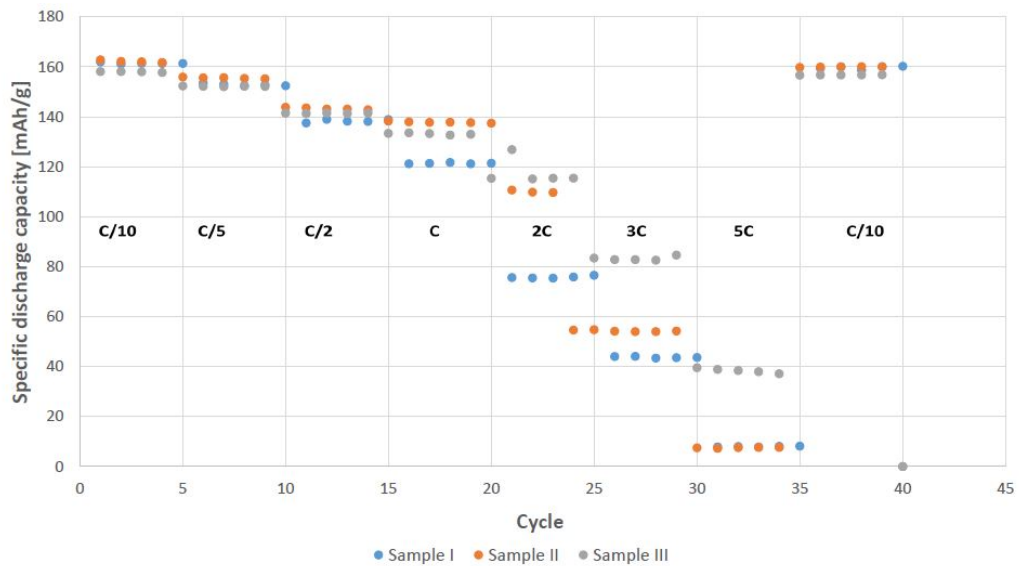
Figure 3.9: Rate test cycling for the experiments with 1 m/s hot air velocity and temperature of 50°C (V1T50)

Figure 3.9 displays the results of experiment V1T50 that is dried under thermal condition of 50°C and 1 m/s, the initial specific discharge capacity is equal to 160 mAh/g for all samples and all three samples perform approximately the same. After C-rate of 5C the specific discharge capacity of samples raised again to the approximately same as initial specific discharge capacity in first five cycles.

Figure 3.9 shows the group of experiment V1T100 for three samples, the initial specific discharge capacity of sample I and sample II are equal to 160 mAh/g and the trend of capacity reduction to deduction of C-rate are similar. Both samples fell to less than 5 mAh/g for C-rates of 3C and 5C and raised to about 160 mAh/g for C-rate of C/10. However, Sample III starts from 120 mAh/g at C/10, which is considerably lower than other samples, and shows less reduction in response to higher C-rates. It could be stated
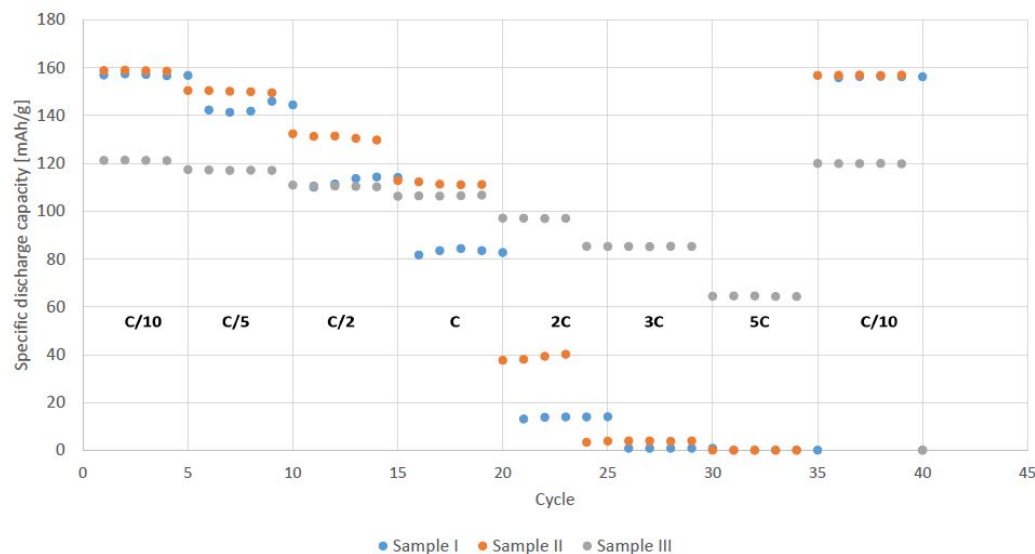
Figure 3.10: Rate test cycling for the experiments with 1 m/s hot air velocity and temperature of 100°C (V1T100)

since the V1T100 electrodes are produced in the extreme condition, these are more fragile in comparison with other electrodes. Hence, it could be possible that the electrode of sample III lost a portion of the material during the coin cell assembly. In that case, the active material weight used to calculated the specific discharge capacity in the cycling plot is too high which results in a lower overall specific discharge capacity. Moreover, the lost part of the electrode might be filled by electrolyte and act as pores. Consequently, the lithium ions diffuse faster in that part of the electrode and it leads to significantly higher specific discharge capacity at large C-rates. Hence, sample III will be dismissed in the discussion part and will not be considered.

In the following chart, the specific discharge capacity based on C-rate for V05T50 and V05T100 are compared with standard deviations. Figure3.12 shows that the trend of falling specific discharge capacity of V05T100 is slightly sharper than V05T50 in specially switching C-rates from 3C to 5C. additionally, the standard deviation of V05T100 is considerably higher than V05T50 since sample I performed better than others due to less formation of larger cracks during the drying process.

In terms of rate test cycling evaluation based on the impact of cracks formation on the electrochemical performance, it is worth to compare V05T100 and V05T50 rate test cycling results again without sample I. In Figure 3.13, V05T100 has lower standard deviation in comparison with V05T50. Apparently, Figure 3.13 admits that V05T100 performance is considerably inferior in high C-rates like 2C, 3C and 5C in comparison with V05T50.
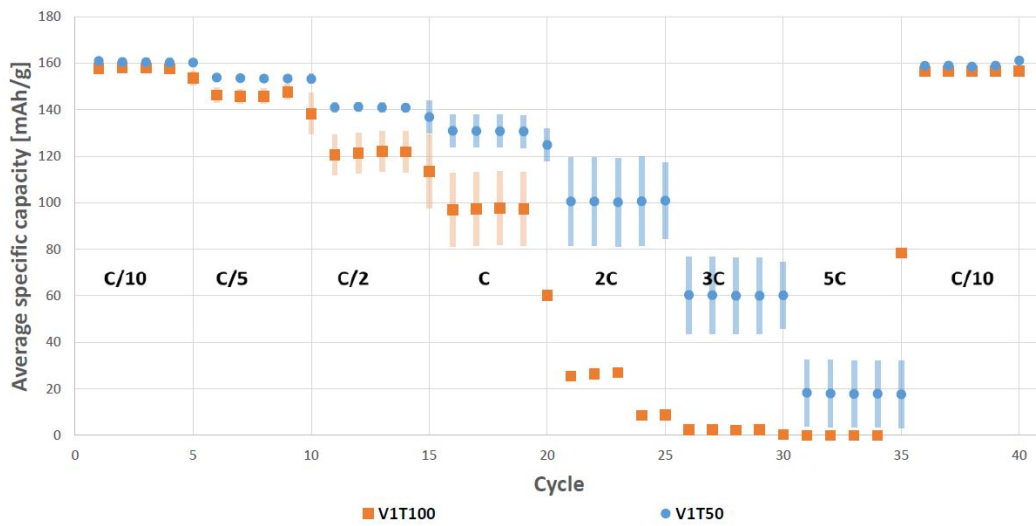
Figure 3.11: Specific discharge capacity of V1T100 and V1T50
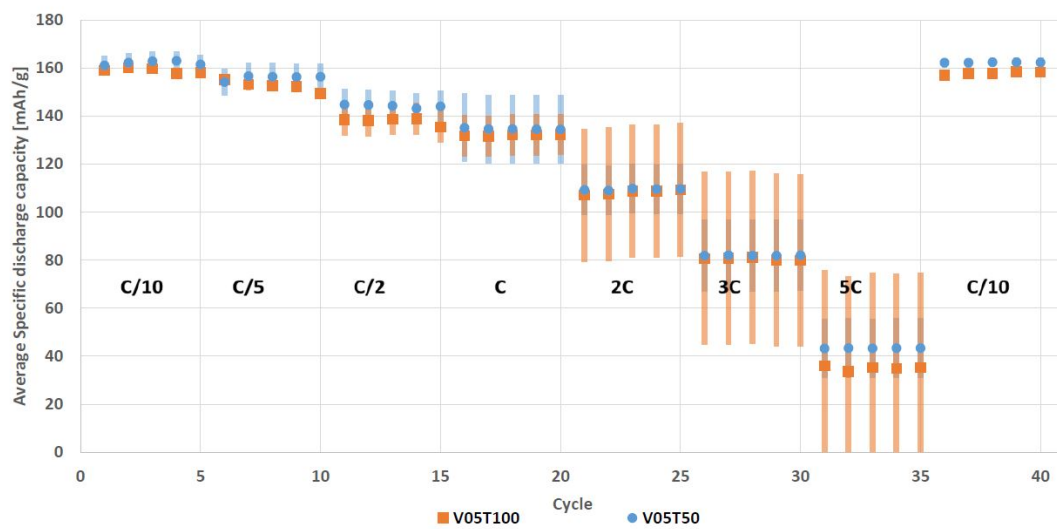
Figure 3.12: Specific discharge capacity of V05T100 and V05T50
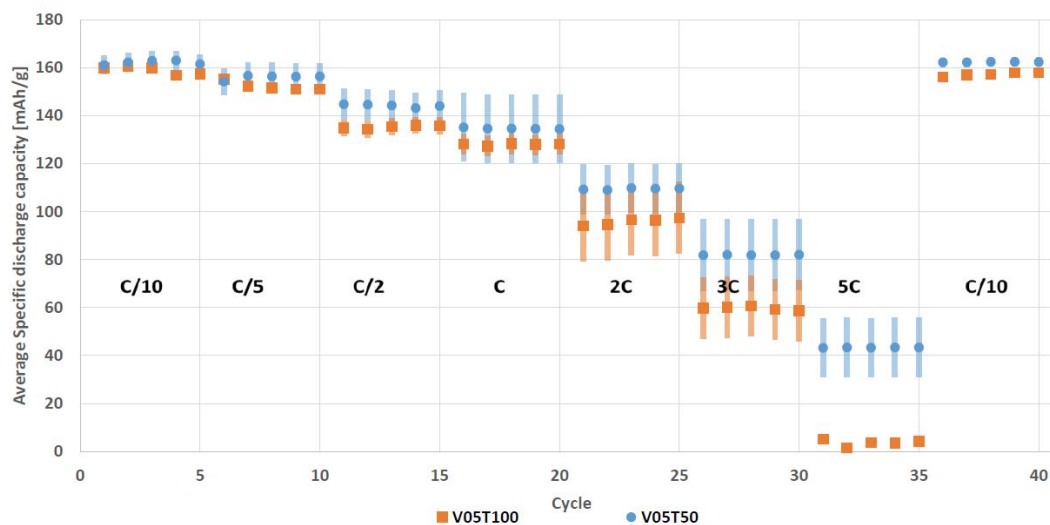
Figure 3.13: Specific discharge capacity of V05T100 without sample I and V05T50

3.3.2. Long Term Cycling Results

In this section the results of long term cycling will be reported, the average specific discharge capacity trend and CE of three coin cells after 100 cycles will be shown with standard deviations in form of scatter charts and histograms. Since the long term cycling is performed after the rate test cycling, the charts start from the cycle number 40 and close at the cycle number 140. The CE and capacity retention of V05T50 is shown in the following figure3.14. The chart illustrates that the specific discharge capacity which is equal to 143 mAh/g in the cycle of 40 and drops to 141 mAh/g at cycle number 140. Moreover, The CE starts with 99.5 % and decreases to 99.9 % which can be considered as constant value.

In the next Figure3.15 the specific discharge capacity and CE of V05T100 is shown, the specific discharge capacity starts with 139 mAh/g on the cycle number 40 and reduces gradually to 134 mAh/g on the cycle number of 140. However, the CE remains approximately constant on the value of 99.25% during the cycling.

The next chart (Figure3.16) presents the specific discharge capacity and CE of V1T50, the specific discharge capacity on cycle number 40 is equal to 135 mAh/g and it gradually decreases to the value of 129 mAh/g. On the other hand, the CE decreases from 99.4% to 98.8% after 100 cycles. The last chart displays the specific discharge capacity and CE of V1T100. As the Figure3.17 shows, the specific discharge capacity of cycle number 40 is 129 mAh/g, while after 100 cycles it decreases to 124 mAh/g. The CE remains
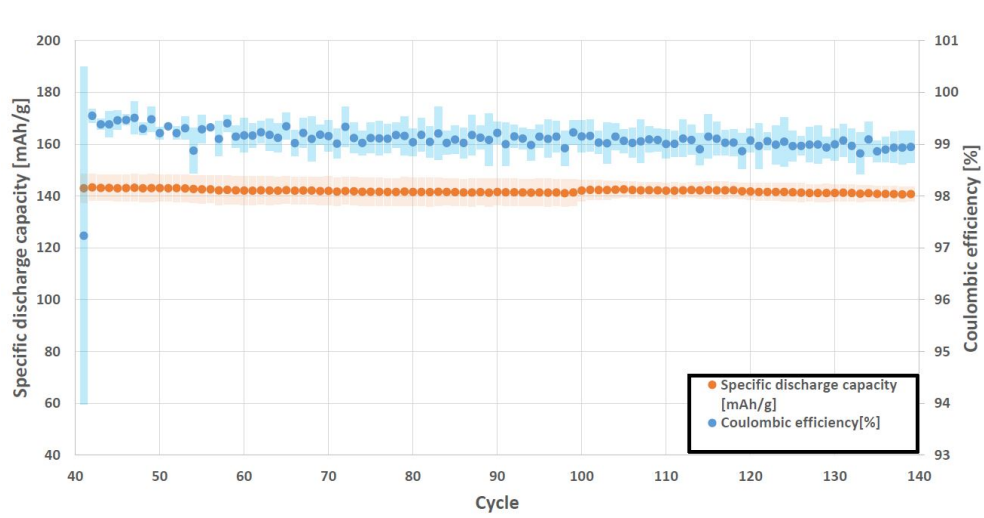
Figure 3.14: Average specific discharge capacity trend and CE of V05T50
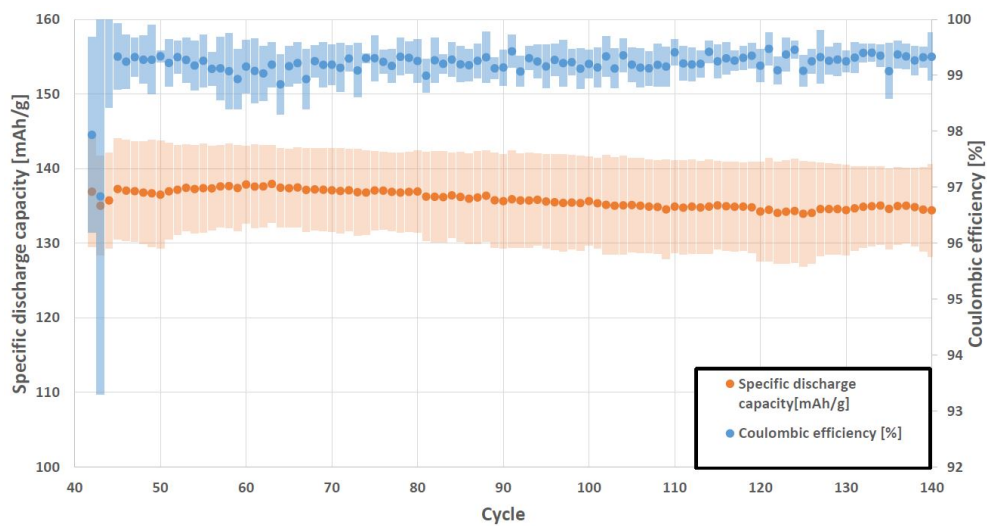
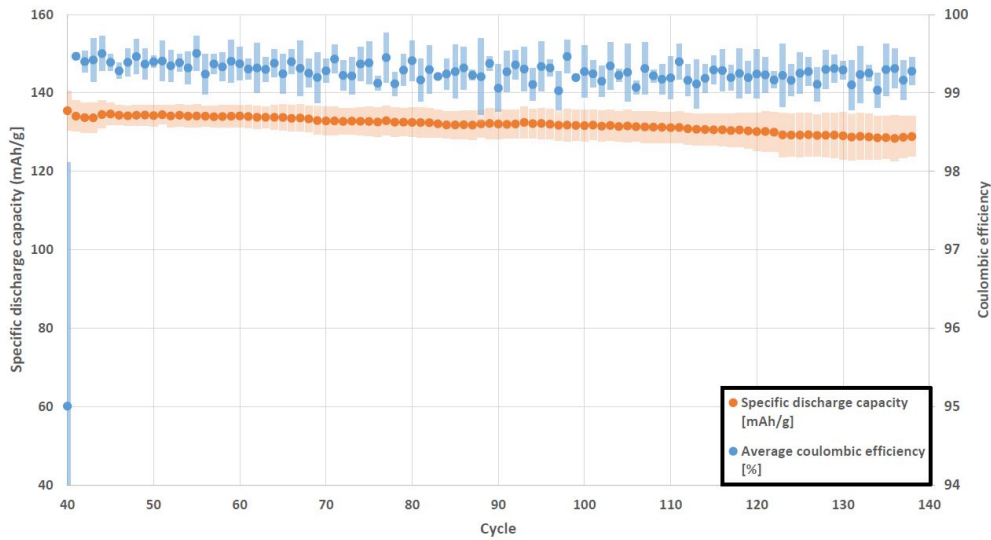Figure 3.15: Average specific discharge capacity trend and CE of V05T100

Figure 3.16: Average specific discharge capacity trend and CE of V1T50

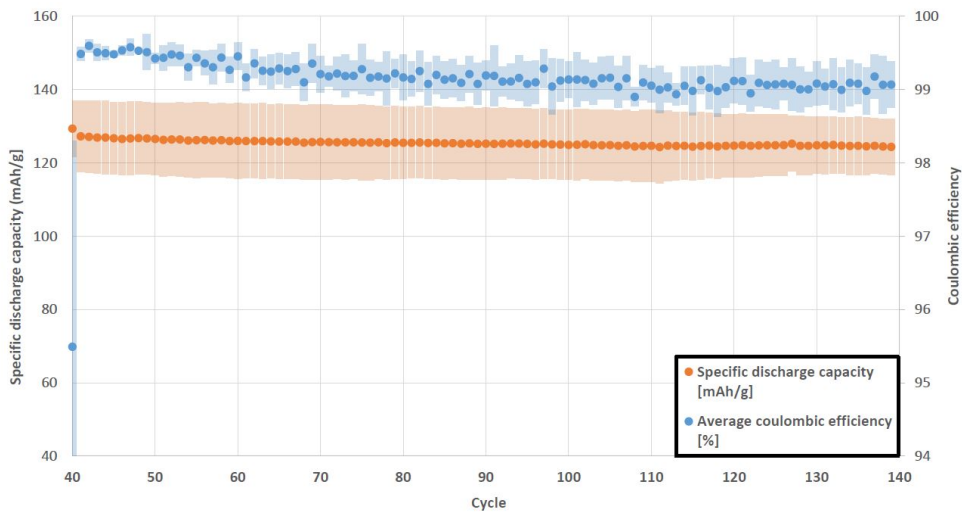approximately constant with infinitesimal reduction from 99.5% to 99.1%.

Figure 3.17: Average specific discharge capacity trend and CE of V1T100

Finally, in Figure 3.18, the capacity retention of each set of coin cells is shown as a histogram. Since the C-rate in long term cycling is equal to C/2 the capacity retention estimations can be started from rate test cycling with same C-rate which is cycle number 11. Hence, capacity fade is shown for 130 cycles in Figure 3.18 in form of histogram. As the histogram shows the highest capacity losses are for V1T100 and V1T50 with 4.6% and 7.8% respectively. On the other hand V05T50 has the minimum capacity fade after 130 cycles with 2.1% while V05T100 lost 3.5% of its capacity after 130 cycles with C-rate of C/2. The only group of half cells that are remained on the values greater than 140

mAh/g is V05T50 and the lowest final specific discharge capacity is for V1T100 with 124 mAh/g at the end of the test.
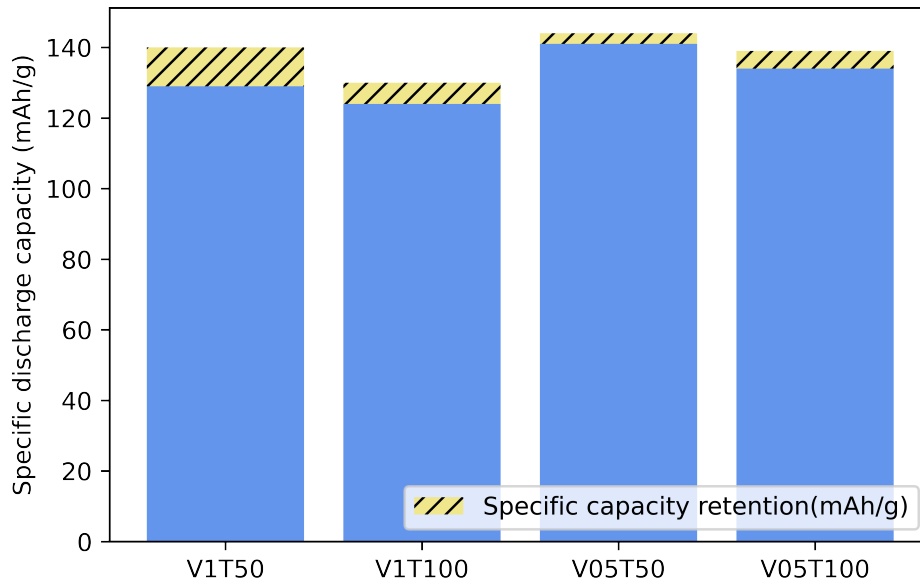
Figure 3.18: The blue bars display the specific discharge capacity of each group of experiments after 130 cycles and the yellow bars with diagonal stripes shows the capacity fade of each group during the cycling, capacity losses are 7.8%, 4.6%, 2.0% and 3.5% for V1T50, V1T100, V05T50 and V05T100 respectively.

4 | Discussion

This section addresses the electrochemical performance of coin cells and discuss its relation to cracks results. The most efficient way of drying will be proposed and discussed based on the energy consumption in drying process and quality of electrode. The quality of electrode will be discussed considering the results of characterization sections including cracks analysis and electrochemical performance.

4.1. Cracks and Drying Rate Discussion

The impact of crack results could be considered as the main factor to estimate the cathode quality and cell's electrochemical performance. In Figure 4.1, the proportion of crack's area over total area of electrode of large cracks are compared to each other for each group of investigated drying conditions.
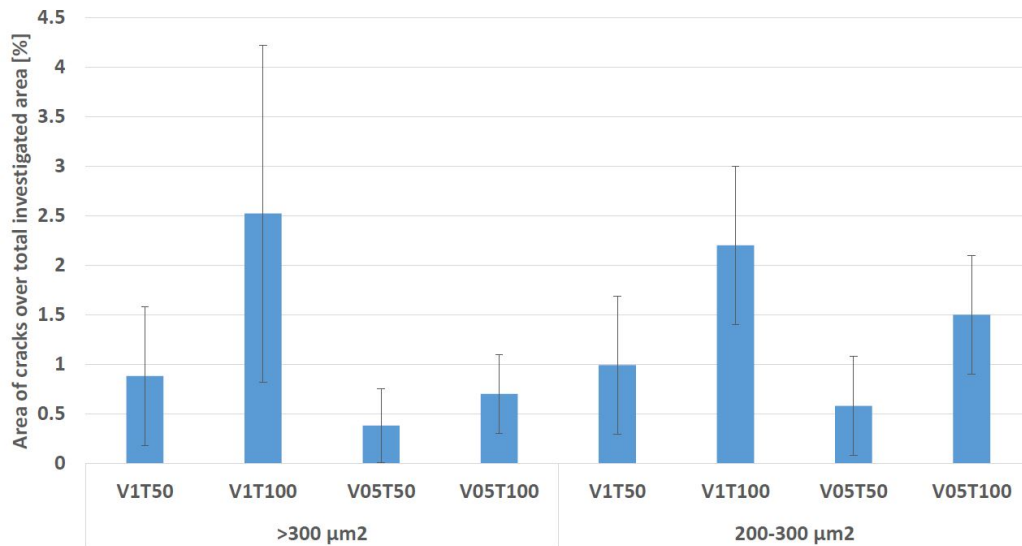
Figure 4.1: Comparison of proportion of crack's area over total area of electrode larger than 200μm with standard deviations for each group of drying conditions

According to Trunec et al [81], in the constant drying period, the NMP is continuously transported to the surface of the cathode by capillary force and evaporates with constant

rate. The particles come into contact with each other as the NMP solvent is gradually removed, and the body stiffens. When the NMP between the particles removed, the shrinkage of the electrode stops in $X_{critical}$ and the falling drying rate period starts. The rate of drying slows down gradually in this period, and the larger pores are emptied first. That is because of smaller pores with higher capillary tension may suck NMP from bigger pores, they stay fully saturated by solvent, resulting in an uneven drying front. Since the smaller ($X_{critical}$) represents the longer constant drying rate period and shorter falling drying rate period. According to the table 3.1 which displays the drying rates and the critical moisture contents, the experiment code of V05T50 has considerably lower $X_{critical}$ which is equal to 0.34, while the other codes are equal to 0.38 for V1T50 and 0.41 for V1T100 and V05T100.

Therefore, the results which is shown in the chapter three admits that the higher drying rate and $X_{critical}$ can increase the cracks over the electrode which is undesirable and since the falling drying rate period is shorter in V05T50 with temperature of 50C and 0.5 m/s of air velocity, the proportion of cracks area over total investigated area in considerably smaller than other groups with higher drying rate and $X_{critical}$.

4.1.1.   Experimental Drying Rate and Theoretical Drying Rate Comparison

As in the theory chapter illustrated, drying rate is proportional mass transfer coefficient through heat transfer coefficient. On the other hand, thanks to the Lewis analogy, mass transfer coefficient is connected to heat transfer coefficient. Hence, considering the measured data including average temperature and average air velocity, it is plausible to estimate the required values such as Pr, ρ_a, μ_{air}. Therefore, for the purpose of drying results validation, it is possible to compare the experimental and theoretical drying rate ratios of drying thermal conditions with the same temperatures and different velocities. Hence, as mentioned in theory part, the mass transfer coefficient can be calculated by equation 1.6 for thermal conditions of each group of experiments. On the other hand, the experimental drying rates in constant drying rate period are given in table 3.1 in the Results chapter and can be utilized for the ratio estimations.

Table 4.1: Experimental drying rate and theoretical drying rate comparison based on constant temperature and various velocity

Experiment Code	V1T50	V05T50	V1T100	V05T100
Air Velocity (m/s)	1	0.5	1	0.5
Drying Temperature °C	50	50	100	100
Constant Drying Rate (g/m^2.s)	0.0095	0.0057	0.042	0.0196
K_t (W/m^2.K)	30.96	17.78	30.71	17.64
K_m (m/s)	18.28	10.50	10.09	5.79
K_{mV05}/K_{mV1} (Theoretical ratio)	0.57		0.57	
W_{dV05}/W_{dV1} (Experimental ratio)	0.6		0.47	
Error (%)	4.46		18.7	

According to the table 4.1 the experimental drying rate and theoretical drying rate comparison based on constant temperature and various velocity are approximately equal with acceptable error. Since the convection coefficient is connected to Nusselt number and the error of Nusselt correlations are sometimes as large as 25% [30] the error between the experimental and theoretical ratios could be considered as acceptable and consequently the measured drying rates in the constant drying rate period are reliable.

4.2. Electrochemical Performance Discussion

As the rate test cycling suggests in chapter three, the electrochemical performance in higher C-rates is meaningfully dissimilar for the different groups of study. However, the experiment code of V05T50 performed better at C-rates of 3C and 5C, in comparison with the other groups. Similarly, as Figure 3.11 shows, V1T50 performed considerably better than V1T100 specially at C-rates of 3C and 5C where the specific discharge capacity of V1T100. For the latter, the capacity dropped to almost zero at the same C-rates. Correspondingly, V1T100 which has more large cracks as shown in Figure 4.1 shows undesirable performance specifically in rate test cycling, while V05T50 with less large cracks performed as the best group of study in the rate test, and showed least capacity fade over 130 cycles in the long term cycling.

According to other studies [29, 45], consistently low drying rates result in favorable homogeneous binder profiles, whereas consistently high drying rates are unfavorable, resulting in binder buildup at the evaporation surface and binder depletion near the current collector. Binder migration during the drying process, as well as lack of binder coverage

in some areas of the electrode, can cause capacity decline and mechanical failure[29] like for sample III in V1T100. Moreover, the pre-existing cracks caused by high drying rate, generate stress concentration at the crack points, which accelerates particle breakage. Consequently, electrical contact between active particles, conductive additives, and the current collector is disrupted, resulting in a loss of electronic/ionic conductivity and, eventually, capacity decline which happened during the long term cycling[28]. On the other hand, the electrode's adhesion was observed to be diminished when the binder migrated away from the area of the electrode towards the current collector[44, 46]. Hence, the inhomogeneous binder distribution in electrode and accumulation of binder in interface of electrode/separator surface increases high ionic resistance which lead to undesirable phenomena of ion diffusion reduction[66].

For comprehensive understanding, Figure C.3 in appendix C shows one of the electrode's thickness of experiment group of V1T100 which is dried by high drying rate, the detached area between current collector and cathode material is considerable.

Therefore, based on the galvanostatic cycling results, which is shown in Figure 3.18, the V05T50 showed the highest specific discharge capacity for the first cycle at C/2 (11th cycle) with 144 mAh/g and lowest capacity loss after 130 cycles with 2.0%. Conversely, the Figure 4.1 and Figure

4.3. Energy Consumption Discussion

In order to have comprehensive perspective for energy consumption for each group of drying experiment, the energy consumed for drying for average produced capacity ($\text{Wh}_{drying}/\text{Wh}_{capacity}$) with considering the capacity retention during the cycling will be discussed. As Figure 4.2 illustrates, the group cells of V1T50 with 74 $\text{Wh}_{drying}/\text{Wh}_{capacity}$ is the most energy consuming cells followed by V05T50 with 44.5 $\text{Wh}_{drying}/\text{Wh}_{capacity}$, in compare with Figure 3.1 the difference between V1T50 and V05T50 is lower since the produced capacity in V05T50 is meaningfully higher than V1T50. Moreover, as discussed before, the capacity retention of V1T50 is larger than V05T50 which affects on average discharge capacity of V1T50. On the other hand, the group of cells of V05T100 with 32 $\text{Wh}_{drying}/\text{Wh}_{capacity}$ is slightly lower than V1T100 with 38.8 $\text{Wh}_{drying}/\text{Wh}_{capacity}$,so V05T100 is the most energy-effective way of drying procedure among the other groups in this study. In addition, as the results admit, it is fair to state that the air velocity in experiments with low temperature is an essential factor for energy consumption in electrode drying procedure.

For the purpose of comparing the energy consumption per capacity ($\text{Wh}_{drying}/\text{Wh}_{capacity}$) with other studies, it should be considered that 40% of total energy for battery production

is consumed in drying process[99]. On the other hand, according to Kurland et al [54], the industrial energy consumption for battery production is 50 to 65 $Wh_{drying}/Wh_{capacity}$, so it is fair to estimate the energy consumption for industrial scale battery production as 20 to 26 $Wh_{drying}/Wh_{capacity}$ which is lower than given results in this study. It may due to the industrial productions can effort large scaled production which lead to lower consumption of energy in the processes like drying.
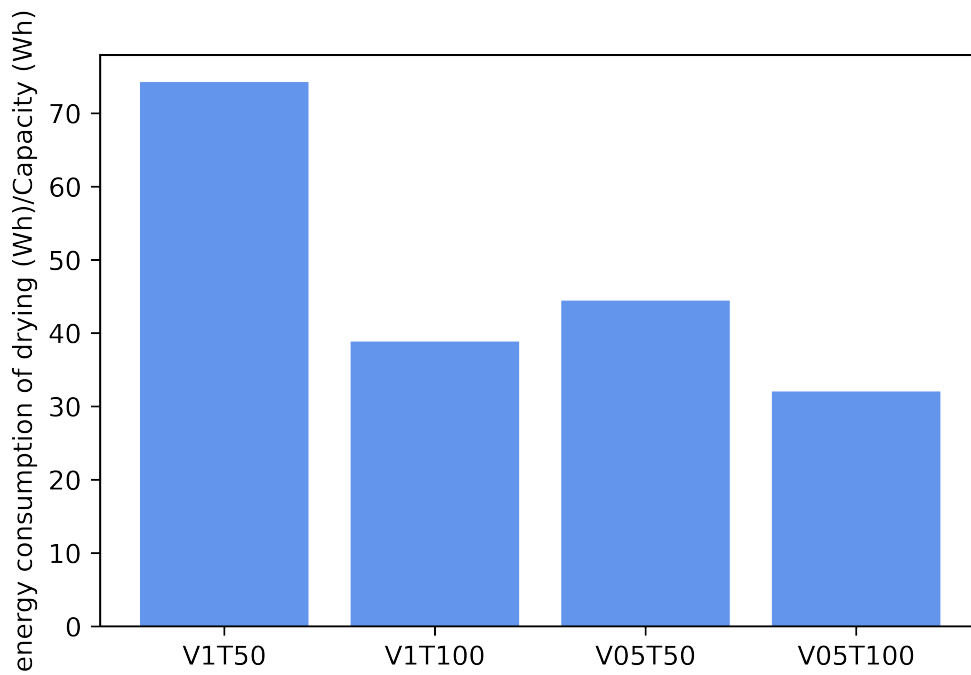
Figure 4.2: Energy consumption per produced capacity for each drying procedures $(Wh_{drying}/Wh_{capacity})$

5 | Conclusion

Drying processes have been committed with four different thermal conditions in order to study the impact of drying on the cracks formation and electrochemical performance of half-cells. Galvanostatic cycling was applied to characterize the electrochemical performance of half-cells by rate test cycling and long term cycling. Also, scanning electron microscopy (SEM) was used for cracks investigations.

Based on results and discussion parts, drying experiment with air velocity of 0.5 m/s and temperature of 100°C (V05T100) which has drying rate of 0.019 g/m^2.s and $X_{critical}$ of 0.41 is considered the most energy-effective approach of drying. This group of half-cells resulted relatively lower proportion of large cracks especially for cracks larger than $300\mu m^2$ which is equal to 0.69%. The 11th specific discharge capacity is 139 mAh/g and the capacity retention is equal to 3.5% after 130 cycles. The energy consumption per produced capacity is 32 $Wh_{drying}/Wh_{capacity}$ which is slightly lower than V1T100.

During the investigations it is experimentally concluded that the longer constant drying rate period leads to less cracks in the electrode. Hence, the $X_{critical}$ should be kept as small as possible which leads to longer period of constant drying rate. Moreover, from the studies [29, 42]and the results of experiments can be inferred that high drying rate leads to binder migration and lack of binder concentration in some parts of electrode especially between cathode material and current collector that may cause more cracks formation and poor electrochemical performance specially in high C-rates.

In addition, considering the results of energy consumption in drying procedure and the capacity of cells, it can be concluded that the impact of hot air velocity on specific energy consumption ($Wh_{drying}/Wh_{capacity}$) is considerable only at low temperatures, and as drying temperature increases the hot air velocity's impact on specific energy consumption diminishes because the drying time (D_t) reduced significantly.

6 | Future Work

Further investigations on drying and the electrochemical performance of half-cells can be taken place on various fields. First, according to Susarla et al. [76] a multi-zone drier can be used for electrode drying in order to consume less energy for drying procedure. Moreover, keeping the drying procedure in longer constant drying rate period with adjusting thermal conditions. In addition, higher drying rate could be investigated as future study by increasing the air velocity up to industrial scale (more than 20 m/s) and higher temperatures.

Second, for the electrochemical characterization, post-mortem analysis could be considered for after the galvanostatic cycling in order to study on the cracks formation during the cycling. Hence, the coin cells should be dissembled to take SEM pictures of the cathode to compare with the SEM pictures before cycling.

In addition, binder migration study of the electrode would be helpful for electrode quality assessment. This is possible with Energy-dispersive X-ray spectroscopy (EDS) to detect the fluorine element diffusion (which is representative of PVDF) along the thickness of electrode.

Bibliography

[1] Projected size of the global lithium-ion battery market from 2020 to 2026. `https://www.statista.com/statistics/1011187/projected-global-lithium-ion-battery-market-size/`. Accessed: 23-9-2021.

[2] Batteries are a key part of the energy transition. `https://www.weforum.org/agenda/2021/09/batteries-lithium-ion-energy-storage-circular-economy/`. Accessed: 10-9-2021.

[3] Steps in the battery manufacturing process. `https://rheonics.com/solutions-item/battery-production-slurry-mixing-and-coating/`. Accessed: 25-10-2021.

[4] *One-Way Analysis of Variance*, pages 399–402. Springer New York, New York, NY, 2008. ISBN 978-0-387-32833-1. doi: 10.1007/978-0-387-32833-1_297. URL `https://doi.org/10.1007/978-0-387-32833-1_297`.

[5] *Analysis of Variance*, pages 545–555. Springer New York, New York, NY, 2008. ISBN 978-0-387-32833-1. doi: 10.1007/978-0-387-32833-1_8. URL `https://doi.org/10.1007/978-0-387-32833-1_8`.

[6] *Fisher Distribution*, pages 199–200. Springer New York, New York, NY, 2008. ISBN 978-0-387-32833-1. doi: 10.1007/978-0-387-32833-1_143. URL `https://doi.org/10.1007/978-0-387-32833-1_143`.

[7] *Two-way Analysis of Variance*, pages 544–550. Springer New York, New York, NY, 2008. ISBN 978-0-387-32833-1. doi: 10.1007/978-0-387-32833-1_408. URL `https://doi.org/10.1007/978-0-387-32833-1_408`.

[8] *Introduction*, chapter 1, pages 1–8. John Wiley Sons, Ltd, 2015. ISBN 9781118414798. doi: https://doi.org/10.1002/9781118414798.ch1. URL `https://onlinelibrary.wiley.com/doi/abs/10.1002/9781118414798.ch1`.

[9] M. Akhilash, P. Salini, B. John, and T. Mercy. A journey through layered cathode materials for lithium ion cells – from lithium cobalt oxide to lithium-rich transition metal oxides. *Journal of Alloys and Compounds*, 869:159239, 2021. ISSN 0925-8388. doi: https://doi.org/10.1016/j.jallcom.2021.159239. URL `https://www.sciencedirect.com/science/article/pii/S0925838821006472`.

[10] J. L. Z. C. F. P. Y. C. K. Amine1. High-performance anode materials for rechargeable lithium-ion batteries. *Springer*, pages 1–11, 22-1-2018.

[11] S. J. An, J. Li, C. Daniel, D. Mohanty, S. Nagpure, and D. L. Wood. The state of understanding of the lithium-ion-battery graphite solid electrolyte interphase (sei) and its relationship to formation cycling. *Carbon*, 105:52–76, 2016. ISSN 0008-6223. doi: https://doi.org/10.1016/j.carbon.2016.04.008. URL `https://www.sciencedirect.com/science/article/pii/S0008622316302676`.

[12] E. I. authors. Battery storage in the united states: An update on market trends. *U.S Energy and Information Administration*, 1(1):42, 2021.

[13] A. Barai, K. Uddin, M. Dubarry, L. Somerville, A. McGordon, P. Jennings, and I. Bloom. A comparison of methodologies for the non-invasive characterisation of commercial li-ion cells. *Progress in Energy and Combustion Science*, 72:1–31, 2019. ISSN 0360-1285. doi: https://doi.org/10.1016/j.pecs.2019.01.001. URL `https://www.sciencedirect.com/science/article/pii/S0360128518300996`.

[14] R. Bhadra, K. Muthukumarappan, K. Rosentrater, and S. Kannadhason. Drying kinetics of distillers wet grains (dwg) under varying condensed distillers solubles (cds) and temperature levels. *Cereal Chemistry*, 88:451–458, 09 2011. doi: 10.1094/CCHEM-02-11-0018.

[15] H. Bockholt, W. Haselrieder, and A. Kwade. Intensive powder mixing for dry dispersing of carbon black and its relevance for lithium-ion battery cathodes. *Powder Technology*, 297:266–274, 2016. ISSN 0032-5910. doi: https://doi.org/10.1016/j.powtec.2016.04.011. URL `https://www.sciencedirect.com/science/article/pii/S003259101630170X`.

[16] B. M. . G. G. Botte. *Recycling of graphite anodes for the next generation of lithium ion batteries.* Journal of Applied Electrochemistry, 2016.

[17] S. N. Bryntesen, A. H. Strømman, I. Tolstorebrov, P. R. Shearing, J. J. Lamb, and O. Stokke Burheim. Opportunities for the state-of-the-art production of lib electrodes—a review. *Energies*, 14(5), 2021. ISSN 1996-1073. doi: 10.3390/en14051406. URL `https://www.mdpi.com/1996-1073/14/5/1406`.

[18] H. Chen, M. Ling, L. Hencz, H. Y. Ling, G. Li, Z. Lin, G. Liu, and S. Zhang. Exploring chemical, mechanical, and electrical functionalities of binders for advanced energy-storage devices. *Chemical reviews*, 118(18):8936–8982, 2018.

[19] J. Chen, J. Liu, Y. Qi, T. Sun, and X. Li. Unveiling the roles of binder in the mechanical integrity of electrodes for lithium-ion batteries. *Journal of The Electrochemical Society*, 160(9):A1502–A1509, 2013. doi: 10.1149/2.088309jes. URL `https://doi.org/10.1149/2.088309jes`.

[20] T. Cheng, Z. Ma, R. Gu, R. Chen, Y. Lyu, A. Nie, and B. Guo. Cracks formation in lithium-rich cathode materials for lithium-ion batteries during the electrochemical process. *Energies*, 11:2712, 10 2018. doi: 10.3390/en11102712.

[21] R. Cherrington and J. Liang. Materials and deposition processes for multifunctionality. In V. Goodship, B. Middleton, and R. Cherrington, editors, *Design and Manufacture of Plastic Components for Multifunctionality*, pages 19–51. William Andrew Publishing, Oxford, 2016. ISBN 978-0-323-34061-8. doi: https://doi.org/10.1016/B978-0-323-34061-8.00002-8. URL `https://www.sciencedirect.com/science/article/pii/B9780323340618000028`.

[22] K. Y. Cho, Y. I. Kwon, J. R. Youn, and Y. S. Song. Evaluation of slurry characteristics for rechargeable lithium-ion batteries. *Materials Research Bulletin*, 48(8): 2922–2926, 2013. ISSN 0025-5408. doi: https://doi.org/10.1016/j.materresbull.2013.04.026. URL `https://www.sciencedirect.com/science/article/pii/S0025540813002717`.

[23] A. Cholewinski, P. Si, M. Uceda, M. Pope, and B. Zhao. Polymer binders: Characterization and development toward aqueous electrode fabrication for sustainability. *Polymers*, 13(4), 2021. ISSN 2073-4360. doi: 10.3390/polym13040631. URL `https://www.mdpi.com/2073-4360/13/4/631`.

[24] C. Didier, W. K. Pang, and V. K. Peterson. 7 the influence of electrode material crystal structure on battery performance. *Crystallography in Materials Science: From Structure-Property Relationships to Engineering*, page 217, 2021.

[25] P. M. Doran. Chapter 11 - unit operations. In P. M. Doran, editor, *Bioprocess Engineering Principles (Second Edition)*, pages 445–595. Academic Press, London, second edition edition, 2013. ISBN 978-0-12-220851-5. doi: https://doi.org/10.1016/B978-0-12-220851-5.00011-3. URL `https://www.sciencedirect.com/science/article/pii/B9780122208515000113`.

[26] N. R. D.R. Cox. *The Theory of the Design of Experiments.* morphologies on statistics and applied probability 86. Chapman and Hall/CRC, 2000. ISBN 9781584881957.

[27] J. Drofenik, M. Gaberscek, R. Dominko, F. W. Poulsen, M. Mogensen, S. Pejovnik, and J. Jamnik. Cellulose as a binding material in graphitic anodes for li ion batteries: a performance and degradation study. *Electrochimica Acta*, 48(7):883–889, 2003. ISSN 0013-4686. doi: https://doi.org/10.1016/S0013-4686(02)00784-3. URL https://www.sciencedirect.com/science/article/pii/S0013468602007843.

[28] J. S. Edge, S. O'Kane, R. Prosser, N. D. Kirkaldy, A. N. Patel, A. Hales, A. Ghosh, W. Ai, J. Chen, J. Yang, S. Li, M.-C. Pang, L. Bravo Diaz, A. Tomaszewska, M. W. Marzook, K. N. Radhakrishnan, H. Wang, Y. Patel, B. Wu, and G. J. Offer. Lithium ion battery degradation: what you need to know. *Phys. Chem. Chem. Phys.*, 23: 8200–8221, 2021. doi: 10.1039/D1CP00359C. URL http://dx.doi.org/10.1039/D1CP00359C.

[29] F. Font, B. Protas, G. Richardson, and J. Foster. Binder migration during drying of lithium-ion battery electrodes: Modelling and comparison to experiment. *Journal of Power Sources*, 393:177–185, 2018. ISSN 0378-7753. doi: https://doi.org/10.1016/j.jpowsour.2018.04.097. URL https://www.sciencedirect.com/science/article/pii/S0378775318304464.

[30] T. L. B. A. S. L. FRANK P. INCROPERA, DAVID P. DEWITT. *Fundamentals of Heat and Mass Transfer*, chapter 7. JOHN WILEY SONS, 2007.

[31] E. R. Girden. *ANOVA: Repeated measures.* Number 84. Sage, 1992.

[32] R. Gonçalves, P. Dias, L. Hilliou, P. Costa, M. M. Silva, C. M. Costa, S. Corona-Galván, and S. Lanceros-Méndez. Optimized printed cathode electrodes for high performance batteries. *Energy Technology*, 9(1):2000805, 2021. doi: https://doi.org/10.1002/ente.202000805. URL https://onlinelibrary.wiley.com/doi/abs/10.1002/ente.202000805.

[33] R. Gonçalves, S. Lanceros-Méndez, and C. Costa. Electrode fabrication process and its influence in lithium-ion battery performance: State of the art and future trends. *Electrochemistry Communications*, 135:107210, 2022. ISSN 1388-2481. doi: https://doi.org/10.1016/j.elecom.2022.107210. URL https://www.sciencedirect.com/science/article/pii/S1388248122000121.

[34] J. B. Goodenough and Y. Kim. Challenges for rechargeable li batteries. *Chemistry of Materials*, 22(3):587–603, 2010. doi: 10.1021/cm901452z. URL https://doi.org/10.1021/cm901452z.

[35] J. B. Goodenough and K.-S. Park. The li-ion rechargeable battery: A perspective. *Journal of the American Chemical Society*, 135(4):1167–1176, 2013. doi: 10.1021/ ja3091438. URL `https://doi.org/10.1021/ja3091438`. PMID: 23294028.

[36] P. Guan, L. Zhou, Z. Yu, Y. Sun, Y. Liu, F. Wu, Y. Jiang, and D. Chu. Recent progress of surface coating on cathode materials for high-performance lithium-ion batteries. *Journal of Energy Chemistry*, 43:220–235, 2020. ISSN 2095-4956. doi: https://doi.org/10.1016/j.jechem.2019.08.022. URL `https://www.sciencedirect.com/science/article/pii/S2095495619307909`.

[37] A. Guerfi, M. Kaneko, M. Petitclerc, M. Mori, and K. Zaghib. Lifepo4 water-soluble binder electrode for li-ion batteries. *Journal of Power Sources*, 163 (2):1047–1052, 2007. ISSN 0378-7753. doi: https://doi.org/10.1016/j.jpowsour. 2006.09.067. URL `https://www.sciencedirect.com/science/article/pii/S0378775306019495`. Selected Papers presented at the FUEL PROCESSING FOR HYDROGEN PRODUCTION SYMPOSIUM at the 230th American Chemical SocietyNational Meeting Washington, DC, USA, 28 August – 1 September 2005.

[38] W. Haselrieder, B. Westphal, H. Bockholt, A. Diener, S. Höft, and A. Kwade. Measuring the coating adhesion strength of electrodes for lithium-ion batteries. *International Journal of Adhesion and Adhesives*, 60:1–8, 2015. ISSN 0143-7496. doi: https://doi.org/10.1016/j.ijadhadh.2015.03.002. URL `https://www.sciencedirect.com/science/article/pii/S0143749615000342`.

[39] K. . L. J. Henriksen, G. L.; Amine. Materials cost evaluation report for high-power li-ion batteries. *Language Acquisition*, 1(1):1–70, 2003.

[40] H. C. Hesse, M. Schimpe, D. Kucevic, and A. Jossen. Lithium-ion battery storage for the grid—a review of stationary battery storage system design tailored for applications in modern power grids. *Energies*, 10(12):2107, 2017.

[41] J. P. Holman. *Experimental Methods for Engineer*. McGrawHill, 2001. ISBN 978-0-07-352930-1.

[42] X. Hong, J. Jin, Z. Wen, S. Zhang, Q. Wang, C. Shen, and K. Rui. On the dispersion of lithium-sulfur battery cathode materials effected by electrostatic and stereo-chemical factors of binders. *Journal of Power Sources*, 324:455–461, 2016.

[43] Y. Hwa, P. D. Frischmann, B. A. Helms, and E. J. Cairns. Aqueous-processable redox-active supramolecular polymer binders for advanced lithium/sulfur cells. *Chemistry of Materials*, 30(3):685–691, 2018.

[44] S. Jaiser, M. Müller, M. Baunach, W. Bauer, P. Scharfer, and W. Schabel. Investigation of film solidification and binder migration during drying of li-ion battery anodes. *Journal of Power Sources*, 318:210–219, 2016.

[45] S. Jaiser, M. Müller, M. Baunach, W. Bauer, P. Scharfer, and W. Schabel. Investigation of film solidification and binder migration during drying of li-ion battery anodes. *Journal of Power Sources*, 318:210–219, 2016. ISSN 0378-7753. doi: https://doi.org/10.1016/j.jpowsour.2016.04.018. URL `https://www.sciencedirect.com/science/article/pii/S0378775316303561`.

[46] S. Jaiser, A. Friske, M. Baunach, P. Scharfer, and W. Schabel. Development of a three-stage drying profile based on characteristic drying stages for lithium-ion battery anodes. *Drying Technology*, 35(10):1266–1275, 2017.

[47] S. Jaiser, L. Funk, M. Baunach, P. Scharfer, and W. Schabel. Experimental investigation into battery electrode surfaces: The distribution of liquid at the surface and the emptying of pores during drying. *Journal of Colloid and Interface Science*, 494: 22–31, 2017. ISSN 0021-9797. doi: https://doi.org/10.1016/j.jcis.2017.01.063. URL `https://www.sciencedirect.com/science/article/pii/S002197971730070X`.

[48] J. Jeon, J.-K. Yoo, S. Yim, K. Jeon, G. H. Lee, J. H. Yun, D. K. Kim, and Y. S. Jung. Natural-wood-derived lignosulfonate ionomer as multifunctional binder for high-performance lithium–sulfur battery. *ACS Sustainable Chemistry & Engineering*, 7 (21):17580–17586, 2019.

[49] J. H. J.F. RICHARDSON and J.R. *chemical engineering,Particle Technology and Separation Processes*. A volume in Chemical Engineering Series. BACKHURST, 2003. ISBN 978-0-08-049064-9.

[50] Y. B. M. C. B. D. T. G. J. L. T. O. R. S. B. W. J. Y. J.-G. Z. . M. S. W. Jie Xiao, Qiuyan Li. Understanding and applying coulombic efficiency in lithium metal batteries. *Nature energy*, pages 1–10, 25 June 2020.

[51] J.-H. Kim, N. P. W. Pieczonka, and L. Yang. Challenges and approaches for high-voltage spinel lithium-ion batteries. *ChemPhysChem*, 15(10):1940–1954, 2014. doi: https://doi.org/10.1002/cphc.201400052. URL `https://chemistry-europe.onlinelibrary.wiley.com/doi/abs/10.1002/cphc.201400052`.

[52] R. Korthauer. *Lithium-Ion Batteries: Basics and Applications*. Springer, Berlin, Heidelberg, 2018.

[53] J. Kumberg, M. Müller, R. Diehm, S. Spiegel, C. Wachsmann, W. Bauer, P. Schar-

fer, and W. Schabel. Drying of lithium-ion battery anodes for use in high-energy cells: Influence of electrode thickness on drying time, adhesion, and crack formation. *Energy Technology*, 7(11):1900722, 2019. doi: https://doi.org/10.1002/ente. 201900722. URL `https://onlinelibrary.wiley.com/doi/abs/10.1002/ente. 201900722`.

[54] S. D. Kurland. Energy use for GWh-scale lithium-ion battery production. *Environmental Research Communications*, 2(1):012001, dec 2019. doi: 10.1088/2515-7620/ ab5e1e. URL `https://doi.org/10.1088/2515-7620/ab5e1e`.

[55] A. Kwade, W. Haselrieder, R. Leithoff, A. Modlinger, F. Dietrich, and K. Droeder. Current status and challenges for automotive battery production technologies. *Nature Energy*, 3:290, Apr. 2018. doi: 10.1038/s41560-018-0130-3.

[56] C.-C. Li and Y.-W. Wang. Binder distributions in water-based and organic-based LiCoO2 electrode sheets and their effects on cell performance. *Journal of The Electrochemical Society*, 158(12):A1361, 2011. doi: 10.1149/2.107112jes. URL `https://doi.org/10.1149/2.107112jes`.

[57] J. Li, C. Rulison, J. Kiggans, C. Daniel, and D. L. Wood. Superior performance of lifepo4 aqueous dispersions via corona treatment and surface energy optimization. *Journal of The Electrochemical Society*, 159(8):A1152, 2012.

[58] X. Li, J. Liu, M. N. Banis, A. Lushington, R. Li, M. Cai, and X. Sun. Atomic layer deposition of solid-state electrolyte coated cathode materials with superior high-voltage cycling behavior for lithium ion battery application. *Energy Environ. Sci.*, 7:768–778, 2014. doi: 10.1039/C3EE42704H. URL `http://dx.doi.org/10. 1039/C3EE42704H`.

[59] S. Lim, S. Kim, K. H. Ahn, and S. J. Lee. Stress development of li-ion battery anode slurries during the drying process. *Industrial & Engineering Chemistry Research*, 54(23):6146–6155, 2015.

[60] C. Liu, Z. G. Neale, and G. Cao. Understanding electrochemical potentials of cathode materials in rechargeable batteries. *Materials Today*, 19(2):109–123, 2016. ISSN 1369-7021. doi: https://doi.org/10.1016/j.mattod.2015.10.009. URL `https: //www.sciencedirect.com/science/article/pii/S1369702115003181`.

[61] S. Liu, X. Zeng, D. Liu, S. Wang, L. Zhang, R. Zhao, F. Kang, and B. Li. Understanding the conductive carbon additive on electrode/electrolyte interface formation in lithium-ion batteries via in situ scanning electrochemical microscopy. *Frontiers*

in Chemistry, 8, 2020. ISSN 2296-2646. doi: 10.3389/fchem.2020.00114. URL `https://www.frontiersin.org/article/10.3389/fchem.2020.00114`.

[62] H. Lu, A. Cornell, F. Alvarado, M. Behm, S. Leijonmarck, J. Li, P. Tomani, and G. Lindbergh. Lignin as a binder material for eco-friendly li-ion batteries. *Materials*, 9(3), 2016. ISSN 1996-1944. doi: 10.3390/ma9030127. URL `https://www.mdpi.com/1996-1944/9/3/127`.

[63] W. T. . A. K. Lu, J. State-of-the-art characterization techniques for advanced lithium-ion batteries. *nature energy*, 1(1), 2017.

[64] L. McKeen. *Fluorinated Coatings and Finishes Handbook.* Elsevier, 2015.

[65] N. Membreño, K. Park, J. B. Goodenough, and K. J. Stevenson. Electrode/electrolyte interface of composite -li3v2(po4)3 cathodes in a nonaqueous electrolyte for lithium ion batteries and the role of the carbon additive. *Chemistry of Materials*, 27(9):3332–3340, 2015. doi: 10.1021/acs.chemmater.5b00447. URL `https://doi.org/10.1021/acs.chemmater.5b00447`.

[66] R. Morasch, J. Landesfeind, B. Suthar, and H. A. Gasteiger. Detection of binder gradients using impedance spectroscopy and their influence on the tortuosity of li-ion battery graphite electrodes. *Journal of The Electrochemical Society*, 165(14): A3459–A3467, 2018. doi: 10.1149/2.1021814jes. URL `https://doi.org/10.1149/2.1021814jes`.

[67] A. C. Ngandjong, T. Lombardo, E. N. Primo, M. Chouchane, A. Shodiev, O. Arcelus, and A. A. Franco. Investigating electrode calendering and its impact on electrochemical performance by means of a new discrete element method model: Towards a digital twin of li-ion battery manufacturing. *Journal of Power Sources*, 485:229320, 2021. ISSN 0378-7753. doi: https://doi.org/10.1016/j.jpowsour.2020.229320. URL `https://www.sciencedirect.com/science/article/pii/S0378775320316086`.

[68] P. Peljo and H. H. Girault. Electrochemical potential window of battery electrolytes: the homo–lumo misconception. *Energy Environ. Sci.*, 11:2306–2309, 2018. doi: 10.1039/C8EE01286E. URL `http://dx.doi.org/10.1039/C8EE01286E`.

[69] a. F. F. Petros Selinis. Review—A Review on the Anode and Cathode Materials for Lithium-Ion Batteries with Improved Subzero Temperature Performance, journal =.

[70] S. Renganathan, N. Ahamed Khan, and R. Srinivasan. Drying of lithium-ion battery

negative electrode coating: Estimation of transport parameters. *Drying Technology*, pages 1–11, 2021.

[71] K. Rollag, D. Juarez-Robles, Z. Du, D. L. Wood III, and P. P. Mukherjee. Drying temperature and capillarity-driven crack formation in aqueous processing of li-ion battery electrodes. *ACS Applied Energy Materials*, 2(6):4464–4476, 2019.

[72] B. Rowden and N. Garcia-Araez. Estimating lithium-ion battery behavior from half-cell data. *Energy Reports*, 7:97–103, 2021. ISSN 2352-4847. doi: https://doi.org/10.1016/j.egyr.2021.02.048. URL `https://www.sciencedirect.com/science/article/pii/S2352484721001463`. 5th Annual CDT Conference in Energy Storage and Its Applications.

[73] P. Rozier and J. M. Tarascon. Review—li-rich layered oxide cathodes for next-generation li-ion batteries: Chances and challenges. *Journal of The Electrochemical Society*, 1(1):1–10, 2015.

[74] A. Smith, J. Burns, D. Xiong, and J. Dahn. Interpreting high precision coulometry results on li-ion cells. *Journal of The Electrochemical Society*, 158(10):A1136, 2011.

[75] A. J. Smith, J. C. Burns, S. Trussler, and J. R. Dahn. Precision measurements of the coulombic efficiency of lithium-ion batteries and of electrode materials for lithium-ion batteries. *Journal of The Electrochemical Society*, 157(2):A196, 2010. doi: 10.1149/1.3268129. URL `https://doi.org/10.1149/1.3268129`.

[76] N. Susarla, S. Ahmed, and D. W. Dees. Modeling and analysis of solvent removal during li-ion battery electrode drying. *Journal of Power Sources*, 378:660–670, 2018. ISSN 0378-7753. doi: https://doi.org/10.1016/j.jpowsour.2018.01.007. URL `https://www.sciencedirect.com/science/article/pii/S0378775318300077`.

[77] E. Talaie, P. Bonnick, X. Sun, Q. Pang, X. Liang, and L. F. Nazar. Methods and protocols for electrochemical energy storage materials research. *Chemistry of Materials*, 29(1):90–105, 2017.

[78] Y. S. R. M. I. S. Y. S. Z. J. Z. L. G. Tariq Bashir1, Sara Adeeba Ismail1. A review of the energy storage aspects of chemical elements for lithium-ion based batteries. *Energy materials*, pages 1–11, 19-10-2021.

[79] M. M. Thackeray, S.-H. Kang, C. S. Johnson, J. T. Vaughey, R. Benedek, and S. Hackney. Li 2 mno 3-stabilized limo 2 (m= mn, ni, co) electrodes for lithium-ion batteries. *Journal of Materials chemistry*, 17(30):3112–3125, 2007.

[80] A. Tornheim and D. C. O'Hanlon. What do Coulombic Efficiency and Capacity

Retention Truly Measure? A Deep Dive into Cyclable Lithium Inventory, Limitation Type, and Redox Side Reactions. *Journal of The Electrochemical Society*, 167 (11):110520, jul 2020. ISSN 1945-7111. doi: 10.1149/1945-7111/AB9EE8. URL `https://iopscience.iop.org/article/10.1149/1945-7111/ab9ee8https://iopscience.iop.org/article/10.1149/1945-7111/ab9ee8/meta`.

[81] M. Trunec and K. Maca. Chapter 7 - advanced ceramic processes. In J. Z. Shen and T. Kosmač, editors, *Advanced Ceramics for Dentistry*, pages 123–150. Butterworth-Heinemann, Oxford, 2014. ISBN 978-0-12-394619-5. doi: https://doi.org/10.1016/B978-0-12-394619-5.00007-9. URL `https://www.sciencedirect.com/science/article/pii/B9780123946195000079`.

[82] unknown. Chapter 3: Hypothesis testing. URL `https://courses.lumenlearning.com/suny-natural-resources-biometrics/chapter/chapter-3-hypothesis-testing/`.

[83] A. Väyrynen and J. Salminen. Lithium ion battery production. *The Journal of Chemical Thermodynamics*, 46:80–85, 2012. ISSN 0021-9614. doi: https://doi.org/10.1016/j.jct.2011.09.005. URL `https://www.sciencedirect.com/science/article/pii/S0021961411003090`. Thermodynamics of Sustainable Processes.

[84] J. wen LIU, X. hai LI, Z. xing WANG, H. jun GUO, W. jie PENG, Y. he ZHANG, and Q. yang HU. Preparation and characterization of lithium hexafluorophosphate for lithium-ion battery electrolyte. *Transactions of Nonferrous Metals Society of China*, 20(2):344–348, 2010. ISSN 1003-6326. doi: https://doi.org/10.1016/S1003-6326(09)60144-8. URL `https://www.sciencedirect.com/science/article/pii/S1003632609601448`.

[85] D. Wood, J. Quass, J. Li, S. Ahmed, D. Ventola, and C. Daniel. Technical and economic analysis of solvent-based lithium-ion electrode drying with water and nmp. *Drying Technology*, 36, 05 2017. doi: 10.1080/07373937.2017.1319855.

[86] D. L. Wood, J. Li, and C. Daniel. Prospects for reducing the processing cost of lithium ion batteries. *Journal of Power Sources*, 275:234–242, 2015. ISSN 0378-7753. doi: https://doi.org/10.1016/j.jpowsour.2014.11.019. URL `https://www.sciencedirect.com/science/article/pii/S037877531401845X`.

[87] K. N. Wood, M. Noked, and N. P. Dasgupta. Lithium metal anodes: Toward an improved understanding of coupled morphological, electrochemical, and mechanical behavior. *ACS Energy Letters*, 2(3):664–672, 2017. doi: 10.1021/acsenergylett.6b00650. URL `https://doi.org/10.1021/acsenergylett.6b00650`.

[88] Y. Xia, Y. Zhou, and M. Yoshio. Capacity fading on cycling of 4 v li / LiMn2o 4 cells. *Journal of The Electrochemical Society*, 144(8):2593–2600, aug 1997. doi: 10.1149/1.1837870. URL https://doi.org/10.1149/1.1837870.

[89] X. Xu, S. Lee, S. Jeong, Y. Kim, and J. Cho. Recent progress on nanostructured 4v cathode materials for li-ion batteries for mobile electronics. *Materials Today*, 16(12):487–495, 2013. ISSN 1369-7021. doi: https://doi.org/10.1016/j. mattod.2013.11.021. URL https://www.sciencedirect.com/science/article/ pii/S1369702113004227.

[90] D. P. F. C. T. S. R. D. J. S. W. K. B. O. T. M. M. H. G. H. E. K. D. J. L. B. . P. R. S. Xuekun Lu, Antonio Bertei. 3D microstructure design of lithium-ion battery electrodes assisted by X-ray nano-computed tomography and modelling. *Nature*, page 13, 2020. doi: https://doi.org/10.1038/s41467-020-15811-x.

[91] R. Yazami. Surface chemistry and lithium storage capability of the graphite–lithium electrode. *Electrochimica Acta*, 45(1):87–97, 1999. ISSN 0013-4686. doi: https:// doi.org/10.1016/S0013-4686(99)00195-4. URL https://www.sciencedirect.com/ science/article/pii/S0013468699001954.

[92] R. Younesi, A. S. Christiansen, R. Scipioni, D.-T. Ngo, S. B. Simonsen, K. Edström, J. Hjelm, and P. Norby. Analysis of the interphase on carbon black formed in high voltage batteries. *Journal of The Electrochemical Society*, 162(7):A1289–A1296, 2015. doi: 10.1149/2.0761507jes. URL https://doi.org/10.1149/2.0761507jes.

[93] L. H. . Z. J. Yuan, X. *Lithium-Ion Batteries: Advanced Materials and Technologies*. CRC Press., 2011.

[94] G. Zhang, B. Qiu, Y. Xia, X. Wang, Q. Gu, Y. Jiang, Z. He, and Z. Liu. Double-helix-superstructure aqueous binder to boost excellent electrochemical performance in li-rich layered oxide cathode. *Journal of Power Sources*, 420:29–37, 2019. ISSN 0378-7753. doi: https://doi.org/10.1016/j.jpowsour.2019.02.086. URL https:// www.sciencedirect.com/science/article/pii/S0378775319302113.

[95] S. Zhang, K. Xu, and T. Jow. Evaluation on a water-based binder for the graphite anode of li-ion batteries. *Journal of Power Sources*, 138(1):226–231, 2004. ISSN 0378-7753. doi: https://doi.org/10.1016/j.jpowsour.2004.05.056. URL https:// www.sciencedirect.com/science/article/pii/S0378775304006615.

[96] Y. S. Zhang, A. N. Pallipurath Radhakrishnan, J. B. Robinson, R. E. Owen, T. G. Tranter, E. Kendrick, P. R. Shearing, and D. J. L. Brett. In situ ultrasound acoustic measurement of the lithium-ion battery electrode drying process. *ACS Applied*

Materials & Interfaces, 13(30):36605–36620, 2021. doi: 10.1021/acsami.1c10472. URL `https://doi.org/10.1021/acsami.1c10472`. PMID: 34293855.

[97] Y. S. Zhang, N. E. Courtier, Z. Zhang, K. Liu, J. J. Bailey, A. M. Boyce, G. Richardson, P. R. Shearing, E. Kendrick, and D. J. L. Brett. A review of lithium-ion battery electrode drying: Mechanisms and metrology. *Advanced Energy Materials*, 12(2):2102233, 2022. doi: https://doi.org/10.1002/aenm.202102233. URL `https://onlinelibrary.wiley.com/doi/abs/10.1002/aenm.202102233`.

[98] H. Zheng, L. Tan, G. Liu, X. Song, and V. S. Battaglia. Calendering effects on the physical and electrochemical properties of li[ni1/3mn1/3co1/3]o2 cathode. *Journal of Power Sources*, 208:52–57, 2012. ISSN 0378-7753. doi: https://doi.org/10.1016/j.jpowsour.2012.02.001. URL `https://www.sciencedirect.com/science/article/pii/S0378775312003023`.

[99] K. Zhou, Y. Su, W. Liu, and Y. Deng. Parametric energy consumption modeling for cathode coating manufacturing of lithium-ion batteries. *IOP Conference Series: Materials Science and Engineering*, 793:012057, 04 2020. doi: 10.1088/1757-899X/793/1/012057.

[100] Z. Zhu, Y. He, H. Hu, and F. Zhang. Evolution of internal stress in heterogeneous electrode composite during the drying process. *Energies*, 14(6), 2021. ISSN 1996-1073. doi: 10.3390/en14061683. URL `https://www.mdpi.com/1996-1073/14/6/1683`.
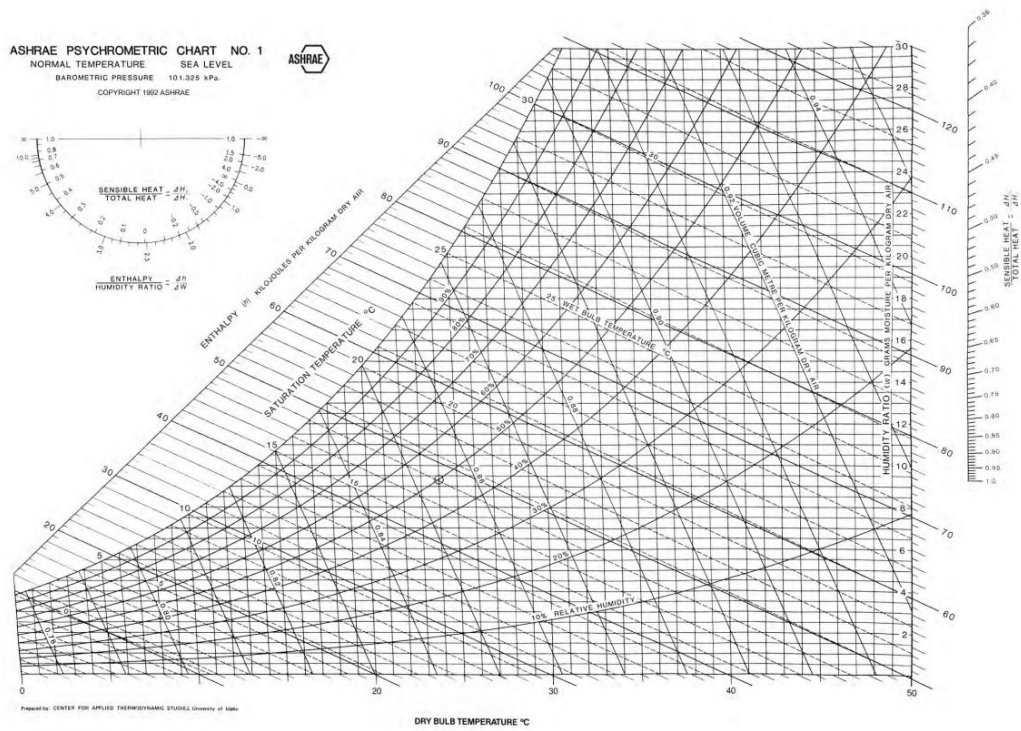
A | Appendix A

Figure A.1: Psychrometric chart for air Source: ASHRAE

B | Appendix B

Table B.1: Detailed list of materials used and their suppliers used for the cathode production.

Chemical Name and Abbreviation	Supplier	Product code
NMC111	Targray	SNMC03001
	$LiNi_{1/3}Mn_{1/3}Co_{1/3}O_2$	
PVDF	Sigma-Aldrich	1002912638
	Poly(vinylidene flouride)	
	average Mw 540,000 by GPC, powder	
Lignin	Sigma-Aldrich	1003004015
	Alkali - low sulfonate content	
Carbon Black (Super C45) TIMCAL C-NERGY^{TM}	Imerys Graphite and Carbon	
NMP	Sigma-Aldrich	102135677
	N-Methyl-2-pyrrolidone	
1 M LiPF$_6$ in EC/DMC/DEC (1/1/1)	Sigma-Aldrich	1002988447

C | Appendix C
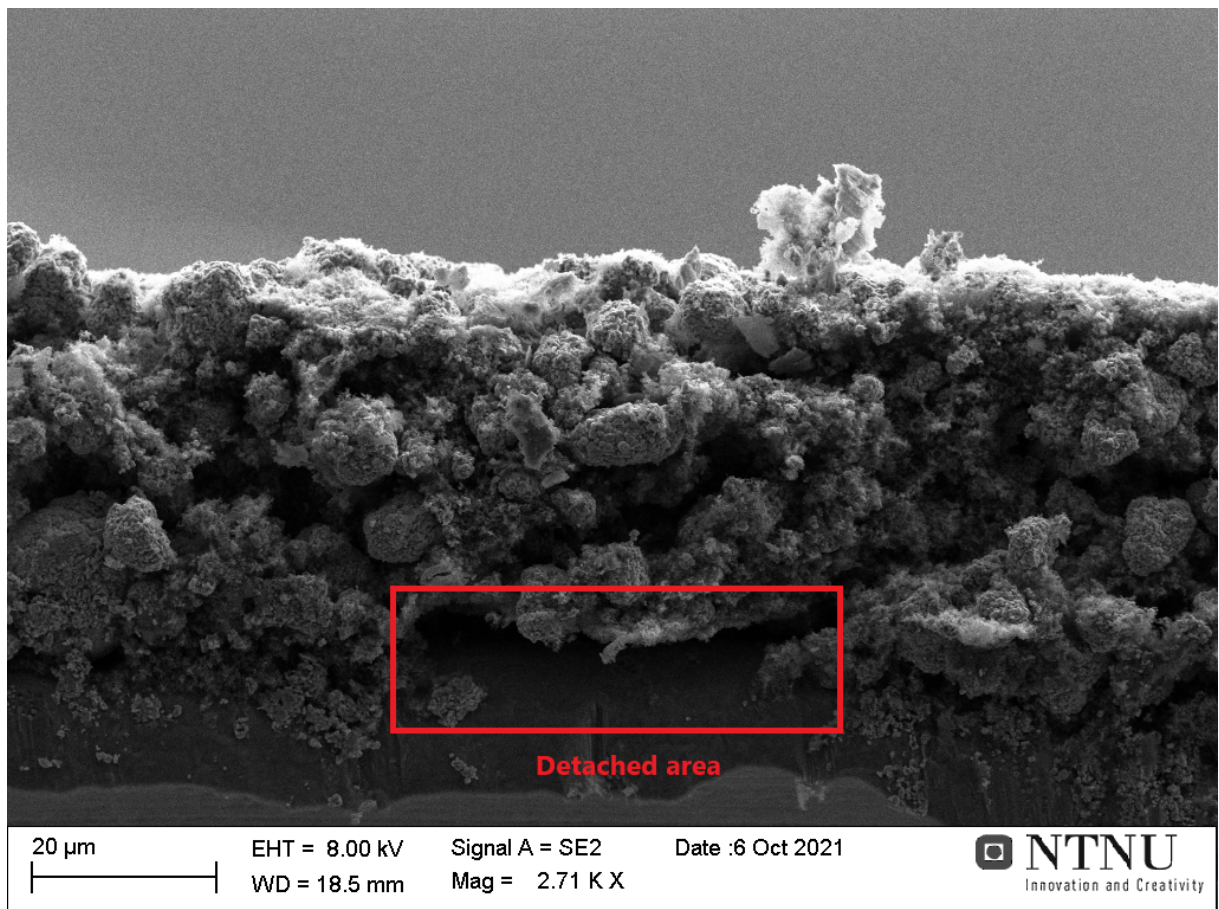
Figure C.1: Electrode's thickness of experiment group of V1T100 including detached area between cathode and current collector
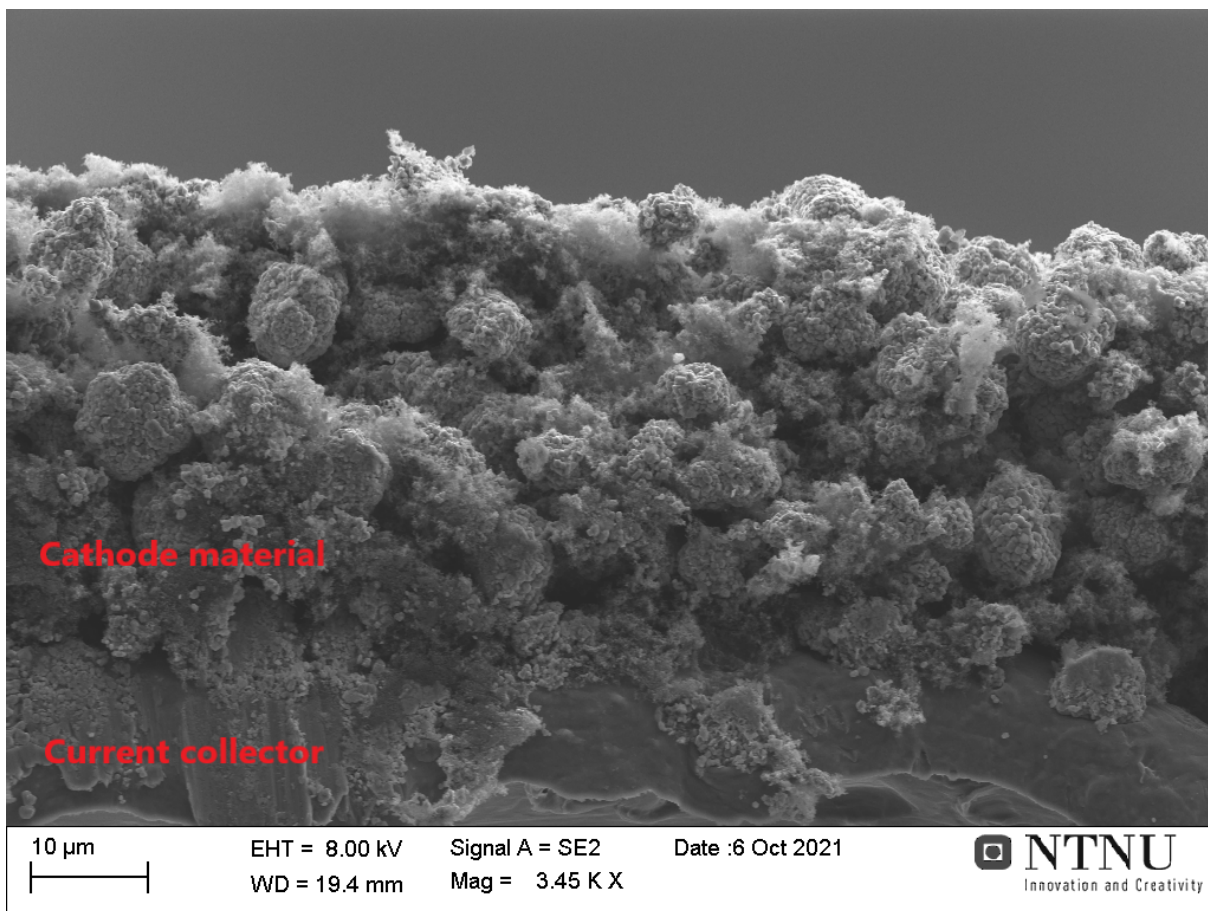
Figure C.2: Electrode's thickness of experiment group of V05T50 which is continuously attached to the current collector
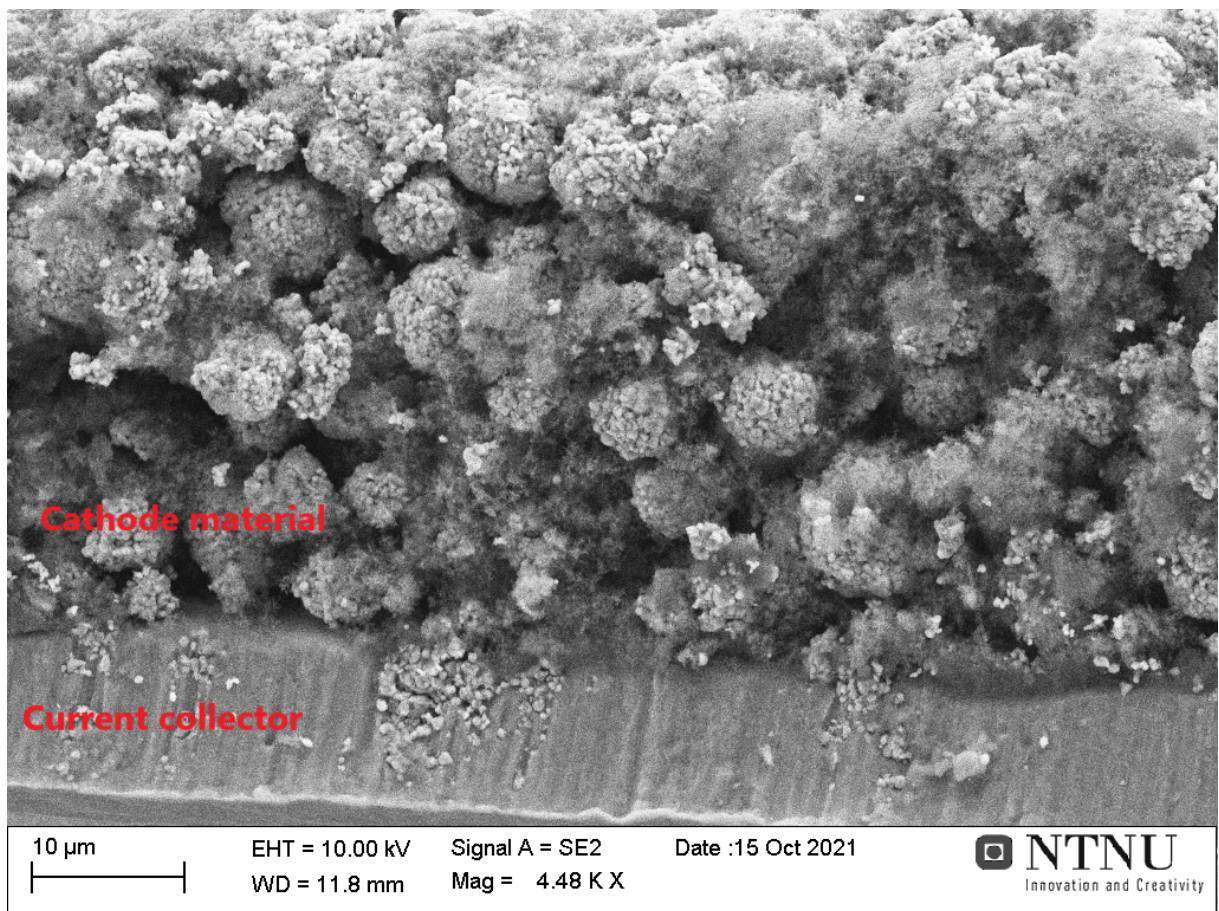
Figure C.3: Another electrode's thickness of experiment group of V05T50 which is continuously attached to the current collector

D | Appendix D

The sample with code of 13SV1T50 had more large cracks than other samples in the group of V1T50, as mentioned before, it may lead to poorer electrcochemical performance during long term cycling.
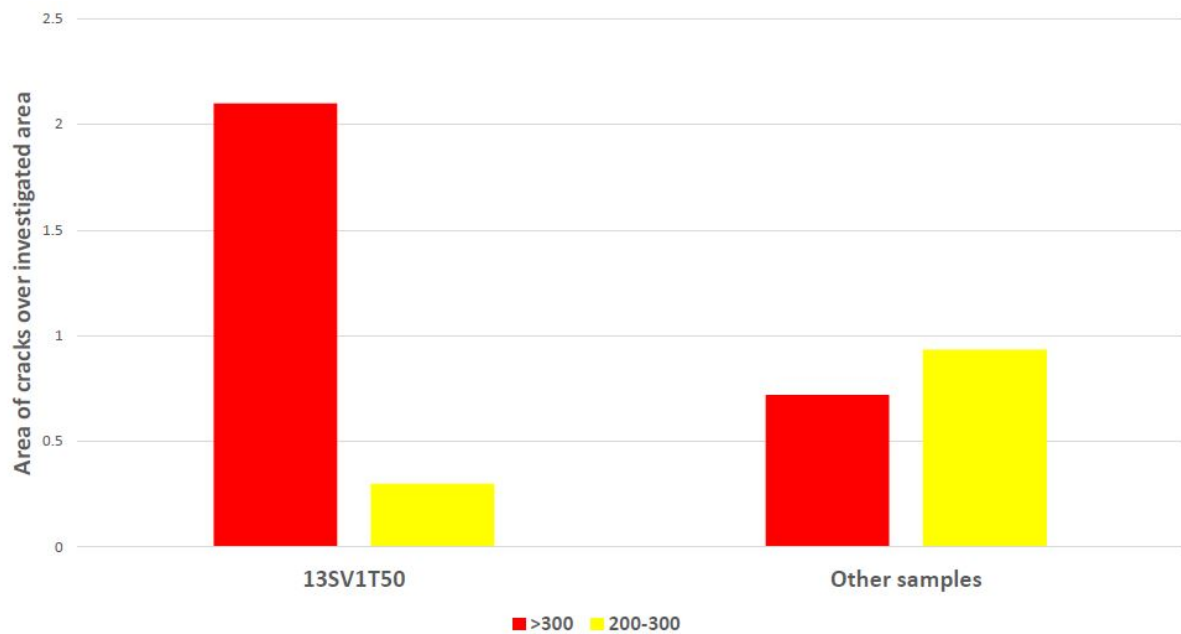
Figure D.1: Comparison of 13SV1T50 and other samples in area of cracks over investigated area of cathode

E | Appendix E

The average characteristic of cathodes that used in half-cells assembly.

	V05T50	V05T100	V1T50	V1T100
Average of thickness of electrode	53.7	59	51.7	57.8
Average of Weight of electrode(mg)	8.7	8.5	9.9	9.46
Average of Weight of active material(mg)	7.39	7.24	8.42	8.04

List of Figures

List of Tables

List of Symbols

Variable	Description	SI unit
$\dot{m}_s$	Rate of evaporation	Kg/s
K_t	Heat transfer coefficient	W/(m^2°C)
K_m	Mass transfer coefficient	m/s
Le	Lewis number	dimensionless
$C_{p,G}$	Specific heat capacity of gas	J/g.K
$C_{p,a}$	Specific heat capacity of air	J/g.K
L	Characteristic length	m
$\tilde{\rho}_G$	Molar density of the surrounding gas flow	Moles/m^3
Pr	Prandtl	m^2/s
V_a	Air velocity	m/s
μ_{air}	Air viscosity	Pa.s
λ_a	Thermal conductivity of air	W.m^{-1}K^{-1}
m_s	Mass of dry solid	kg
W_d	Drying rate	kg/s
A	Surface of area	m^2
X	Moisture content	kg$_{nmp}$/kg$_{bone\ dry\ material}$
t	Time	S
ρ_{air}	Density of air	kg/m^3
h	Enthalpy	kJ/kg
Z	Height	m
g	Gravitational acceleration	m/s^2
$\dot{Q}_{c.v.}$	Heat of control volume	kJ
$\dot{W}_{c.v.}$	Work of control volume	kJ
D_t	Drying time	S
P_{blower}	Power of blower	W
E_{blower}	Energy consumption of blower	Wh

Figure E.1: List of symbols with SI units and descriptions

Acknowledgements

First and foremost I am extremely grateful to my supervisors, Prof. Andrea Casalegno and Prof. Odne Stokke Burheim and co-supervisors, Dr. Silje Nornes Bryntesen and Dr. Ignat Tolstorebrovfor their valuable advice, continuous support, and patience during my Master's thesis. Their vast expertise and wealth of experience have supported me throughout my academic career and daily life. I would also like to thank Dr. Markus Solberg Wahl for his valuable technical support on my study. I would like to thank all the members in the Lib lab of department of Energy and Process Engineering in Norwegian University of Science and Technology. It is their kind help and support that have made my study and life in the Norway a wonderful time. Finally, I would like to express my gratitude to my wise and kindful parents, my brother, his wife and the incoming baby. It would have been difficult for me to finish my studies without their wonderful understanding and encouragement throughout the last few years.

F | Summary

POLITECNICO
MILANO 1863
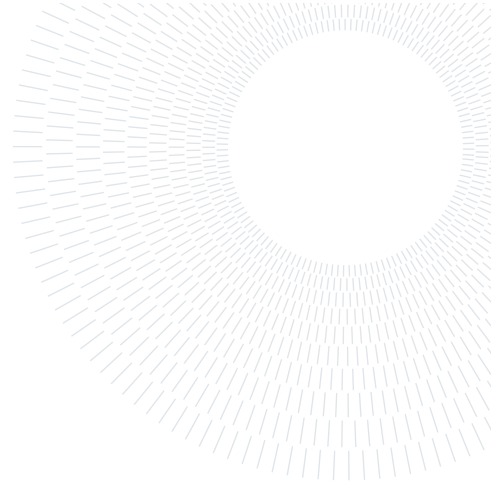
SCUOLA DI INGEGNERIA INDUSTRIALE
E DELL'INFORMAZIONE

Investigating Different Convective Drying Conditions and the Impact on Cracks and Electrochemical Performance

Author: ARMIN KAHROM

Advisor: PROF. ANDREA CASALEGNO, PROF. ODNE STOKKE BURHEIM

Co-advisor: PH.D. SILJE NORNES BRYNTESEN, DR. IGNAT TOLSTOREBROV

Academic year: 2022-23

1. Abstract

The characteristic that determines the microstructure of battery electrodes fundamentally changes during drying, making it a critical yet imperfectly understood processing step in cell manufacture. As a result, drying is an important step in electrode manufacturing since it can change component distribution inside the electrode. Phenomena such as binder migration, might have a detrimental impact on cell performance or cause mechanical failure.

Four different approaches of thermal conditions for drying procedure are introduced and investigated in three aspects including energy consumption of drying process, cracks formation, and electrochemical performance. The study admits that drying conditions have a considerable effect on cracks formation, which means the higher drying rate and critical moisture content lead to an irregular drying regime and a raise of crack formation.

In addition, based on the results of galvanostatic cycling, the specific discharge capacity and capacity retention after long-term cycling of half-cells with lower cracks show better electrochemical performance in comparison with samples with higher cracks density. The results of experiments admit that the cracks can increase the capacity fade of cells and decrease the initial capacities.

Finally, the study compares the different approaches of drying procedures to suggest the most energy-effective approach to drying in terms of energy consumption per produced capacity($\mathrm{Wh}_{drying}/\mathrm{Wh}_{capacity}$). It is found that the half-cells which were undergone extreme thermal conditions and higher drying rates, consumed significantly lower energy in comparison with other cells that were produced under lower drying rates. Hence, since the drying step considerably affects the total energy consumption of cell manufacturing, a reasonably high drying approach is recommended taking into account the electrode capacity to obtain an enhanced energy efficiency.

2. Experimental Work

The experimental section includes brief summary of slurry preparation, coating, convective drying, calendering, electrode preparation, coin cells assembly and characterization methods which were conducted during the thesis in

Executive summary Armin Kahrom

the Lithium-ion laboratory (LIB lab) at the Norwegian University of Science and Technology.

The slurry's powder formula was 85:10:5 for cathode material which means weight ratio (wt %) of 85% of NMC111, 10% of carbon black and 5% of PVDF as binder. N-Methyl-2-pyrrolidone (NMP) was selected as solvent and a wt% ratio of powder to solvent was 1:2. The mixture was placed in a centrifugal mixer (Thinky-Mixer ARE-250) for 25 minutes at 1500 rpm and 5 minutes at 2000 rpm.

A tape caster (MSK-AFA-HC100) was utilized to cast the slurry over the current collector (Aluminum foil) with a doctor blade thickness of 200 μm. After the casting process, the wet electrode was taken place in the convection dryer for drying. The temperature and air velocity of the convection dryer could be adjusted to achieve different drying rates, and were equipped with a weight-scale to measure the corresponding weight loss of NMP solvent during the evaporation. Four different approaches of thermal conditions were regulated by varying temperature and air velocity to achieve four different drying rates. Hence, four different groups of experiments were prepared, as shown in table1 with their corresponding experimental codes.

The dried electrode sheets were removed from the convection dryer crack investigations with a Scanning Electron Microscopy (SEM) and eventually coin cells assembly. These were cut into cathodes of 15 mm diameter, and post-dried at 120 C for 4 hours to remove NMP residues. The coin cells were assembled in a glovebox with a dry Ar atmosphere into CR2032 cells, using 40μL lithium (Li) hexauorophosphate (LiPF$_6$) electrolyte and Li metal as anode. To reveal the electrochemical performance of the cathode, and to have an effective comparison of the electrochemical performance between the studies, these half-cells were cycled in a galvanostatic battery cycler.

From the electrode surface crack characterization in SEM, five electrode sheets were prepared for each drying conditions, and studied at three places to have comprehensive and statistically comparable results. Three cathodes were assembled into half cells per drying condition, and tested at high cycling (charge/discharging) rates (rate-test) and at long-term cycling ($>$ 100 cycles) to study the cell's capacity retention and

degradation.

3. Summary of Results and Discussion

In this section, a brief explanation of the main results will be presented and discussed. The results includes the drying kinetics, electrode surface cracks analysis, electrochemical performance, and the convection oven's energy consumption during drying.

3.1. Drying Procedure

The constant drying rate (W$_D$) of each experiment is estimated by equation 4 and critical moisture content (X$_{critical}$) is defined as the beginning of the "falling drying rate"-step.

Table1 displays the results of drying process, where the constant drying rate varies with drying thermal conditions. The constant drying rate is at its maximum (0.042 g/m^2.s) for the V1T100 samples, meaning for electrodes dried under the highest temperature (T=100 C) and air-flow velocity (V=1 m/s). The minimum value for the constant drying rate is equal to 0.0057 g/m^2.s for those dried at under the most gentle conditions (V05T50). The X$_{critical}$ is proportional to the drying rate of the thermal conditions and the smallest value of X$_{critical}$ is equal to 0.34 for V05T50, which means that V05T50 obtained a longer constant drying period compared to the other thermal conditions. According to Trunec et al. [9], in the constant drying period, the NMP is continuously transported to the surface of the cathode by capillary forces and evaporate with a constant rate. The particles come into contact with each other as the NMP solvent is gradually removed, and the coating stiffens into a dry electrode. When the NMP between the particles are removed, shrinkage of the body stops and the X$_{critical}$ is reached. This marks and start of the falling drying rate period. The rate of drying slows down gradually at this period because the solvent is trapped in pores. The larger pores are emptied first because the smaller pores with higher capillary tension may suck NMP from bigger pores which then stay fully saturated by solvent, and is seen as an uneven drying front.

Table 1: The drying rate during constant rate period and critical moisture content of each drying conditions $X_{critical}$

Experiment Code	V1T50	V1T100	V05T50	V05T100
Air Velocity (m/s)	1	1	0.5	0.5
Drying Temperature °C	50	100	50	100
Constant Drying Rate (g/m^2.s)	0.0095	0.042	0.0057	0.0196
$X_{critical}$ (Kg$_{NMP}$/Kg$_{dry}$)	0.38	0.41	0.34	0.41
Standard deviation of Constant drying rates	0.00084	0.0018	0.0015	0.0029
Standard Deviation of $X_{critical}$	0.011	0.085	0.026	0.077

3.2. Drying Rate Validation

For the purpose of validation, the experimental results were compared with theoretical results obtained by Susarla et al. [8]. The heat transfer coefficient (K_t) and mass transfer coefficient (K_m) is connected together by Lewis analogy. These are connected trough the density and heat capacity of the gas and Lewis (Le) number according to equation 1. The n depends on the flow, and equals to 0.33 for laminar flow and 0.4 for turbulent flow.[8]

$$\frac{K_t}{K_m} = C_{p,G}.\tilde{\rho}_G.\text{Le}^{1-n} \qquad (1)$$

To compare between experimental and theoretical drying rates, the heat and mass transfer coefficients will be investigated to evaluate the measured data. For the turbulent flow of hot air over a flat slab, the equation 2 were used to calculate the heat transfer coefficient [8]:

$$K_t = 0.037 \cdot V_a^{0.8} \cdot \frac{\mu_a}{\rho_a} \cdot \text{Pr}^{1/3} \cdot \lambda_a \cdot L^{-0.2} \qquad (2)$$

The hot air velocity is shown by V_a, μ_a is the viscosity of air, and the Pr represent Prandtl number of air. The λ_a is the thermal conductivity of the air and L is the characteristic length of electrode. The mass transfer coefficient is then calculated from the heat transfer coefficient using the Chilton-Colburn correlation [8]:

$$K_m = \frac{K_t}{C_p \rho_a} \cdot Le^{-2/3} \qquad (3)$$

where Le is the Lewis number.
In order to figure out the critical moisture content ($X_{critical}$), constant drying rate and falling drying rate should be estimated by the measured data of experiments based on equation 4.

$$W_D = \frac{-m_s}{A_e} \cdot \frac{dX}{dt} \qquad (4)$$

where m_s is representative of mass of dry solid of electrode in (kg), W_d is for drying rate in $kg/m^2.s$ and X is for moisture content (kg of solvent/kg of dry electrode material), A_e is for electrode surface area in m^2 and t represents time in seconds[1, 7].
As illustrated, the drying rate is proportional to the mass transfer coefficient through the heat transfer coefficient. On the other hand, thanks to the Lewis analogy, mass transfer coefficient is connected to heat transfer coefficient. Hence, considering the measured data including the average temperature and average air velocity, it is possible to estimate the required values such as Pr, ρ_a and μ_{air}. Therefore, experimental drying rate ratio and theoretical mass transfer coefficient ratio of drying thermal conditions with the same temperatures and different velocities are compared based on the given equations and experimental results. Hence, the mass transfer coefficient was calculated by equation 3 for thermal conditions of each group of experiments. The experimental drying rates from the constant drying rate period are given in table 1 in the Results chapter and can be utilized for the ratio estimations (W_{dV05}/W_{dV1}).

Table 2: Experimental drying rate and theoretical drying rate comparison based on constant temperature and various velocity

Experiment Code	V1T50	V05T50	V1T100	V05T100
Air Velocity (m/s)	1	0.5	1	0.5
Drying Temperature °C	50	50	100	100
Constant Drying Rate (g/m^2.s)	0.0095	0.0057	0.042	0.0196
K_t (W/m^2.K)	30.96	17.78	30.71	17.64
K_m (m/s)	18.28	10.50	10.09	5.79
K_{mV05}/K_{mV1} (Theoretical ratio)	0.57		0.57	
W_{dV05}/W_{dV1} (Experimental ratio)	0.6		0.47	
Error (%)	4.46		18.7	

3.3. Characterization methods

For crack analysis investigations, five samples for each drying conditions were prepared and studied by SEM. Since the cracks with reasonable area should be considered, the cracks are sorted in range of 10 μm^2 to >300 μm^2 as in Figure 3.6 and 3.7 are shown (main report). In Figure 1, the summary of large cracks (larger than 200 μm^2) for each group of study is shown.

Table 3: Cycling program including Rate test cycling and long term cycling programs with different discharge C-rates and voltage in range of 3 to 4.3 V

Cycle			Discharging
	C-rate	CV	C-rate
1-5	C/10	-	C/10
6-10	C/5	4.3	C/5
11-15	C/2	4.3	C/2
16-20	C/2	4.3	C
21-25	C/2	4.3	2C
26-30	C/2	4.3	3C
31-35	C/2	4.3	5C
36-40	C/10	-	C/10
41-140	C/2	-	C/2

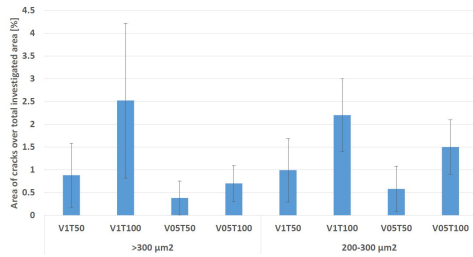
Figure 1: Comparison of proportion of crack's area over total area of electrode larger than $200 \mu m^2$ with standard deviations for each group of drying conditions

Considering the table 1 and Figure 1, it is fair to state that the higher drying rate and $X_{critical}$ can increase the cracks over the electrode which is undesirable and since the falling drying rate period is shorter in V05T50, the cracks formation is meaningfully lower in comparison with higher drying rates such as V1T100 with maximum drying rate and longer falling drying rate period (greater $X_{critical}$).

The half-cells were undergone two different programs for cycling, first one was rate test cycling to evaluate electrochemical performance of coin cells under different C-rates. Table 3 shows the summary of rate test cycling program with more details. The second program was long term cycling with the purpose of capacity retention evaluation and Coulombic efficiency (CE) of cells during long term usage, the cycling takes 100 cycles with C-rate of C/2 and constant voltage equal to 4.3 V.

In the following charts, the results of rate-test cycling for all groups of experiments are dis-

played and compared two by two. The Figure2 displays the rate test comparison of V05T50 and V05T100, as the chart presents, the electro-chemical performance of V05T50 which dried by lower drying rate is slightly better than V05T100 specially in high C-rates like 5C.
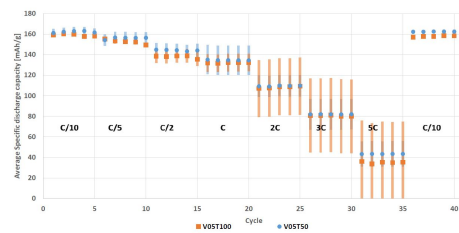

Figure 2: Specific discharge capacity of V05T100 and V05T50

Figure 3 displays the comparison of V1T50 and V1T100. It illustrates that V1T100 which was dried at the most extreme conditions performed significantly worse than V1T50 and those with lower air-flows (V05T50 and V05T100). Specifically, the specific discharge capacity of V1T100 fell to almost zero in C-rates of 3C and 5C. Moreover, the specific discharge capacity of V1T100 declined faster than V1T50 with an increasing C-rate. As indicated by others [3, 6], consistently low drying rates result in favorable homogeneous binder profiles, whereas consistently high drying rates results in binder build-up at the evaporation surface and binder depletion near the current collector. Binder migration during the drying process, as well as lack of binder coverage in some areas of the electrode, can cause capacity decline and mechanical failure[3]. Moreover, one possible explanation is the pre-existing cracks caused by high drying rate, generate stress concentration at the crack points, which accelerates particle breakage. Consequently, electrical contact between active particles, conductive additives, and the current collector is disrupted, resulting in a loss of electronic/ionic conductivity and, eventually, capacity decline which can be detected over long term cycling [2].
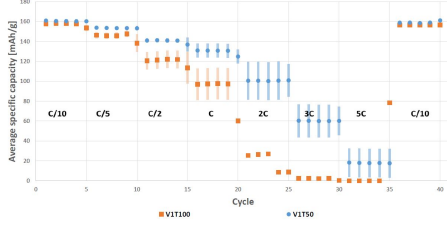
Figure 3: Specific discharge capacity of V1T100 and V1T50

The long term cycling results is shown in Figure 4. The V05T50 with least cracks showed the highest specific discharge capacity for the first cycle at C/2 (11th cycle) of 144 mAh/g and the lowest capacity loss after 130 cycles with 2.1%. As the Figure 1 and Figure 3 show, the V1T100 has the lowest specific discharge capacity at 11th cycle which is equal to 130 mAh/g and capacity fade of 4.6%. It also shows the highest percentage of large cracks over the total area of electrode. Surprisingly, while the electrochemical performance of V1T50 in the rate test cycling performed considerably better than V1T100, it suffered from the largest capacity fade at 7.8 % during long term cycling. This is because of the sample (ref. 13SV1T50), which showed a considerably larger formation of large cracks compared to other parallel samples in the group V1T50. This also lead to the relatively high standard deviation of V1T50 in Figure 1. Hence, it may be assumed that during the long term cycling, stress concentration at crack points leads to particle breakage and capacity fade.
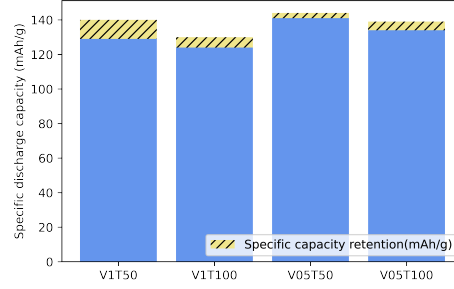

Figure 4: The blue bars display the specific discharge capacity of each group of experiments after 130 cycles and the yellow bars with diagonal stripes shows the capacity fade of each group during the cycling, capacity losses are 7.8%, 4.6%, 2.0% and 3.5% for V1T50, V1T100, V05T50 and V05T100 respectively.

With the intention of making a comprehensive perspective for energy consumption analysis of the drying procedure, the energy consumption of heating elements to adjust the temperature (equation 5) and energy consumption of blower to regulate the desired air-velocity of convection dryer were estimated .

The heater duty for the input air heat exchanger for a continuous convective air drier (Q) is provided by [4]:

$$Q = A \cdot V_\alpha \cdot \rho_\alpha \cdot c_\alpha \cdot \Delta T \cdot D_t \qquad (5)$$

The equation of energy conservation can be simplified to calculate the specific work ($\dot{W}$) needed for the air blower as below:

$$\dot{W} = h_i - (\frac{1}{2} \cdot \dot{V}_{\alpha,e}^2 + h_e) \qquad (6)$$

Equation 6 can be used to calculate the specific work of blower based on kJ/kg of air. However, in order to calculate the power of blower (P_{blower}) we have:

$$P_{blower} = \dot{W} \cdot \dot{m}_{air} \qquad (7)$$

The estimated power of blower (P_{blower}) should be multiply by drying time (D_t) which results energy consumption (E_b) of the blower during the drying procedure:

$$E_b = P_{blower} \cdot D_t \qquad (8)$$

Executive summary   **Armin Kahrom**

In next step, the energy consumption used during drying to produce one gram of electrode (i.e. the specific energy consumption) was estimated, and used to compare the energy efficiency of each drying condition as shown in Figure 5. Considering the drying experiments at 50 °C, the specific energy consumption varied considerably by decreasing the air velocity. Meanwhile, the energy consumption difference in the drying approaches with 100 °C is negligible. This is because the drying time at 50 °C are significantly longer than at 100 °C, so the energy consumption for both the blower and heating elements become main factor of energy consumption at.
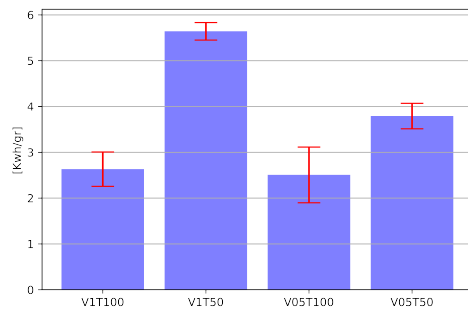

Figure 5: Energy consumption per produced gram of electrode for each drying approaches

Finally, considering the average discharge capacities of each groups of experiment and total energy consumption of drying process, the final value of drying energy consumption over specific discharge capacity can be calculated ($Wh_{drying}/Wh_{capacity}$) and compared. Figure 6 shows the final results of energy consumption evaluation with a histogram. Based on the histogram V05T100 is the most energy-effective approach of drying in this study. Considering Figure 5 and Figure 6, while V1T100 specific energy consumption per gram of electrode is the lowest, thermal conditions of 100 °C for temperature and 1 m/s for air velocity should be considered as most energy-effective approach for drying in this study, because the specific capacity (mAh/g) of V05T100 is higher than specific capacity of V1T100.
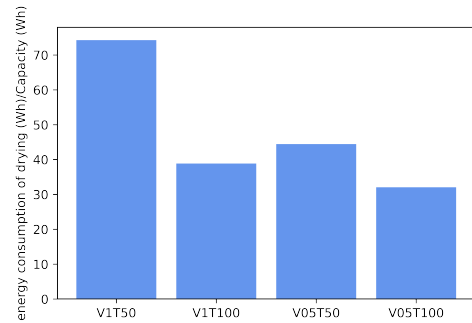

Figure 6: Energy consumption during drying per produced battery capacity ($Wh_{drying}/Wh_{capacity}$) is represented for each drying condition.

4.   Conclusion

Drying processes have been committed with four different thermal conditions in order to study the impact of drying on the cracks formation and electrochemical performance of half-cells. Galvanostatic cycling was applied for characterize the electrochemical performance of half-cells by rate test cycling and long term cycling programs. Also, Scanning electron microscopy (SEM) method was used for cracks investigations.

The drying experiment with air velocity of 0.5 m/s and temperature of 100°C (V05T100) which has drying rate of 0.019 g/m^2.s and $X_{critical}$ of 0.41 is considered the most energy-effective approach of drying. This group of half-cells resulted relatively lower proportion of large cracks especially for cracks larger than $300\mu m^2$ which is equal to 0.69%. The initial specific discharge capacity is 139 mAh/g and the capacity retention is equal to 3.5% after 130 cycles. The energy consumption per produced capacity is 32 $Wh_{drying}/Wh_{capacity}$ which is slightly lower than V1T100.

During the investigations it is experimentally concluded that the longer constant drying rate period leads to less cracks in the electrode. Hence, the $X_{critical}$ should be kept as small as possible which leads to longer period of constant drying rate. Moreover, from the studies [3, 5]and the results of experiments can be inferred that high drying rate leads to binder migration and lack of binder concentration in some parts of

electrode especially between cathode material and current collector that may cause more cracks formation and poor electrochemical performance specially in high C-rates.

In addition, considering the results of energy consumption in drying procedure and the capacity of cells, it can be concluded that the impact of hot air velocity on specific energy consumption ($\mathrm{Wh}_{drying}/\mathrm{Wh}_{capacity}$) is considerable only at low temperatures, and as drying temperature increases the hot air velocity's impact on specific energy consumption diminishes because the drying time (D_t) reduced significantly.

References

[1] Rumela Bhadra, Kasi Muthukumarappan, Kurt Rosentrater, and Sankarandh Kannadhason. Drying kinetics of distillers wet grains (dwg) under varying condensed distillers solubles (cds) and temperature levels. *Cereal Chemistry*, 88:451–458, 09 2011.

[2] Jacqueline S. Edge, Simon O'Kane, Ryan Prosser, Niall D. Kirkaldy, Anisha N. Patel, Alastair Hales, Abir Ghosh, Weilong Ai, Jingyi Chen, Jiang Yang, Shen Li, Mei-Chin Pang, Laura Bravo Diaz, Anna Tomaszewska, M. Waseem Marzook, Karthik N. Radhakrishnan, Huizhi Wang, Yatish Patel, Billy Wu, and Gregory J. Offer. Lithium ion battery degradation: what you need to know. *Phys. Chem. Chem. Phys.*, 23:8200–8221, 2021.

[3] F. Font, B. Protas, G. Richardson, and J.M. Foster. Binder migration during drying of lithium-ion battery electrodes: Modelling and comparison to experiment. *Journal of Power Sources*, 393:177–185, 2018.

[4] J. P. Holman. *Experimental Methods for Engineer*. McGrawHill, 2001.

[5] Xiaoheng Hong, Jun Jin, Zhaoyin Wen, Sanpei Zhang, Qingsong Wang, Chen Shen, and Kun Rui. On the dispersion of lithium-sulfur battery cathode materials effected by electrostatic and stereo-chemical factors of binders. *Journal of Power Sources*, 324:455–461, 2016.

[6] Stefan Jaiser, Marcus Müller, Michael Baunach, Werner Bauer, Philip Scharfer, and Wilhelm Schabel. Investigation of film solidification and binder migration during drying of li-ion battery anodes. *Journal of Power Sources*, 318:210–219, 2016.

[7] J.H. HARKER J.F. RICHARDSON and J.R. *chemical engineering,Particle Technology and Separation Processes*. A volume in Chemical Engineering Series. BACKHURST, 2003.

[8] Naresh Susarla, Shabbir Ahmed, and Dennis W. Dees. Modeling and analysis of solvent removal during li-ion battery electrode drying. *Journal of Power Sources*, 378:660–670, 2018.

[9] Martin Trunec and Karel Maca. Chapter 7 - advanced ceramic processes. In James Zhijian Shen and Tomaž Kosmač, editors, *Advanced Ceramics for Dentistry*, pages 123–150. Butterworth-Heinemann, Oxford, 2014.